University of Glasgow

Electropolymerisation of hole transport materials

Pablo Santana Alvaro

September of 2024

School of Chemistry

College of Science and Engineering

University of Glasgow

Table of contents

List of abbreviations

PCE = Power conversion efficiency. It is a measure of how well a device absorbs photons and transforms this energy into electricity

V_{OC} = Open circuit voltage. The voltage difference between the two ends of a device when it is not connected to a circuit. This is one of the variables needed to calculate the PCE

ITO = Indium tin oxide

FTO = Fluorine-doped tin oxide

HTM = Hole transport material

ETM = Electron transport material

HTL = Hole transport layer

ETL = Electron transport layer

PSC = Perovskite solar cell

HOMO = Highest unoccupied molecular orbital

LUMO = Lowest unoccupied molecular orbital

R_{shunt}= Shunt resistance. A measurement of how, due to diverse methods, current leaks from the device, decreasing the PCE

R_{series} = Series resistance. The resistance caused by the thickness of the material, which causes a decrease in PCE

$R_{recombination}$ = Recombination resistance. The resistance encountered by charge carriers when they attempt to recombine with their corresponding pair

CV = Cyclic voltammetry

SAMs = Self – assembled monolayer

PEDOT:PSS = Poly (3,4-ethylenedioxithiophene) polystyrene sulfonate

PTAA = Polytriarylamine

Spiro-OMeTAD =2,2',7,7'-Tetrakis[N, N-di(4-methoxyphenyl)amino]-9,9'-spirobifluorene

TPA = Triphenylamine. This is a common moiety found in a plethora of HTMs

EDOT = 3,4-ethylenedioxythiophene

Fc = Ferrocene. This compound is used in electrochemical analysis as a reference molecule, as its redox reaction to Fc^+ is usually placed at 0.0 V

THF = Tetrahydrofuran

DMF = Dimethylformamide

DMA = Dimethylacetamide

TNT = Trinitrotoluene

DCM = Dichloromethane

TBDSM-Cl = Tert-butyldimethylsilyl chloride

TLC = Thin layer chromatography. This silica plate is used for a quick analysis of a reaction

TGA = Thermal gravitational analysis. A common thermal characterization technique in which the amount of mass is measured against the amount of heat given

DSC = Density scanning calorimetry. A common thermal characterization technique in which heat flow is measured against temperature

FTIR = Fourier transformed infra-red spectroscopy. A common characterization technique used to observe any bond stretching, rotation or vibration that can be found within a compound when infra-red waves are shone upon it

DFT = Density functional theory. A series of calculations that project theoretical energy levels of a compound, amongst other physical characteristics

AFM = Atomic force microscopy. A technique which uses the reflection of a laser to observe the surface of a film or material. Can be used to calculate the thickness of said material

SEM = Scanning electron microscopy. A technique which uses the reflection of a focused electron beam to observe the surface of a film or material.

Declaration of originality

I, Pablo Santana Alvaro, with student ID XXXXXXXX, confirm and sign that this thesis made with the standards for an MSci (Res) in Chemistry, is my own work. I also confirm that I have: read and understood the guidance on plagiarism in the Student Handbook, including the University of Glasgow Statement on Plagiarism; clearly reference in both text and bibliography all sources used in the work; fully referenced (including page numbers) and used inverted commas for all text quoted from books, journals, web etc…; provided the sources for all tables, figures, data etc… that are not my own work; not made use of the work of any other student(s) past or present without acknowledgement, including any of my own work that has been previously, or concurrently, submitted for assessment, either at this or any other educational institution, including school; not sought or used the services of any professional agencies, or any artificial intelligence to produce this work.

Additionally, I understand that any false claim in respect of this work will result in conduct action in accordance with University regulations.

I am aware of and understand the University's policy on plagiarism and I certify that this assignment is my own work, except where indicated by referencing, and that I have followed the good academic practices noted above.

Pablo Santana Alvaro

Abstract:

The perovskite solar cell has been the standard when it comes to organic solar cells, a steadily increasing renewable energy source which is greener than its silicon counterpart. However, even if there have been some advances such as overpassing the PCE threshold of 25% and being close to competing with silicon solar cells (PCE = 26.8% in a silicon heterojunction structure), there are still some issues in operability, more specifically the conductivity and stability, amongst others. One of the main parts of the perovskite solar cell which is proven to be causing some of the problems is the hole transport material. As well as finding new compounds which can act as competitive hole transporters, which have been proven difficult, methods of deposition of said molecules into ITO and/or FTO prior to device creation has been observed to contribute to the increase of these setbacks due to the formation of charge traps, uneven interstitial surface and poor homogeneity, amongst others. Self – assembled monolayers (molecules) (SAMs) used as hole transport materials have overcome some of these obstacles, although alternative deposition methods are still required.

This thesis describes a strategy for deposition of hole transport materials in the form of electropolymerisation. We have investigated the electropolymerisation of some hole-transporting materials and investigated the conductivity of their films.

Acknowledgements

The author of this thesis would like to extend his gratitude to all the members of the Cooke group for their support. I would like to give a special thanks to Prof. Graeme Cooke, for the opportunity to undergo this master's programme, to Dr. Dylan Wilkinson for aid and guidance throughout the project and to Gregor Macleod for facilitating the conductivity and thickness measurements.

1. Introduction[1, 95]

Since the discovery of the photovoltaic effect in 1839 by Edward Becquerel[102], which led to the formation of the traditional silicon solar cell, and the later implementation of a perovskite layer into a photovoltaic system in 2009 by Tsutomu Miyasaka[101], the organic photovoltaic cell (OPV) has been continuously improved with the intention of surpassing the silicon solar cell, as it is, amongst other advantages, cheaper in both synthesis and commercialisation, and easier to fabricate solar cells.

Although there has been a consistent increase in the power conversion efficiency (PCE) (which is a quantitatively calculated percentage that shows how well a solar cell may work) from 3.8% in 2009[101] to over 25% in 2022, there are still some issues related to performance and stability which are crucial to the functioning of devices. However, in order to understand these problems, one must first be familiar with the structure and science behind a solar cell and its layers.

1.1. Perovskite solar cell configuration[100, 103]

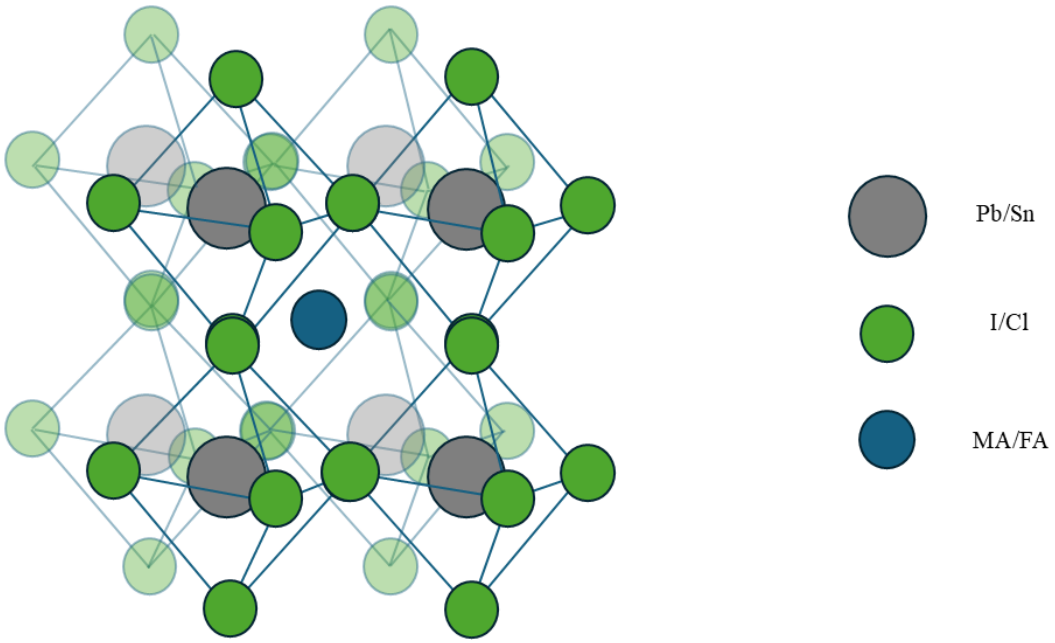

Figure 1: Internal structure of perovskite[100]

The perovskite is the name given to a crystal structure which has lead or tin as the primary cation (although sometimes caesium is also used), and iodine or chlorine ions or a mixture of both forms an octahedral structure surrounding said cation. The columbic interactions between the positive cation and the negative anions hold this structure together. However, in between the spaces between 4 octahedral structures, a smaller organic cation can be found. This is usually either methylammonium (MA, or

$CH_3NH_2^+$) or formamidinium (FA, or $CH(NH_2)^+$), and counteracts the overall negative charge of the anions. In Figure 1, the overall structure is observed in 3D.

In a perovskite solar cell (PSC), the perovskite is the layer in charge of absorbing the photons from light, and it is found in between two electrodes, which are connected to a circuit. Once absorbed, the excitons (electron – hole pair) get excited, which raises the electron (negative charge carrier) from the HOMO to the LUMO of the perovskite, while the hole (positive charge carrier) is left behind. After this separation, the charge carriers will be transported to their respective electrodes (explained later when discussing energy levels).

However, due to the difference in electrostatic charges, electrons and holes tend to recombine back together before any current can be collected, which results in a loss of power generated. In order to decrease the recombination rate, further layers are included to aid the transportation of the charge carriers to their destination, more specifically the hole-transporting layer (HTL), to move holes, and the electron transporting layer (ETL) to transport electrons.

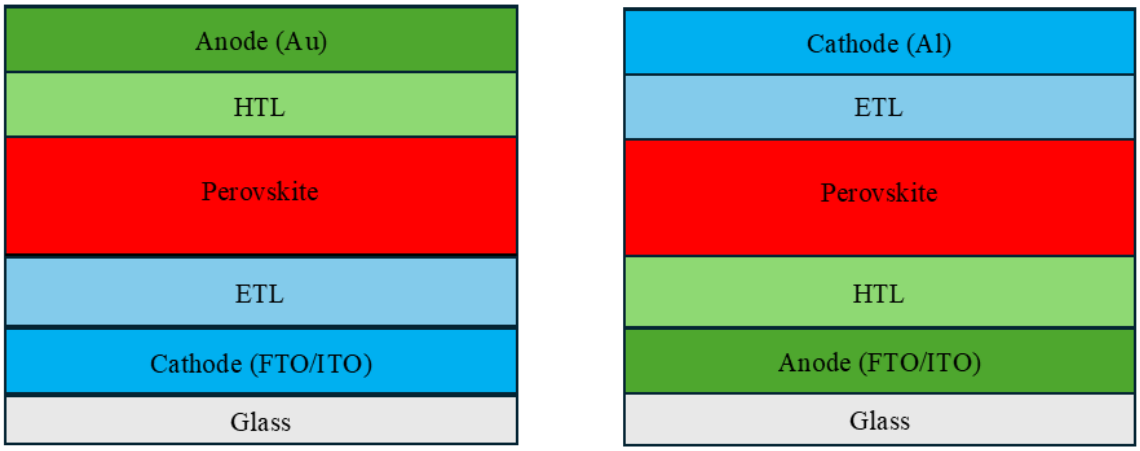

Figure 2: Traditional and inverted structures of a PSC[103]

Figure 2 shows a clearer image of the general set up of a PSC, both traditional (n-i-p structure) and inverted (p-i-n structure). These two structures work essentially in the same manner, however the characteristics of the HTL and the ETL are slightly different in both. For example, the layer closer to the glass must also be as hydrophobic as possible in order to protect the perovskite from moisture.

In both cases, FTO (fluorine doped tin oxide) or ITO (indium tin oxide) is used as cathode or anode in the layer closer to the glass, in order to protect the perovskite from the environment, and the nature of the electrode depends on the metal used for the counterpart electrode.

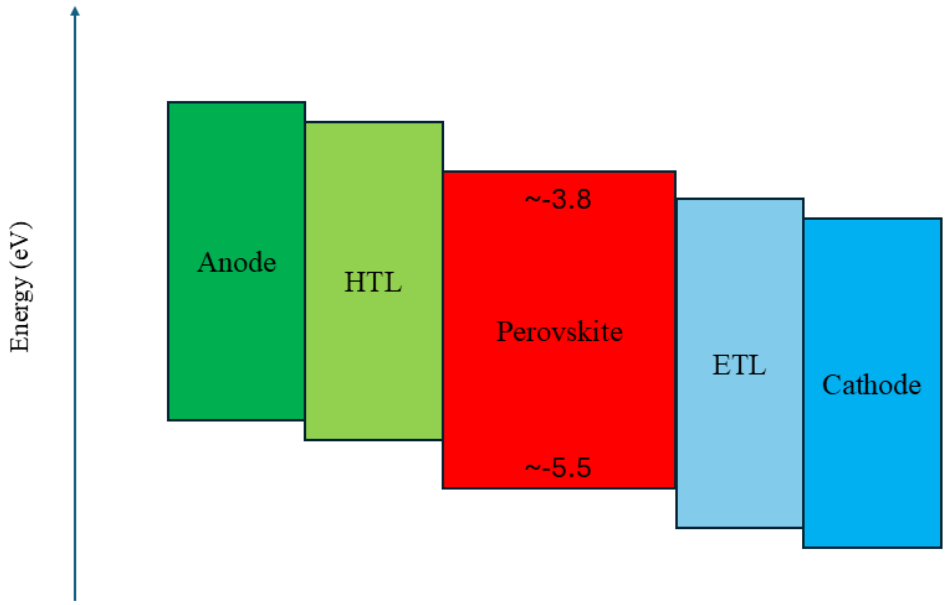

Figure 3. HOMO and LUMO energetic levels of the layers within a perovskite solar cell (simplified)[103]

The reason why the formation mentioned previously worked is due to the energy levels of the HOMO and the LUMO of the components (see Figure 3.). For an ETL to actively transport an electron, the LUMO of the compound must be lower than that of the perovskite (~3.6 eV), thus allowing for relaxation of the electron from LUMO to LUMO until it reaches the cathode. Furthermore, the HOMO of the ETL must be much lower than that of the perovskite (~5.5 eV) in order to stop any holes from moving from the perovskite to the ETL. On the other hand, for an HTL, the HOMO must be higher than that of the perovskite so that the hole can travel to increasingly higher energy levels until it reaches the anode, as well as having a very energetically high LUMO, in order to avoid any electrons passing into the HTL, thus recombining with the hole, producing a loss of current.

Overall, although the configuration of a PSC is simple, there are many details which have to be considered in order to make a device as efficient as possible.

1.2. Problems, and where to improve[104, 105]

Previously, the issue related to moisture in the air was mentioned. If water does make contact with the perovskite, there will be a breakdown of the crystal structure of the perovskite, which would form halogen ions. These halogen ions will then corrode the electrodes, and the overall device irreversibly, rendering it useless.

This example highlights the issue concerning the stability of the compound to the environment, as air, water and acid may cause it to breakdown[105], and considering that the PSC is meant to be placed outdoors, the layers that have the highest exposure to the

environment (in the n-i-p structure the anode and HTL, and in the p-i-n structure the cathode and the ETL) must be engineered so that they are a hydrophobic as possible.

Other considerations that have to be factored in are the overall loss of current caused by traps and pinholes found in the structure. Any heterogeneity found in the interfaces of the perovskite with the charge transporting layers may result in leakage of current, and thus the shunt resistance must be as low as possible (R_{shunt})[105].

The overall resistance that charges may find in their respective transporting layers may also cause a decrease in current obtained, and thus the series resistance (R_{series}) of the layers must also be as low as possible[105].

Recombination[104] is another issue mentioned previously, and thus correct energy levels must be met in order to produce the highest recombination resistance (R_{recomb}), which would allow the device to work more efficiently. This, along with the number of other routes that lead to degradation, have resulted in PSCs that surpasses traditional silicon solar cells very challenging.

However, there are many areas in which further investigation has been made, which has resulted in the significant improvement of device performance. Hole-transporting materials (HTMs) can be chemically tailored into many structural configurations to display a wide array of characteristics and properties. The capacity for tailoring depends on whether the HTM is a small molecule, a polymer, or an inorganic molecule (organic – metallic compound). On top of that, further study into the interface between layers also deepens the general understanding of the interactions between layers, which will aid solving the problems previously identified.

In this dissertation, the focus will be on methods for the deposition of HTMs, and a deeper study into a new type of film forming involving electrochemistry.

1.3. Types of film laying techniques[95]

Throughout the decades, many different techniques have been developed to deposit the layers in a more efficient way, each having their own peculiarities. For all techniques involving solvents, after the process, the layers will have to be annealed in order to evaporate the polar organic solvents used. Not only that, but the perovskite layer has to be annealed *in situ* in order to transform it into its crystalline structure, which is the configuration which absorbs photons and conduct current most effectively.

1.3.1. Solvent engineering[3, 73]

Prior to the film production and deposition processes, most of the layers for a PSC have to be dissolved in organic solvents, as the layers in the form of a solution tend to be easier to manage and control. At first, this was usually performed under one solvent (usually DMF, DMSO, or any other aprotic organic solvent available). However, this method resulted in pinhole and trap formation due to nucleation processes, in which colloids began to form prior within solution. This would inevitably affect the

performance of the device, both in conductivity as well as stability. Not only that, but DMSO and DMF are extremely toxic and harmful to the environment.

To overcome these issues, solvent engineering was carried out to make the process of film solution formation as green and economical as possible. An increase in efficiency has also been a primary target, as the choice of solvent does change the reaction and deposition pathway, as well as the overall morphology of the layers themselves, especially the perovskite layer. Throughout the research, many types of solution formation have been developed, with the anti-solvent system (usually used for the perovskite layer) and the co-solution system been very good examples of solvent engineering.

In the co-solution system, many solvents (two for a binary system or three for a ternary system) are used to dissolve a specific layer of the device. Although this system is quite simple, it has proved to have many advantages compared to the traditional single solvent system, as corroborated by Zhang *et al.* in 2022[92]. One of these advantages is the prevention of the formation of colloid aggregates. This is due to the mixture of solvents, which causes different solvent – solute interactions, which prevents the congregation of macromolecular structures such as colloids. This result in more spread out solutes, which result in a better interaction between the precursors of the layers, and thus a decrease in loss of precursors, making the reactions more efficient. On top of that, due to the multiple different interactions between the solvents and the solutes, difference in solubility could largely decrease, which further helps the reaction to take place more efficiently.

However, even though the overall efficiency is usually greatly increased, many of the solvents typically used tend to be toxic, and thus the increase in amounts of solvent may suggest an increase in overall toxicity, which must be addressed.

In the anti-solvent system, the inorganic salt (for example, PbI_2) and the organic precursors are dissolved in different solvents (the different reactants for the objective molecule would vary depending on whether the electron transfer or the hole transfer layer is been made), with the heavy metal salt being dissolved in DMSO or THF, while the organic precursor is dissolved in another more polar solvent such as alcohols (IPA, for example). When both solutions are combined, the reaction forms the perovskite layer. Upon addition of a strong anti-solvent unto the wet perovskite (or charge carrier) film, such as toluene or chlorobenzene, crystallization is forced due to the low solubility in the anti-solvent used. This system is usually performed just before continuing with one of the techniques that will be described below, as the crystallization process happens quickly.

This method not only uses a lower amount of solvent, but it still controls to a very large degree the morphology of the film produced, avoiding any pinholes or traps and keeping the homogeneity of the film, and thus increasing the performance of the device.

However, even though the number of toxic solvents is reduced compared to the co-solvent system, the solvents used are very toxic and harmful, which must be addressed too. Further research performed by Nadege Ouedraogo *et al.* [51]have found a wide range of less toxic, layer-specific substitutes in order to make the overall process greener, and

although this is a huge step towards commercially available devices, further investigation in solvent engineering has to be performed.

1.3.2. Printing[11, 33, 36, 37, 61]

This technique consists of dissolving the layer in solution (in ink) and, with the use of machinery, place a specific pattern into the surface where the layer needs to be placed (let that be the glass (ITO/FTO), the perovskite, or an overall substrate). There are plenty techniques in this category, but two very important ones are the inkjet printing technique, and the screen-printing technique, and the main difference lies on the pattern used. In inkjet printing, the ink is ejected into a pre-determined pattern made *via* computer. The ejection is made *via* a muzzle, drop by drop. There are two methods in which the droplets can be placed into position: *via* continuous inkjet dripping or *via* drop-on-command inkjet dripping.

Continuous inkjet dripping technique (see Figure 4) consists of a stationary muzzle which infuses a constant stream of ink onto a moving substrate. On the edge of the muzzle, as the ink comes out, droplets form, which are immediately charged due to charged electrodes placed very closely to the edge. Beneath the muzzle, there is a deflector, and beneath the deflector there is the substrate as well as a gutter. The charged ink droplets will then fall through the deflector, which will then steer the droplet either into the gutter (and thus, discarded) or into the substrate. The deflector is controlled *via* a specific amount of voltage being applied (which causes the steering), and thus a specific pattern is produced onto the substrate. Although this technique is effective, it does waste a lot of resources, which can be costly, and thus the drop-on-command technique is usually used.

On drop-on-command (see Figure 4), the ink is also placed in a muzzle, but this muzzle is then connected to a voltage supply. The ink flows dropwise into the substrate under the influence of the voltage, and as the muzzle moves, the ink is being ejected, allowing a very accurate pattern to be produced. The method in which the ink is forced out of the muzzle can be either by a piezoelectric process, in which pressure generates electricity, and thus voltage (which is usually preferred, as it does accommodate most solvents); or by a thermal bubble, in which the ink is heated up to form a vapour bubble, which forces the ink out (this technique is still very popular, as water can be used as part of the solution).

Either way, these two methods are the preferred way to place layers onto rough or sensitive substrates, as it does not require direct contact from any machinery onto the surface, which could result in the substrate being damaged.

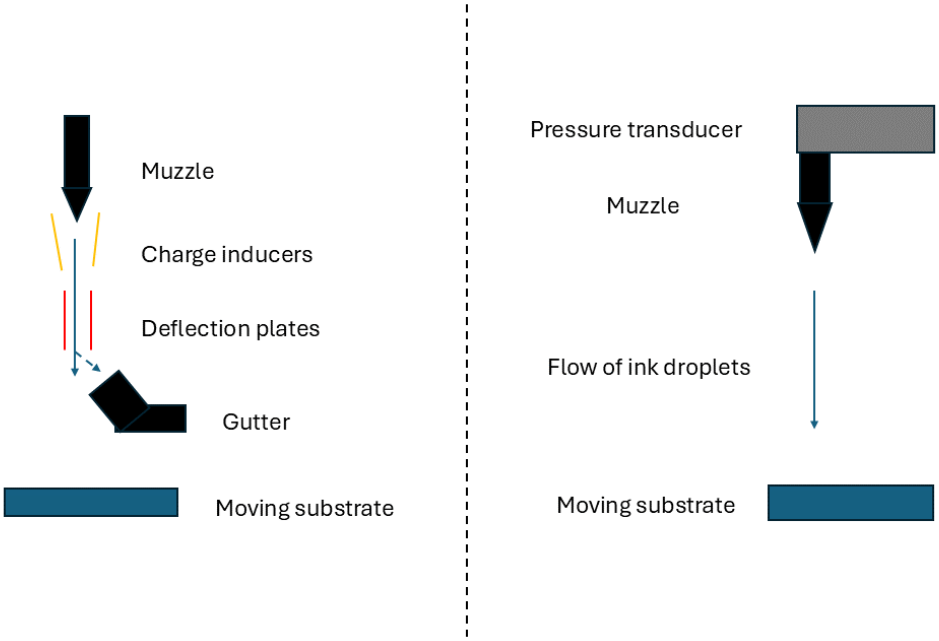

Figure 4: Diagrams showing continuous technique (left) and drop-on-command technique (right) set ups

On the other hand, screen printing technique (see Figure 5) works *via* a mesh that has a very specific design. This mesh is then placed on top of the substrate, and these two are then placed below a squeegee (with the mesh facing it). As ink is placed on top of the mesh, the squeegee forces the ink to go through the holes in the mesh, applying ink. As soon as the ink is placed on the substrate, the mesh is lifted, leaving behind the substrate with the predesign pattern on top. As this procedure can be made several times, the thickness of the layer is highly controlled, which could help optimising the R_{series} caused by the thickness of the layer and the potential traps that could be caused by the thinness of it. Although it is a technique used to place any sort of layer, and it does have very large scalability and pattern flexibility, it is a particularly slow technique, which could hinder the commercialization of PSCs made under this approach.

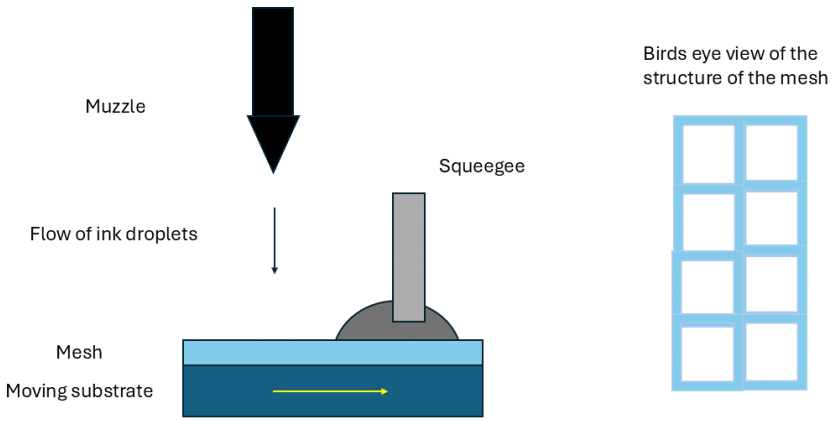

Figure 5: Diagram showing screen printing, with bird's eye view on the right

1.3.3. Depositions[9, 13, 24, 56, 69, 80]

The main difference between deposition techniques and the rest of film laying processes revolves around the non-usage of a solution, as the layer deposited is placed particle by particle into the substrate. This leads to an increase in stability caused by the lack of potential decomposition caused by solvents, but it does require a lot of machinery, which would be expensive. Within this category, there are three main categories: atomic layer deposition, (chemical) vapour deposition and vacuum deposition (sometimes included in the vapour deposition, but it is physical).

In atomic layer deposition, the layers that are usually used are inorganic, both for ETM (such as TiO_x, ZnO, or SnO_x) and for HTM (such as NiO_x, VO_x or MoO_x). Throughout the process, the substrate is placed on a sealed environment. Here, the metal precursor will be injected and adsorbed chemically into the substrate, atom by atom, and with the help of oxidising compounds (such as O_3 or H_2O), the metal complexes will react with each other to form a monoatomic layer. Afterwards, the extra ligands which have been detached from the metal will be purged outside the container using an inert gas such as N_2 or Ar. Although this method has seen some success, such as Jeong *et al.*in 2019 (which showed a $[Mo(CO)_6]$ complex HTM which produced a PCE of 21.06%), there are still mayor setbacks in the technique, such as the need for low temperatures when laying on top of a perovskite layer, as perovskites do oxidise quite fast, and the low amount of growth that the process allows requires many rounds, increasing time and cost.

In vacuum deposition, the process is somewhat similar to atom layer deposition, but no other compound is needed apart from the layer precursors. The compound is vapourised within a vacuum, and then evaporated onto the substrate, covering any area exposed to the compound, including gaps and spaces caused by potential grains in the substrate. This technique is very effective in forming controlled, high quality polycrystalline layers with little to no traps, as shown recently by Hui Wang *et al.*, with their device reaching a staggering 21.32%. However, even though there is potential, and it does allow for films covering over a large area (which is an issue solvent-required techniques tend to have), it is a recent process in the field of photoelectronics, and thus not a lot of research has been done. Furthermore, it does require for the compound to be in the gas phase under vacuum at temperatures of approximately 60˚C.

Although vapor deposition is sometimes divided into two (vacuum deposition, as it does rely on the vapor to be formed, and chemical), here it will refer to the chemical variant. The process is very similar to that of the vacuum deposition, but instead of the final compound being deposited, the precursors of the layer are the ones being vaporized, and then evaporated onto the substrate, adhering to the surface, and once there the precursors react or decompose to form the desired layer. It does allow for a wider range of possibilities and options for the precursors compared to the vacuum deposition method, which leads to higher tunability, and devices made have shown promising results, such as the ones made by Andrea Capasso *et al.*, which in 2016 they made a PSC with graphene-based derivatives with ethanol as precursors for HTMs, which resulted in a PCE of 5%, comparable to a state-of-the-art PEDOT:PSS device, performing at around the same PCE. However, very high temperatures are usually

required, and the reaction pathways cannot be controlled *in situ* in case any unwanted side reaction does form, which would lead to a different compound.

1.3.4. Coatings[4, 6, 15, 17, 52, 59, 67, 76]

Similarly to printing, the coating processes rely on a solution of the target layer being placed directly onto the substrate. However, instead of drops of the ink dripping into the substrate into a predetermined pattern, the solution will be placed throughout all the surface of the substrate.

There are many types of coating techniques, and four of the most popular ones are knife coating, slot-die coating, spin coating (which is the most popular), and spray coating.

Knife coating (see Figure 6) consists of a blade placed very near to the substrate, at a known and fixed distance. A constant source of solution (or ink) is added into the substrate, and the substrate is moving below the knife. This makes the knife stop any extra solution passing through, creating a film with a fixed and controlled thickness. This method is arguably the simplest of film laying technique, but its control over thickness and the small amount of machinery needed makes this a very cost efficient and effective technique. However, the main disadvantage is the amount of solution used, as it must be in excess, and thus depending on the solvent it can increase significantly the price. Not only that, but the film has to be quite thick in order for the process to work, which would increase the R_{series}, as well as the possibility of streaking caused by a damaged or blunt knife, which would be detrimental to the homogeneity of the thickness, leading to different R_{series} and thus a decrease in reproducibility.

Furthermore, the environment in which the coating is dried is crucial for this technique, although it is also applicable to the other coating processes, and to a smaller degree printing processes (as these have more controlled parameters by default). This is proven by the experiment made by K. Peters *et al.* in 2009. During drying, many factors, such as phase separations and polymer gelation (which happens when the polymer has the ability to cross link and forms a large 2D or 3D structure which increases the viscosity of the layer). These two factors influence how the thickness of the layer can shrink during the annealing process, and results (according to the paper, although further research is required) in higher temperatures leading to an increase in grain size and other topographic figures, which in return creates a deviation of conductivities between samples placed under different environmental conditions.

In slot-die coating (see Figure 6), the setup is very similar to that of the knife-coating procedure, but instead of a knife there is a muzzle. This muzzle is attached to an ink dispenser, which allows it to expel ink into the substrate, while the substrate moves just below it. The thickness of the film is controlled by the distance between the muzzle's mouthpiece and the substrate. This set up has similar advantages to the knife coating, but the amount of ink ejected is much more controlled, which can result in less solution needed, and thus more economical as well as green. However, there are operational limits, such as the theoretical low amount limit of solvent used (as it may cause a larger meniscus, which could lead to an heterogeneous layer), air entrapment into the solution which leads to bubbles formed and thus heterogeneity in the film, and flooding or

dripping caused by too much or too little ink being dispensed at once, which may cause issues with the heterogeneity of the layer, too. All these factors are easy to consider when performing the technique, but there are still limitations which could affect severely the creation of the device, and does not have a lot of versatility.

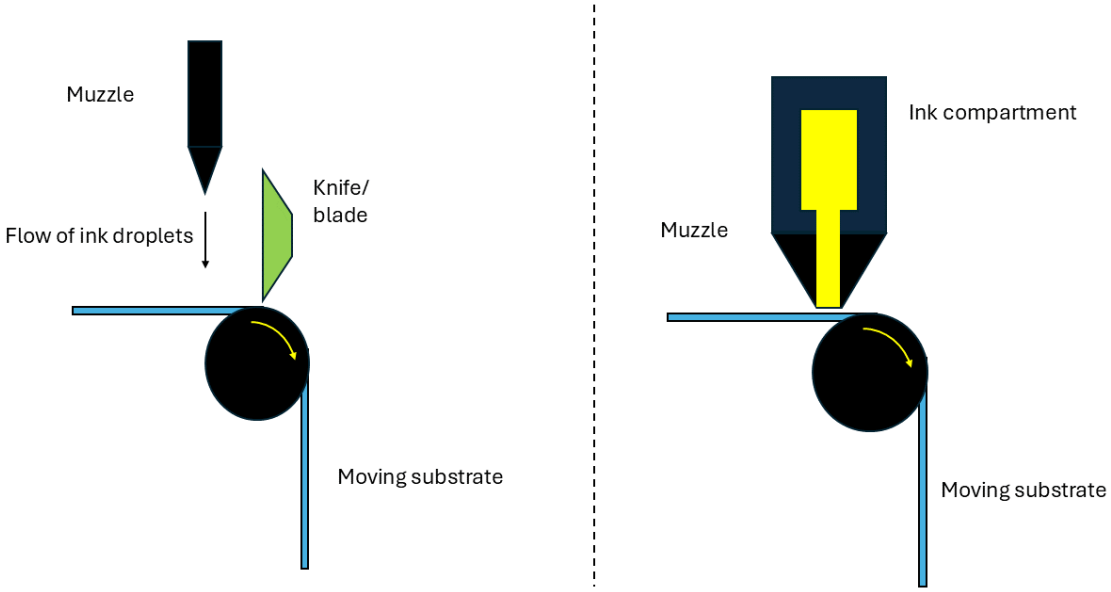

Figure 6: Diagrams of knife – coating (left) and slot-die coating (right)

Spin coating (see Figure 7) is by far the most popular method in which to place a layer into a substrate, as it is the most cost effective, and leads to the most homogeneous layer with controlled thickness and low amount of solution/ink require, making it a particularly economic and green technique. The technique consists of placing solvent onto the substrate. The substrate will then start spinning, which due to centrifugal force spreads out throughout the substrate in a homogeneous manner. While the substrate is spinning, an airflow is blown directly into the substrate, which helps with the evaporation of a significant amount of the solvent (although this depends on the viscosity of the solution).

The sample may be applied to the substrate using two methods: using a stationary disc (called static dispense) or a moving disc (called dynamic dispense). Usually, if the material has poor wettability, a dynamic dispense is required as it forces the compound throughout the surface as soon as it reaches the substrate, which helps forming a better interaction between the substrate and the layer. The substrate then accelerates uniformly, until it reaches an arbitrary maximum speed. In this process, some ripples do occur, but as the solution spreads throughout the substrate, and evaporation of the solvent occurs, the layer becomes thinner and thinner, until the ripples are either negligeable or not present anymore. This is caused by the drag between the substrate and the solution, as within the layer the part of the solution near the substrate rotates with the substrate while the part of the solution on top stays behind.

After the evaporation of the solvent, the film left behind is similar to that of a gel, or a highly viscous material, and thus it still requires annealing afterwards.

Although this technique has very defining advantages, reaching an impressive 26.07 % PCE in a device made by Wenlin Jiang *et al.*[91] in July this year, the procedure still has disadvantages which must be addressed, such as scalability, and the increased difficulty of achieving and replicating a specific pattern, which would increase the conductivity of the layers.

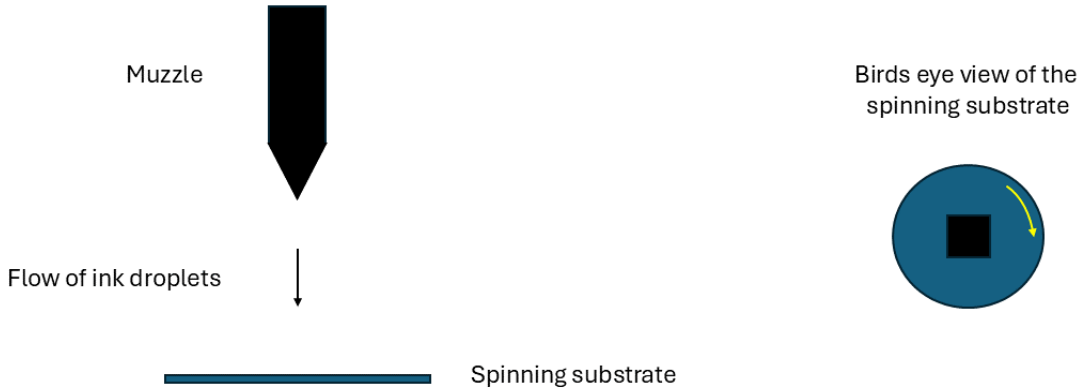

Figure 7: Diagram showing the set-up of the spin coating technique

Finally, in spray coating (sometimes called pneumatic spray coating) (see Figure 8) the ink is placed on a nozzle, and once there the ink will be sprayed onto the substrate as an aerosol. The nozzle is connected to an air compressor, which is what allows the spraying. This technique has some important benefits, such as simplicity in operation, very easy to up-scale, and relatively cheap in terms of machinery. However, there are some important drawbacks, one of them being increasing the size of the perovskite substrate over 10 cm^2 will cause a decrease in PCE, so even if the technique can increase in size, the results made will have a size limit. Not only that, but part of the solution will go to waste, as in order to make sure the substrate is fully covered, the area in which the aerosol will be sprayed will have to be slightly larger. A third drawback is that devices made using this process, although efficient (with perovskite spray coated into devices reaching a PCE of 16% in 2022[88]) they tend to have stability issues, which must be addressed.

Within simple spray coating, there are many other techniques which strive to overcome some of these problems. One of them is electrospray coating, where the droplets are charged with static electricity. This causes an even finer mist, as each droplet will be electrostatically repulsed from one another, which results in a more homogeneous layer being deposited. Furthermore, the size, the charge and the flow rate can all be tuned. Finally, as the nozzle can have an area of spraying programmed into it, making the spraying more efficient, which would cause a decrease in waste. Thus, also simple spray coating may have some issues, this technique has shown increasing development throughout the years, and thus it can be considered a promising process for the future commercialization of PSCs.

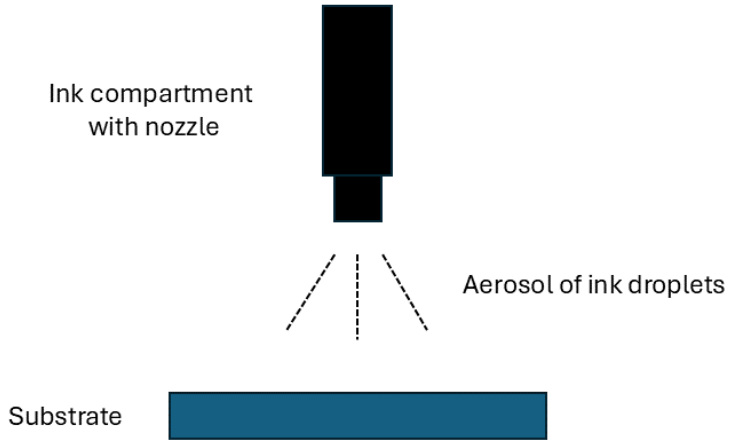

Figure 8: Diagram showing spray coating

1.3.5. Chemical bath[22, 42]

Chemical baths are mainly used to form film layers of charge carrier materials which have an inorganic/metallic part (usually oxides), such as NiO_x or SnO_2, and it conforms of two parts: the treatment of the substrate, and the film deposition.

In the treatment of the substrate (see Figure 9), the substrate itself will have to be chemically and physically cleaned in order to achieve an uneven surface. This is crucial, as any deformity within the surface of the substrate will be used as a nucleation site for the main reaction in the film deposition later. To achieve this, the surface will be scrubbed by an anti-greasing agent (such as detergent), as well as ultrasonic treatment (with water and acetone) multiple times, each time being followed by rinsing the surface with deionised water. Once the surface is completely de-greased, it will be scrubbed a few more times with different common organic solvents, such as acetone, organic alcohols, trichloromethane etc… to achieve a chemically clean surface. Finally, after this the substrate will be dried in an oven or heated for a small amount of time (approximately 10 minutes), which concludes the substrate treatment.

Once cleaned, the substrate will then be dipped in a premade solution containing the precursors of the inorganic layer for a prolonged amount of time, in order to allow for the films to be produced. There are three precursors: the salt of the metallic part of the film (which gives the metal), a complexing agent (which will aid in the formation and transportation of the complex into the substrate), and a chalcogenide (which upon its hydrolysis allows for the formation of the oxide of the metal. This could be Se^{-2}, S^{-2}or O^{-2} (usually found in water itself as ^{-}OH)). These precursors must have a higher solubility than the film itself, as this method relies on the formation of complexes between the metallic centre and the other precursors, which forms an insoluble species. This species then precipitates upon the substrate, more specifically in the nucleation sites forcing the nucleation step to begin, in which the insoluble ionic complexes start forming in the film, which grows exponentially as the surface of the film increases.

Due to the nature of the formation of complexes, the pH and the temperature must be held under very strict parameters in order to avoid any side reactions happening, as well as guaranteeing a certain control in the formation of the films caused by a controlled precipitation of the insoluble “monomers” of the film.

Chemical baths have been a successful procedure for layer deposition throughout time. In 2023, Sibo Li *et al.* produced with this technique NiO_x films to be used as hole-transporting layers using $Ni(NO_3)_2$, amino-alcohol ligands and water. After annealing, the solar cell reached a PCE of 22.03% with the aid of SAMs.

Chemical baths overall have a very wide range of advantages which has made this technique very popular, such as their ability to be scaled up easily (as it is readily available for large substrate surface areas), their easy setup and cheap processing. These factors make this process be commercially friendly. This technique is also very tuneable, as the ligands within the complexes can be changed, which allows for a wide variety of rates of reaction, which in this deposition method directly influences the morphology of the film itself. However, this process does have major drawbacks, as it does require a high level of precision when dealing with parameters, as a small deviation on concentration, or more importantly pH or temperature may lead to side reactions which could be detrimental to the overall process. Not only that, but this technique, although very tuneable, it is limited to inorganic compounds, with which it has a lot of potential for growth.

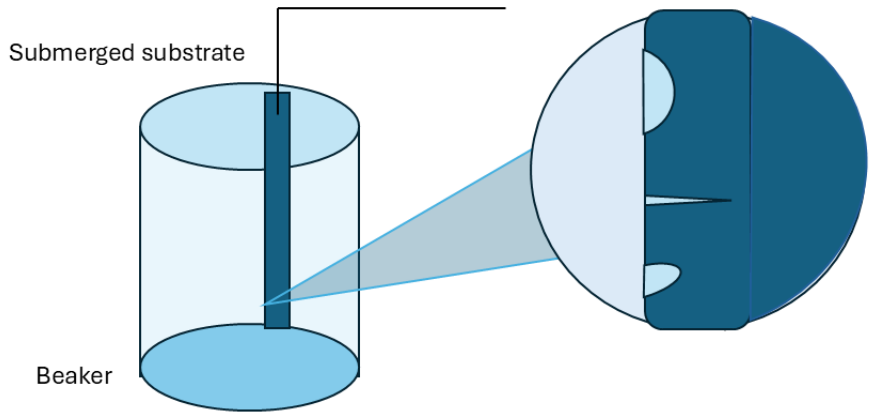

Figure 9: Diagram showing the set-up of the chemical bath technique, showcasing the traps and nucleation sites in the perovskite

1.4. Self-assembled monolayer (molecules) (SAM)[84, 96, 97, 98]

In the previous segments it was discussed how new layers can be deposited on top of the substrate. Overall, all these processes have advantages and disadvantages, and are still under investigation in order to improve their efficiency and thus forming better layers.

However, recently, there has been a new type of materials which can form a molecule thick layer by reacting with the surface of the substrate. These molecules are called self-assembled monolayer (or molecules) (SAMs) and have attained an increased interest within the scientific community due to their key advantages against other typical HTMs and layer deposition techniques.

SAM molecules have three parts: the anchoring group, the 'body' or spacer and the 'head' or functional group. All these parts have intrinsic properties which allow the SAM molecules to perform how they should. The anchor part of the SAMs (see Figure 10) is in charge of connecting the molecule to the substrate, which typically have hydroxyl groups attached to its surface. The usual moieties are carboxylic acids (or esters) and phosphoric acid derivatives, but silanes are also used. These groups are oxygen rich, which is crucial for the connection into the substrate, done in two steps. The first step is the hydrolysis, in which the moiety chosen is hydrolysed from ether groups (-OR) into hydroxyl groups (-OH) (for example, from esters into carboxylic acids, or phosphate esters into phosphoric acids). Once the hydroxyl form of the compound is made, a condensation reaction occur between the hydroxyl group of the SAMs and the hydroxyl group of the substrate, releasing water in the process, and forming a monodentate ligand between the silane, carbonyl or phosphate moiety and the surface. Usually, the water produced in this condensation reaction or in the following assembling reaction is later removed *via* annealing or heating.

During the assembling process, some parts of the SAMs can react further in order to form the conducting layer. Any hydroxy group can sometimes condense further with surrounding hydroxyl groups, such as with silanes or with phosphonic acids, forming the network of the SAMs. Furthermore, the oxo groups can sometimes datively or directly bond with the substrate layer, forming bidentate or tridentate ligands. During this process, hydrogen atoms are displaced from the anchoring group into the hydroxyl groups in the substrate, which could result in water formation, and the formation of oxygen vacancies. These vacancies can then be filled *via* the oxo groups of the moieties, in case any bidentate ligand can further turn into a tridentate ligand. The type of ligand as well as moiety is crucial to the performance of the PSC, as it affects the structure and order of the layer, as well as the strength (and thus length) of the bond between the SAM and the substrate, both of which interfere with the conductivity of the layer. Anchoring groups can also bond to perovskites.

The body or spacer of the SAMs (see Figure 10) connects the anchoring group and the functional group of the molecule. This moiety is usually an alkyl chain, and its job is to hold the 3D structure of the compound together *via* Van der Waal forces between non-polar molecules. These forces then allow for an orderly configuration, and thus structure, which raises the conductivity of the layer, as the film quality increases. In case that the alkyl chain is straight, the longer the chain implies stronger Van der Waal

forces, and thus a greater cohesion and order within the layer. However, if the alkyl chain is branched, an increase in length implies a decrease in cohesion due to the steric hinderance between the main chains of the alkyl moieties, and thus a shorter chain length is preferred.

Finally, the head or functional group of the SAMs (see Figure 10) is the most electroactive part of the molecule, and thus the one that gives the energy levels for the molecule. As this implies, this part has to be selected carefully in order for the molecule to align correctly with the perovskite or substrate and the surface itself, as physical connection is not enough for a good electronical connection. Sometimes, the energy levels of SAMs are such that this interface layer can function as an HTL itself, as conductivity mainly relies on them.

Not only that, but surface energy is also determined by the functional group of the SAMs. When the anchoring groups form monodentate, bidentate or tridentate ligands with the substrate or perovskite, it changes the electronics of the anchoring surface in comparison with the rest of the substrate or perovskite. This excess of energy in the surface is the surface energy. Ideally, if there is a very strong interaction (and thus a very high surface energy) between the SAMs and the substrate, a 2D structure may form, molecular layer by molecular layer. On the other hand, if the interaction between SAMs and surface is not as high as it should, and thus the surface energy is not high enough, the intermolecular forces (Van der Waals, for example) become very strong, and thus a 3D structure is formed. This difference in configuration is crucial, especially for p-i-n structures where the perovskite may be laid upon the SAMs (in case the SAMs acted like an HTL), as the 2D structure favours an appropriate crystallisation of the perovskite, and thus an improved charge transportation, resulting in better PCE. Overall, 2D structures are the ones sought after.

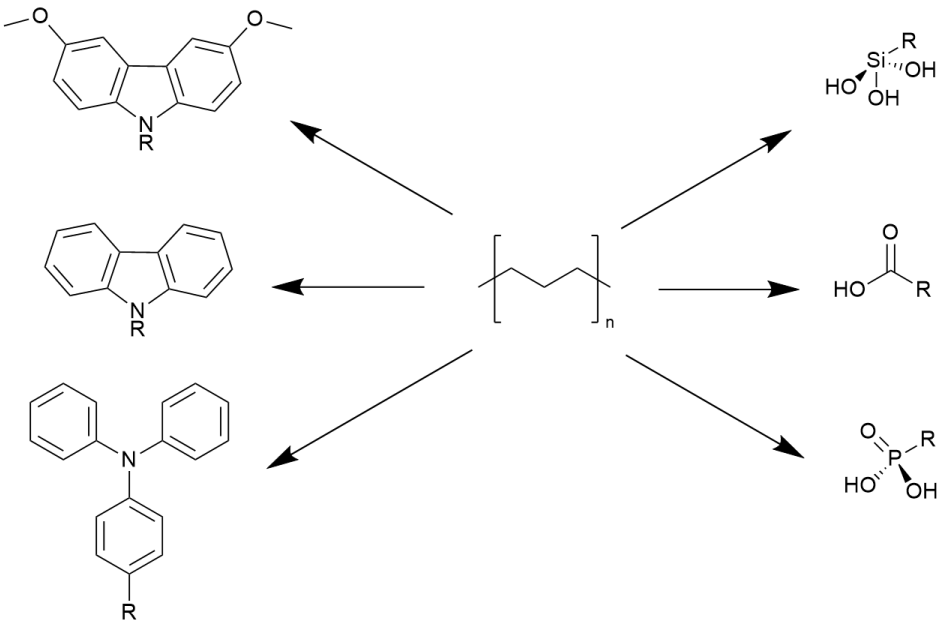

Figure 10: Possible headers (left), spacer (centre) and anchoring groups (right) for a SAMs

Furthermore, the technique used to place this molecule is also crucial, and either vapour deposition or cyclic voltammetry is preferred, sometimes chemical bath. Overall,

thermal annealing has an enhanced importance (especially with cyclic voltammetry and chemical bath), as high temperatures tend to make the SAMs form stronger and better bonds with the substrate, which results in better devices, making temperature control critical during the final steps of the layer formation.

When these three components are correctly chosen, it can result in very high PCEs in not only in single PSCs, but also in tandem PSCs. An example of this is in 2021, when Aktas *et al.* produced two SAMs, EADR03 and EADR04, with carboxylic ends (see Figure 11). These were used as HTLs with an ITO substrate, and placed under immersion, and reached a PCE of 21.2% and 20.6% respectively, although solubility issues were encountered.

Another example was the one produced by Casella *et al.*, which formed a phosphorous acid-based molecule, MeO-2PACz (see Figure 11), which connected to the perovskite $MAPbI_3$ *via* a combination of spray and spin coating, which performed well at a PCE over 20%. This PCE was later increased further to a 20.8% by using gas-assisted spray coating, which although not comparable to commercially available PSCs with PTAA or Spiro-OMeTAD (later explained), it did produce the highest PCE to date in devices made *via* spray coating.

Finally, in 2023 Guo *et al.* produced a phosphonic acid-based molecule (see Figure 11), which works *via* a donor – acceptor system, and was placed in a p-i-n device with ITO and silver electrodes. This device, under careful investigation, managed to reach a PCE of 23.24% and demonstrated very good stability, demonstrating that these types of molecules have the potential to be commercially viable.

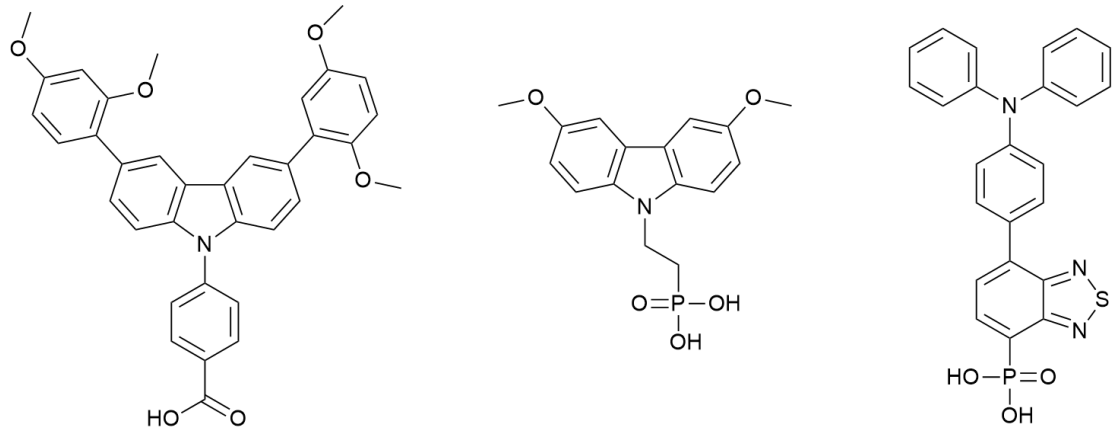

Figure 11: Example molecules made by Aktas (left), Casella (middle) and Guo *et al.* (right)

The main advantage of SAMs is that they overcome the issues corresponding to the interface between the substrate and the perovskite by forming a chemical bridge between them, which allows good conductivity and thus good performance even in rough surfaces. Not only that, but usually SAMs are used in very thin layers, which results in a reduction of materials used per device, and thus lower costs, as well as a decrease in the amount of solvent used to make said layers in the substrate, which results in greener processes and cells. The low thickness of the layers also minimises the resistivity caused by the thickness of layers (R_{series}), which results in an increase in PCE. Finally, the molecule does have a lot of tuneability, and thus a significant prospect

towards future improvements as well as potential configurations. Overall, these molecules offer higher conductivity at a much lower costs, making devices using these materials very competitive against traditional silicon solar cells.

However, even if this process has many attractive benefits, it still has some shortcomings which have to be addressed. The main issue concerning SAMs is their lack of wettability, which is caused by the low attraction between the metallic oxide surface of the substrates and the organic molecules which form the SAMs. This lack of wettability, as well as limited solubility, causes the SAMs to display low reproducibility between different batches, which causes difficulty in the attempts of improvement. Not only that, but the lack of wettability causes the layers to have a low density. Higher density is usually preferred, as it improves the conductivity of the layer, and thus even though the layers are good conductors, they do not operate to their full potential yet. A lot of effort is being placed into investigating different approaches to overcome said setbacks, one being the engineering and creation of a molecule which has a hydrophobic and a hydrophilic part (an amphiphilic molecule), which could improve the wettability of the SAMs and thus have higher density, as well as improved reproducibility, but this is still a work in progress.

1.5. Electropolymerisation of porous materials[93, 106-111]

SAMs are not the only type of molecules which have piqued the interest of scientists. CMPs (conjugated microporous polymers) are a type of molecule which, like SAMs, can electropolymerize to form HTLs. However, unlike SAMs, CMPs use their π backbone in order to transport charge carriers, and thus usually form more planar structures. CMPs were first discovered by Cooper *et al.* in 2007[111] when studying potential molecules for gas storage and catalysis, but it was later discovered that these molecules where also useful in an optoelectronic setting.

The conductivity of CMPs arise from the slightly different monomeric moieties energy levels within the polymer, which forms an energy band akin to those found in semiconductors such as silicon in traditional organic cells[110]. Due to this, the π backbone becomes an easy intramolecular pathway to transport the charge carriers from the active layer of the OPV to the electrodes. Furthermore, due to the high amount of double bonds throughout the structure, CMPs tend to show high chemical and thermal stability, as well as hydrophobicity, which are all key properties for designing HTMs.

By electrochemically placing CMPs into ITO/FTO, many of the defects found within the surface can be eliminated or mitigated *via* control of the thickness of the layer[109], which alongside the inherent porosity of the material, increases the R_{recomb} of the electropolymerized layer, and thus increases the efficiency of the OSC.

In 2017, Liu *et al*. made a CMP using carbazolyl triphenylethylene as a monomer and used in combination with PEDOT: PSS as the HTLs in a solar cell[106]. This CMP was difficult to dissolve in common solvents, demonstrating its chemical stability, and was attributed to the cross-link system of the polymer. After characterization, two samples were made, one with PEDOT: PSS alone and another with the combination previously

mentioned, and results concluded that the sample with the CMP had 0.94% more PCE than the one only showing PEDOT: PSS (8.32%, compared to 7.38%)

Another example could be the CMP made in 2020 by Supreetha *et al.* using 1,3,5-tri(furan-2-yl)benzene as a monomer, but was used to detect ovarian cancer cells miRNA[107]. This CMP was coated into flexible ITO and used with known, relevant concentrations of an ovarian cancer cell biomarker, and showed high genosensitivity towards the miRNA biomarker under the conditions mentioned in the study.

An example which highlights CMPs ability for gas storage can be noted with the CMP made by Zongyao *et al.* in 2020, which electropolymerized 2,2',7,7'-tetra(carbazol-9-yl)-9,9'-spirobifluorene to form a molecular sieve with high surface area and strength for high pressure systems with the aid of carbon nanotubules[108].

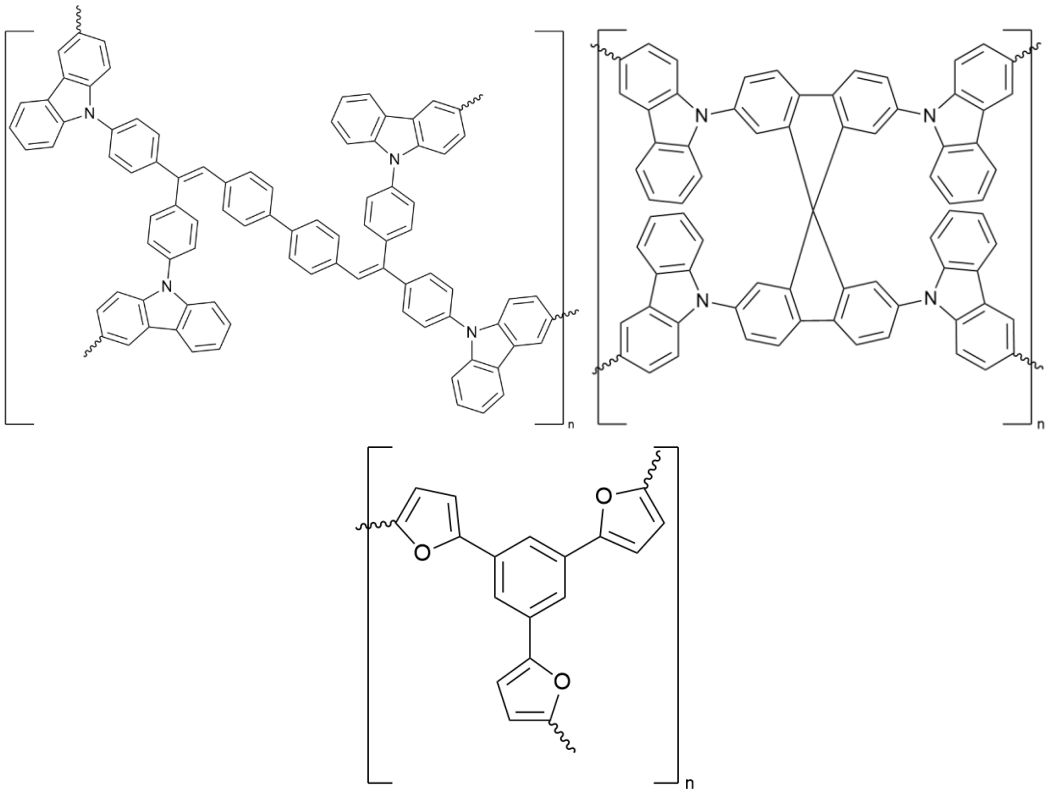

Figure 12: Liu *et al.*'s molecule (top left), Supreetha *et al.*'s molecule (bottom) and Zongyao *et al.*'s molecule (top right)

1.6. Electrochemistry[2, 20, 21, 32, 41, 68, 70, 71, 72, 89]

Although SAMs seems to be the future of PSCs, new techniques have to be investigated and developed which have proven to be promising, and one of them is *via* the use of electrochemistry to form polymers. This thesis will describe efforts to use electropolymerisation of appropriately functionalised monomers to furnish hole-transporting layers. However, before commenting on electropolymerisation, an understanding of the set up and the overall processes involved are crucial for the comprehension of the technique. In this project, CV (cyclic voltammetry) is used, but this technique has been made with other analytical electrochemical programs.

1.6.1. Electrochemical cells

In electrochemistry, electrochemical cells are the space in which non-spontaneous reactions happen thanks to electricity (electrolytic cells). For an electrolytic cell to work, an electrode must be placed within a solution (electrolyte), and a voltage must be applied. This voltage will then oxidise or reduce the contents within the electrochemical cell, forming an oxidised or reduced species, in exchange for the electrode being reduced or oxidised (respectively). A classic example would be the copper electrode being placed within a solution of zinc sulphate, and *via* an applied current, zinc solid will form (zinc gets reduced), while the surface copper atoms will dissolve forming copper sulphate (copper gets oxidised), liberating electrons in the form of current in stoichiometric amounts to the limiting reagent between zinc and copper.

In an analytical electrochemical setting (see Figure 13), the electrode in which the voltage would be applied would be the working electrode, and it is chemically inert in order to avoid any reactions that could occur within solution. This electrode is usually made of glassy carbon or platinum. A thinner reference electrode is usually necessary, as any potentiostat used to control the potential applied would have to be calibrated. This reference electrode must have a well-defined equilibrium potential, and this is typically created by having this electrode in an enclosed system within the electrolyte with a mesh in which only electrons can pass through. This is the case for the saturated calomel electrode (SCE), in which mercury, a salt of mercury (typically mercury (I) chloride), a platinum electrode and a solution of a chlorine salt (typically potassium chloride) forms a standardised cell. The mercury becomes reduced, forming solid mercury and the chloride anion dissolves in the solution. The standard hydrogen electrode (SHE) works in a similar fashion, with a platinum electrode being in contact with an acidic solution, and in the presence of hydrogen gas, as well as the Ag/AgCl electrode, in which a silver electrode is surrounded by silver (I) chloride salt and placed in a solution containing chloride anions (such as potassium chloride). Another form of reference electrode would be the much simpler Ag/Ag_2O, in which the silver wire has naturally occurring silver oxide on the surface, which protects the surface from chemical corrosion.

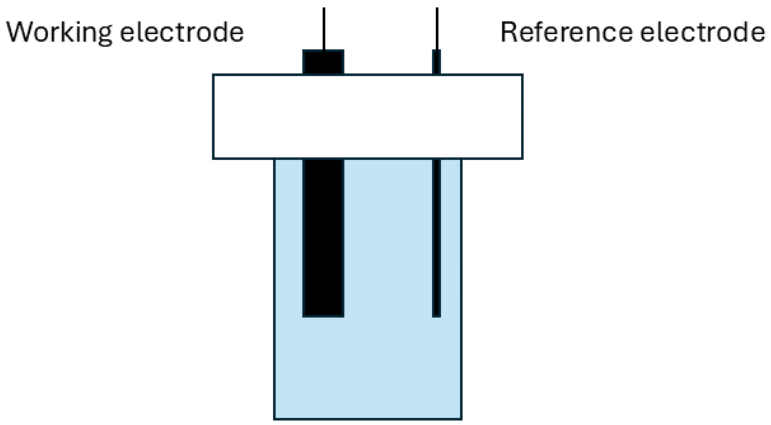

Figure 13: Set up of the two-electrode system in an electrochemical cell

This system has the disadvantage of forcing the reference electrode to become the opposite of the working electrode (if the working electrode is the cathode, the reference electrode would become the anode as the molecules within the system become reduced, and *vice versa* when the molecules become oxidised). In order to avoid that, a third electrode is usually placed, called the counter electrode, and its function is to provide electrons when an oxidation occurs in the working electrode, and gain electrons when a reduction happens, thus completing the circuit. This electrode is also made from a chemically inert material, such as platinum. An electrochemical cell with a working electrode, a reference electrode and a counter electrode is sometimes referred to as the three-electrode system (see Figure 13), and it is the preferred system in which to measure the potential of any electroactive organic system.

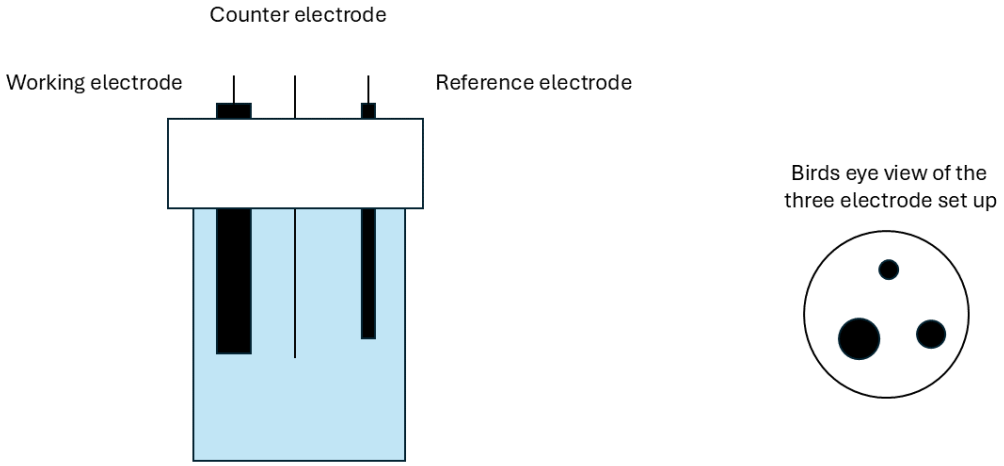

Figure 14: Set up of the three-electrode system

1.6.2. Cyclic voltammetry (CV) [16, 26, 40, 50, 63]

With this set up (see Figure 15) there are many techniques which are used to analyse the electrochemical capability of an organic molecule, such as linear sweep voltammetry, bulk electrolysis and cyclic voltammetry.

The main difference between these techniques is the application of potential. In bulk electrolysis, a specific voltage is applied for a controlled amount of time to ensure the complete or partial oxidation or reduction. In linear sweep voltammetry, the potential goes from one voltage to another, and the results are recorded from any oxidation or reduction that could happen within that potential window. In cyclic voltammetry, similarly to the linear sweep voltammetry, the potential goes from one voltage to another throughout a specific potential window, but it continues back to the original voltage to record any reversible or irreversible reaction which could happen within that potential frame. Because of this, CV is usually the preferred technique for an electrochemical analysis of a new compound, although it is more time consuming.

For a CV set up (although it also applies to the other techniques), the compound will be dissolved on a selected organic liquid which is not suspected to be oxidised or reduced

within the potential window in which the compound will be studied, such as THF, DCM, acetonitrile etc… The organic solution must also be as dry as possible, as well as under nitrogen bubbling, as the hydrolysis of water (or the reduction of oxygen) happens close to 0 volts.

Furthermore, the solution itself will have a specific resistance. Because of this, a supporting salt is added in order to increase the conductivity of the solution. This salt, usually called supporting electrolyte, must dissolve readily into the solvent used, as well as being chemically and electrochemically inert. This will make any current generated by any redox reaction occurring within the solution detectable without a major interference with any current caused by the movement of ions in solution.

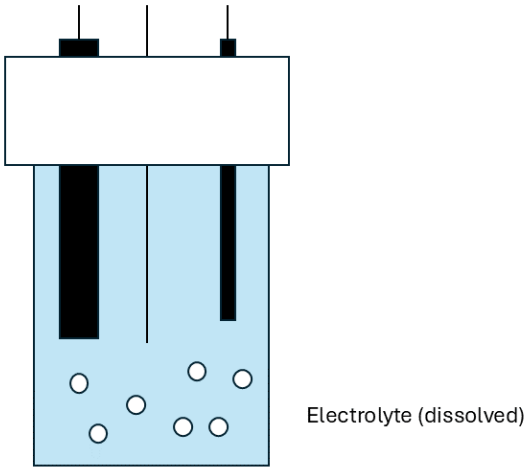

Figure 15: Set up of a CV

Upon starting the CV, the electrolyte cation and anion goes to their respective electrodes and form a layer surrounding them called the Stern double layer[81] (see Figure 16). This double layer is the main ion that comes into contact with the electrode, which forms the inner Helmholtz layer, and due to the coating of a specific ion, the overall charge created by said ion attracts the corresponding counter ion, forming the outer Helmholtz layer. For example, in the cathode a layer of cations from the supporting electrolyte will form, and due to the overall positive charge of the inner Helmholtz layer, the anion from the electrolyte will also diffuse towards the cathode, forming the outer Helmholtz layer. The outer Helmholtz layer is usually some mixture between the counter ion and the ion itself, as it is loosely attracted to the inner Helmholtz layer *via* coulombic interactions. The potential measured with the potentiostat is between the working electrode and the diffusion layer, which starts where the outer Helmholtz layer ends, and were electrons move between one electrode to another. The stern bilayer is crucial for the measurement of current and potential of the experiment, as it does not allow for the analyte to move close to the electrodes. The movement of ions would create a current by itself which would interfere with the current created by the movement of electrons generated in the redox reactions of the compound, and thus mitigating said movement as much as possible is recommended to obtain accurate data from the reactions happening within. Because of this, the concentration of the supportive electrolyte is higher than that of the analyte.

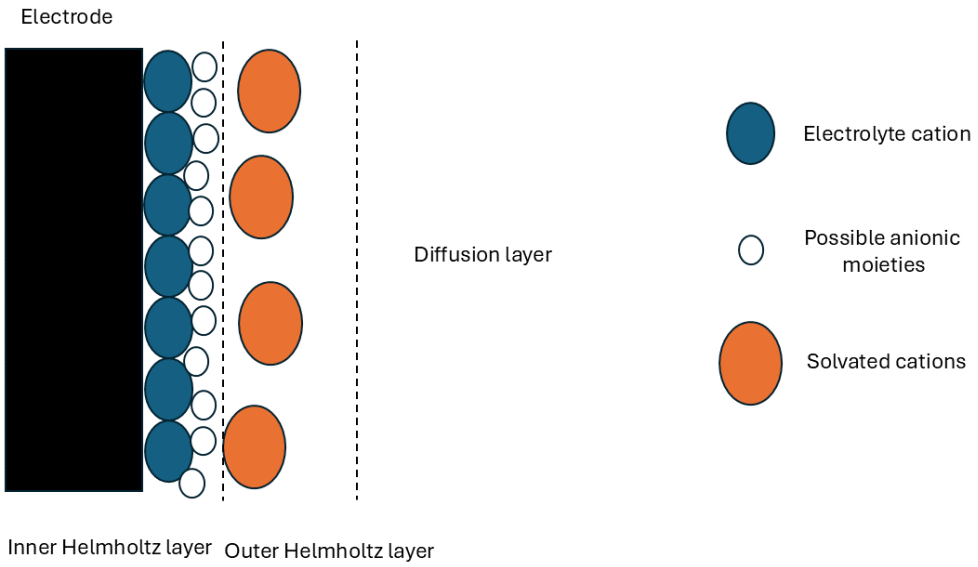

Figure 16: Diagram showing the Stern layer near an electrode, with inner and outer Helmholtz layers (simplified)

1.6.3. Understanding CV results

As mentioned previously, a cyclic voltammogram results from a steady increase of potential across a potential window, and back again, and this provides a plot of current-voltage typically observed in cyclic voltammetry.

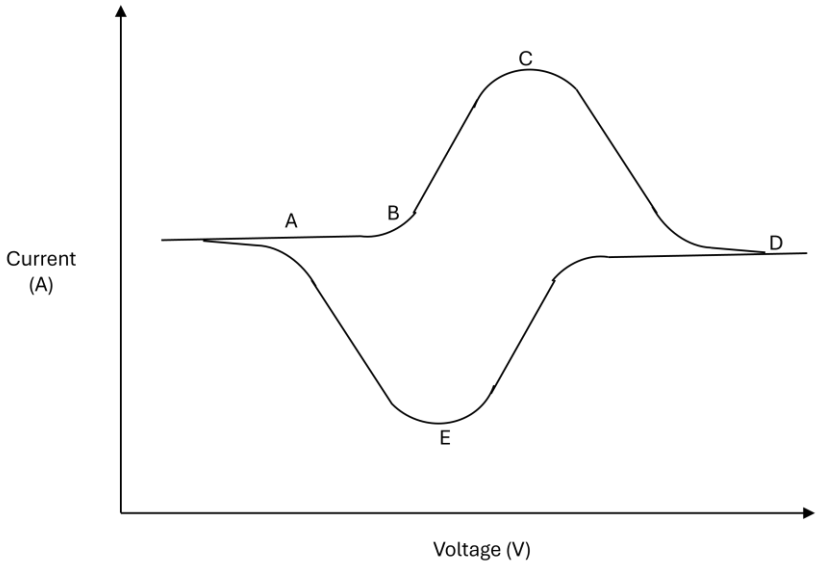

Figure 17: A simple current – voltage graph sketch

In order to understand these types of plots, two factors have to be considered: the diffusion rate in which the oxidised/reduced species moves back into the diffusion layer (mentioned previously) and the Nernst equation.

$$E_{input} = E^0_{compound} + (RT/nF).\ln([Ox]/[Red])$$

The Nernst equation[23, 74, 79] shows how the input of potential E causes the concentration of either the oxidised species or the reduced species near the electrode change based on the potential needed for the redox reaction to happen ($E^0_{compound}$). R is the gas constant, T is the temperature in Kelvin, F is the Faraday constant, and n is the amount of electrons taken or received in a specific redox reaction. This equation explains the duck shape of the plot.

At first, because E_{input} is smaller than $E^0_{compound}$, the concentration of the reduced species is much larger than the oxidised species (A), which makes sense as no redox process would happen at the start of the experiment. However, as the potential increases, the concentration of the oxidised species increases until it will reach a point (B) in which the concentration of the oxidised species is large enough to be considered against the reduced species. This means that the potential is high enough for some noticeable oxidation to occur, and thus the current will start increasing. With this, it is also worth mentioning that due to the increase in concentration of oxidised species near the electrode, the oxidised species slowly diffuse into the diffusion layer within the CV set up, but at a slower rate than the oxidation occurs.

This increase continues as the E_{input} becomes larger and larger, increasing the redox rate, increasing the current obtained as well as the concentration of oxidised species, and reducing the concentration of reduced species. Eventually, the E_{input} surpasses the $E^0_{compound}$ (where the concentrations of both the oxidised species and the reduced species are equal) and continues getting larger until the current reaches a peak (C), sometimes called anodic peak. Here there are two factors to have in mind. The first one, is that at this point most of the reduced species within the CV set up has been depleted, and thus the concentration of oxidised species stagnates. The second one, is that due to the increase in oxidised species concentration near the electrode, the diffusion rate is at its highest. These two concepts combined makes the concentration of the oxidised species collapse, allowing for a more equal distribution of oxidised species in the solution, and a decrease in current as the redox reaction is halted, reaching point (D), and finishing what is commonly called as anodic current (as oxidation occurs in the anode).

Point (D) is determined *via* consideration of the molecule, as it is placed shortly after the final peak is achieved, as no other electrochemical reactions will occur. This is the limit of the potential window, and from this point forward the potential will start to decrease. This causes a similar process to the one in the anodic current, called cathodic current. Here, the inverse of what was described above occurs. The decrease in voltage allows for some of the oxidised species to become reduced, and due to the low concentration of the reduced species the diffusion of it is low. As time passes, the concentration of the reduced species becomes noticeable, and the current dips as the reduction rate increases. The decrease current passes the $E^0_{compound}$ point, in which most of the oxidised species will now become reduced and eventually causing a cathodic peak (E). Here, there is very little amount of oxidised species left, and thus the

concentration of the reduced species stagnates, which in combination with the peak of diffusion rate caused by the elevated concentration of reduced species, allows for a decrease in its concentration around the electrode. As the E_{input} continues to decrease, the redox rate also decreases, increasing the current, and allowing the system to achieve similar conditions to that at the start of the experiment.

As observed from the graph, both the cathodic and the anodic peaks are not in the exact same position. This is caused by a process known as overpotential[5, 18, 31, 53, 54, 65]. Although the $E^0_{compound}$ is a fixed value, when oxidising the solution may require some extra potential to force the redox reaction to start, in a similar fashion to the extra energy required in exothermic reactions to occur. Similarly, when dealing with reduction, a lower potential is required. This causes the mismatch between the peaks, and thus in order to calculate the $E^0_{compound}$ of the molecule, an average between the anodic peak and the cathodic peak is used.

In a standard CV cycle, the peaks can also give information of the type of redox reaction which is occurring. If the peaks are of similar height, then the redox reaction is reversible. However, if one of the peaks is significantly higher than the other, it can be considered quasi-reversible, where one redox pathway is much more favourable than the other. If there is only one peak, instead of two, then the redox reaction is irreversible.

1.6.4. Electropolymerisation[8, 26, 27, 35, 62, 66]

There are two types of electropolymerisation: reductive and oxidative (see Figure 18). The only difference is if an electron is added (reductive) or taken away (oxidative), however it is this difference which have big implications on the types of molecules which can undergo them. In reductive electropolymerisation, compounds usually are carbon only in their electrochemically active moiety, such as vinyl compounds. On the other hand, for oxidative electropolymerisation electron-rich cyclic compounds are required, and thus it is very common to see heteroatoms within the electrochemically active cyclic moiety.

A key aspect of oxidative electropolymerisation is the formation of radicals stabilised *via* resonance structures. For the process to be successful, in one of the resonance structures of the monomer/oligomer the radical must be found in the heteroatom within the electrochemically active cyclic moiety of the molecule, as this increases the stability of the radical. For this to be true, the LUMO of the molecule must not lie within the electrochemically active cyclic moiety of the molecule, as it will result in the radical not being observed in the heteroatom.

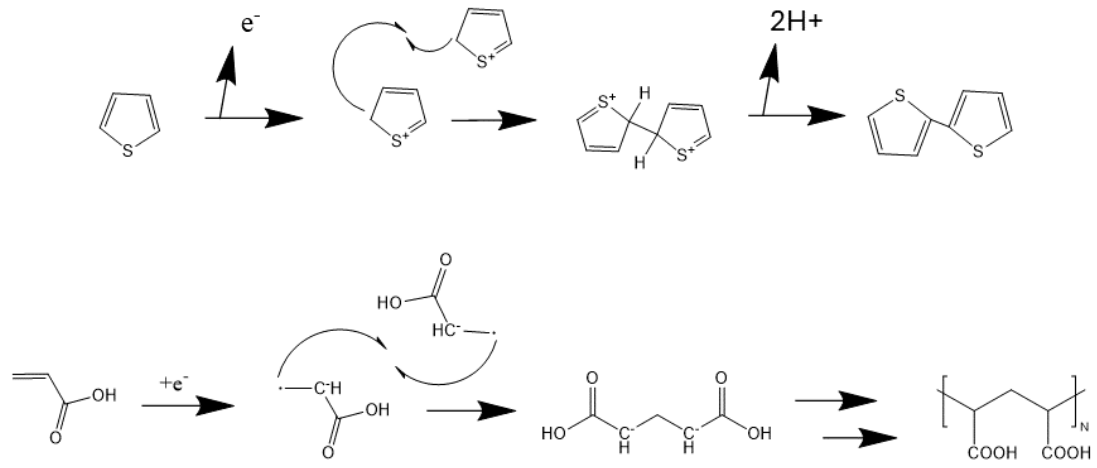

Figure 18: Oxidative (up) and reductive (down) electropolymerisation examples

Electropolymerisation can usually be observed within a CV plot. When the potential is increased and decreased back to its original value through a potential window, this is called a scan. When electropolymerising, multiple scans are required, as the first scan usually allows for dimers to form, and following scans start creating the layers of the film on the working electrode. This can sometimes be visible, but the current-voltage graph shows if any actual electropolymerisation is occurring. A classic one scan CV has been explained previously, however, the second scan usually produces slightly higher current throughout, and it continues increasing with subsequent scans[30, 85]. If these spacings are even, then electropolymerisation is occurring. This is proven by the fact that when a dimer forms, its higher conjugated system allows for it to be easier to become oxidised, meaning that under the same potential more current can be collected. This is also true with longer oligomers, as longer chains are formed, the higher the conjugation, and thus easier to oxidise. If no increase between peaks is observed, then further polymerisation is not occurring (or it simply does not occur).

A similar pattern can be observed with scan rate. With an increase in scan rate, there is an increase in current obtained, as seen by the Randles – Sevcik equation[87, 90].

$$I_p = 0.4463.nFAC.((nFvD)/RT)^{1/2}$$

I_p is the peak current, n is the number of electrons displaced, F the faraday constant, A is the area of the electrode, C the concentration of the solution, v the scan rate, D the diffusion coefficient, R the gas constant and T the temperature.

F, R and T are constants and thus the formula can be simplified to

$$I_p = 2.69 \times 10^5 . n^{3/2}AC.(Dv)^{1/2}$$

Within an experiment A, n and C are constants, and thus it can be clearly seen that current is proportional to scan rate (see Figure 18). This is because the higher the scan rate, the concentration of the oxidised or reduced species increases at a faster rate, and thus the diffusion rate peak becomes higher as the concentration gradient between the surface of the electrode and the diffusion layer within solution is greater.

This relationship is very important, as sometimes the difference between peaks are very small, and a peak current – scan rate plot can be proven useful. If the general pattern is increasing, then electropolymerisation is occurring, even if it stagnates eventually (stagnation just means there is a limit to the thickness an electropolymerised film can achieve).

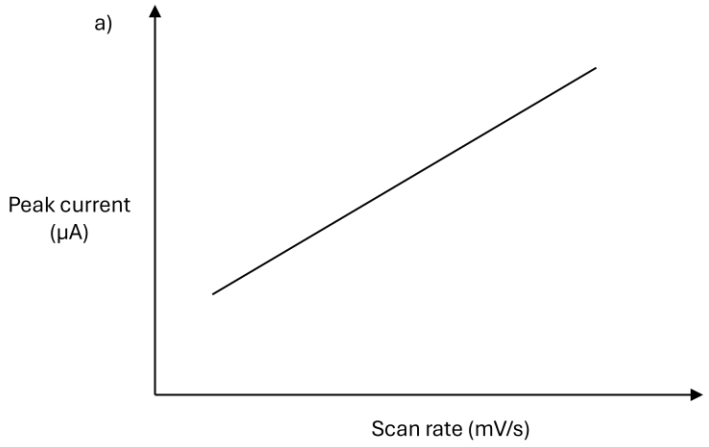

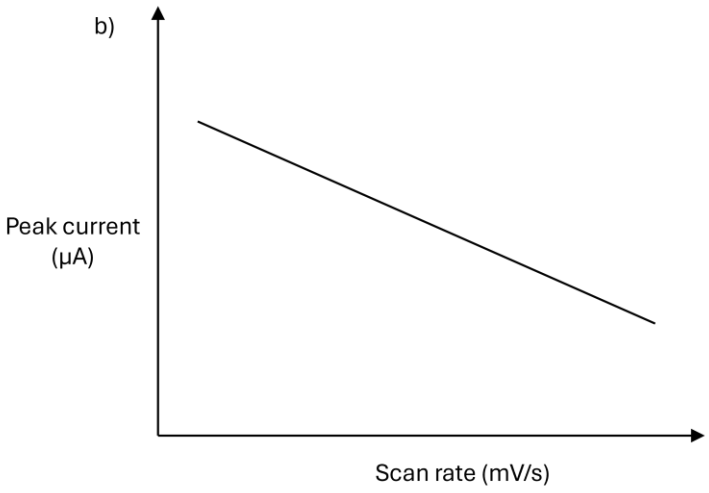

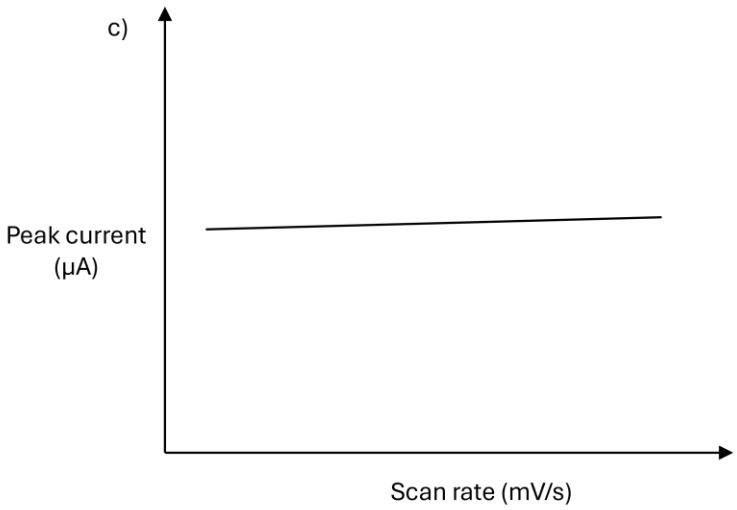

Figure 19: Scan rate vs peak current graph sketches, with a good example (up) and two examples which show no electropolymerization occurring (down)

An important factor when dealing with electropolymerization is that all measurements must be referenced against Fc/Fc^{+}, as this compound has an E^{0} at 0.0 V, and thus any changes caused by physical differences in the set up (eg. Change of reference electrode) between measurements can be normalised.

1.7. Standard molecules

When dealing with new molecules, it is customary to have a reference molecule which has proven to work in plenty of scenarios to which compare any new molecules synthesised. This reference usually requires to be somewhat similar to the compound being investigated in order to place the measurements of the new molecule into context. For HTMs, this molecule is Spiro – OMeTAD (see Figure 20). This molecule has consistently proven to perform at over 20% PCE and has been considered the best small molecule HTM (for the high PCE as well as for high reproducibility, amongst other reasons), and thus the universal reference compound. It is crucial to pinpoint, however, that it does have mayor setbacks, and these are the reasons for the research for a new HTM for PSCs. Some of the problems encountered are the expensive procedure required to synthesise, the necessity for the addition of dopants (some of them hydroscopic) to improve its low conductivity and the increasing instability at 85 $^{\circ}$C, which are very important considerations when dealing with PSC components.

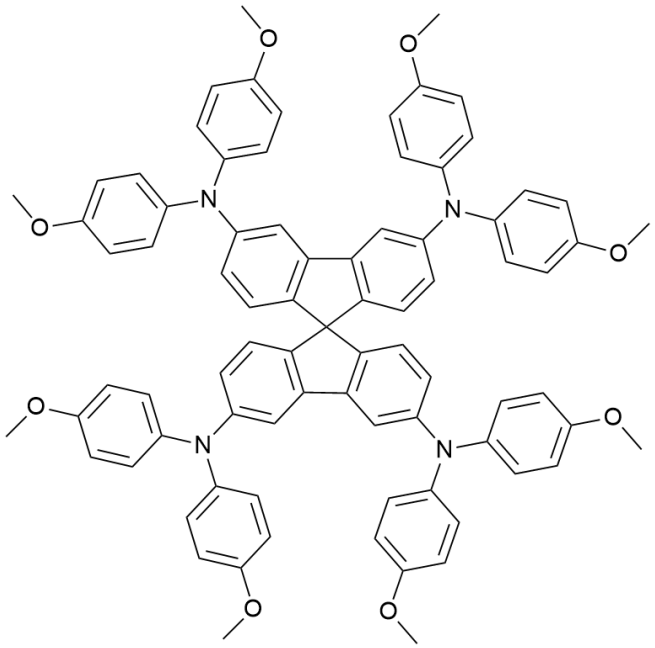

Figure 20: Spiro - OMeTAD

In this thesis, the focus is in electropolymerisation, and non-polymeric Spiro – OMeTAD is not usually deposited by electropolymerisation. Thus, in terms of performance standards, there are two other molecules that could be useful: PEDOT:PSS and PTAA.

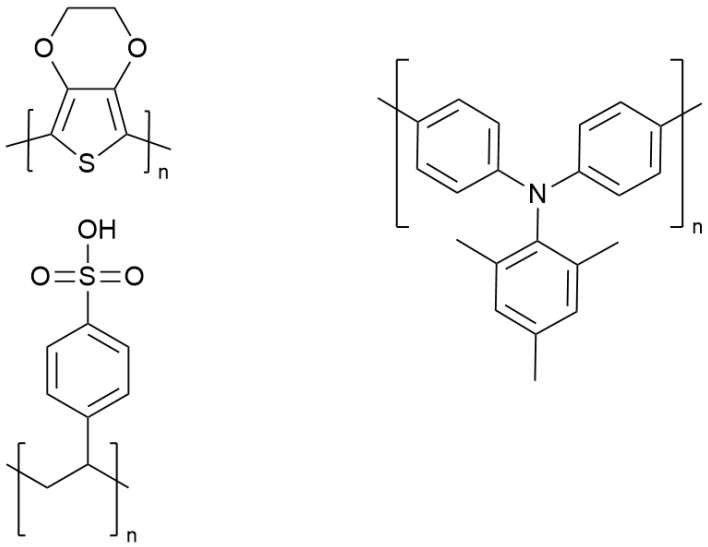

Figure 21: PEDOT: PSS and PTAA

PEDOT:PSS has the advantage of having very high conductivity compared to Spiro – OMeTAD, but this is due to the ionic nature of the bonding between the PEDOT moiety and the PSS moiety. Thus, PEDOT:PSS, although a well-performing HTM, it could not be applicable as a reference to our molecules. PTAA, in the other hand, could be a good contender for a reference compound, as it does have a similar electrochemical structure to some of our compounds. It does have very high resistivity and wettability issues (the latter being a main point if other film laying techniques were to be used), which are considerable drawbacks.

However, two other reference molecules have been used, one of them as it has proven to be electropolymerisable, and due to the focus on the electropolymerisation layer deposition aspect of the project (as well as the inclusion of further data of the reference compound in question), it has deemed an adequate reference to use; and the other due to its proven capacity to be an HTM and its capacity to electropolymerize. (See more information concerning these molecules in the next section).

Aims and objectives

The first aim of the project is synthesizing the following molecules, two already made (with one of them already used as an HTM and the other already electropolymerized) to be used as reference molecules (as well as completely characterize them), and two new molecules based on the carbazole and the EDOT moieties, respectively

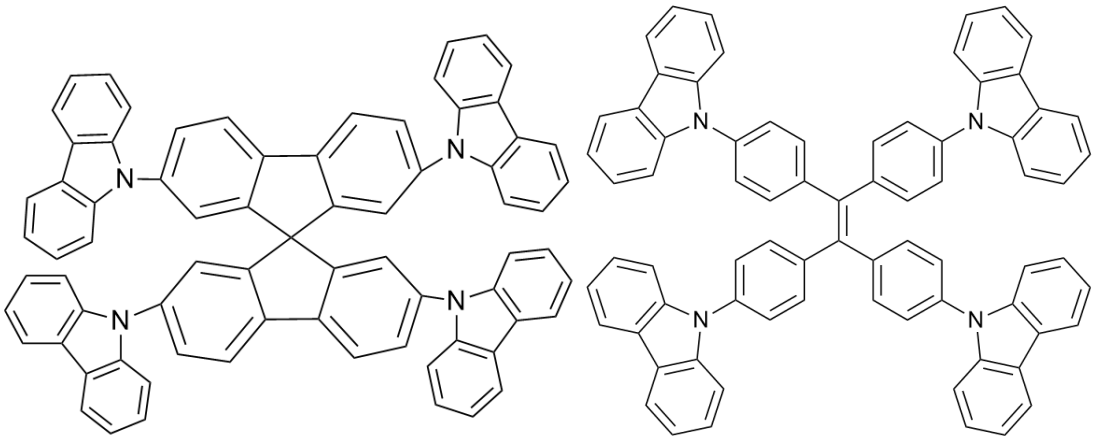

Figure 22: The two reference molecules, the left one already presented as an HTM by Shuo Yang *et al.*[94] (PSA-006) and the right one already electropolymerized by Venkata Suresh Mothika *et al.*[93] (PSA-013)

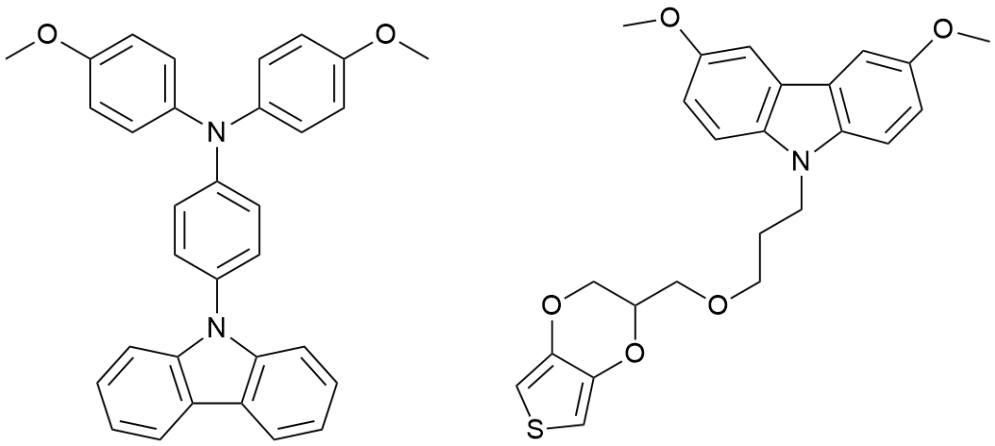

Figure 23: The two newly synthesized molecules, the carbazole based one (left) (PSA-025) and the EDOT based one (right) (PSA-027)

Once the molecules have been synthesized, they will then be tested to see if they have the capacity to electropolymerize onto ITO plates. Once the films have been characterized (e.g. FTIR and UV-vis spectroscopy), the film thickness and conductivity of the films will be investigated.

2. Results and discussion

2.1. Synthesis discussion

As mentioned in the Aims section, the objective of this project is to synthesize electropolymerizable HTMs, and electropolymerize a thin layer of the HTMs onto ITO substrate for conductivity measurements. **PSA-006** and **PSA-013** have already been produced and electropolymerized successfully. **PSA-006** have already been tested within an HTM context, which demonstrated good results due to π – π stacking interactions between layers, which aid intermolecular conductivity. **PSA-013** has not been observed within an optoelectronic context, but similarly to **PSA-006**, it is highly conjugated and could form π – π stacking interactions between layers, so it was suspected that it would perform similarly.

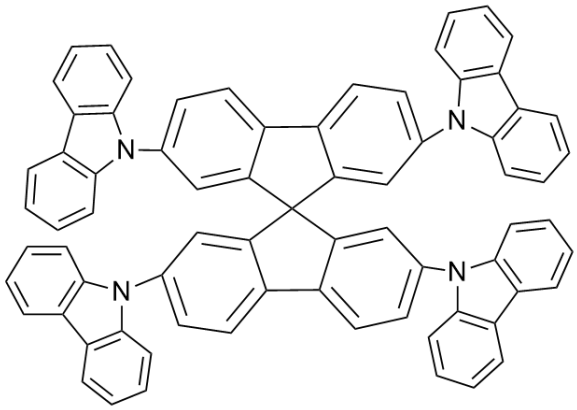

Figure 24: **PSA-006**

For **PSA-006** (Figure 24), the methodology used was the one reported by Shuo Yang *et al.*[94]. The first step was a halogenation in carbons 2, 2', 7 and 7' of 9,9'-spirobifluorene *via* an electrophilic substitution using $FeBr_3$ as a Lewis acid and bromine. ^1H NMR showed that the reaction was successful (Yield = 98.0%), and pure enough for the following reactions.

The methodology reported an Ulmann coupling using CuI as the catalyst to attach carbazole groups into the now activated spiro core (**PSA-007**). However, with the conditions reported, ^1H NMR showed that no reaction occurred.

To overcome this, a Buchwald Hartwig reaction was then attempted (**PSA-008)** with a palladium catalyst, XPhos as a ligand, and toluene as the solvent, but ^1H NMR showed similar results as the previous reaction. A Suzuki coupling was then attempted (**PSA-009**), under the presence of a boronic acid, a palladium catalyst, and a solution of THF and water. However, ^1H NMR revealed mostly starting material. K_2CO_3 was used, which is a weak base, which in combination with the likely steric hinderance could explain the unsuccessfulness of the reactions proposed.

Finally, a second attempt at the methodology reported was performed, but o – dichlorobenzene was substituted with DMA, and 2,2' – bipyridine with 18 – crown – 6, with the intention of enhancing the performance of the base without the need for a stronger one, as side reactions may occur. Unfortunately, the ^{1}H NMR of the suspected product was not consistent with the structure of the target molecule.

After some consideration, it was decided to move into the synthesis of **PSA-013**, as **PSA-006** was proving too difficult to synthesise.

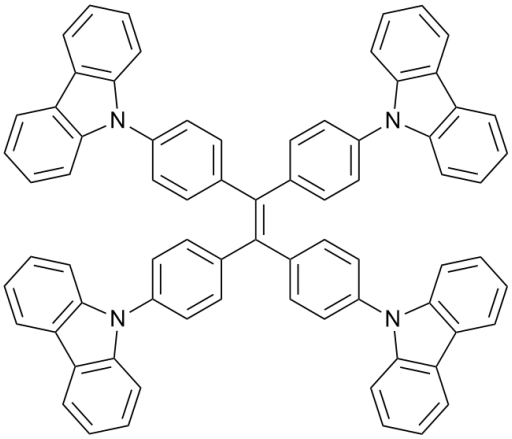

Figure 25: **PSA-013** [14, 57, 58, 77, 89]

PSA-013 (Figure 25) was synthesized as reported by Venkata Suresh Mothika *et al.*[93], by performing an electrophilic substitution reaction to add the carbazole onto the bis(4 – fluorophenyl)methanone, followed by a McMurry coupling to attach two molecules made in the previous reaction together through the double bond.

The electrophilic substitution (**PSA-012**) was carried out by using t-BuOK as a base and DMF as a solvent in a stepwise reaction by adding the reagents first and then t^{h}e ketone in solution to increase reaction control. ^{1}H NMR demonstrated the presence of the target compound (Yield = ~44%) and pure enough for the following reaction.

The McMurry coupling was then carried out by cooling the mixture of the reagents to -78˚C to have a controlled initial interaction between the $TiCl_4$ catalyst and said reagents. After a few minutes, the reaction mixture was heated to reflux and monitored by TLC. This resulted in the target compound being produced (confirmed by ^{1}H NMR) (Yield = ~33%) with no side product detected. Approximately 350 mgs were collected for future characterisation and electropolymerisation.

After synthesising **PSA-013,** the two novel molecules were synthesized, the first one being **PSA-025**.

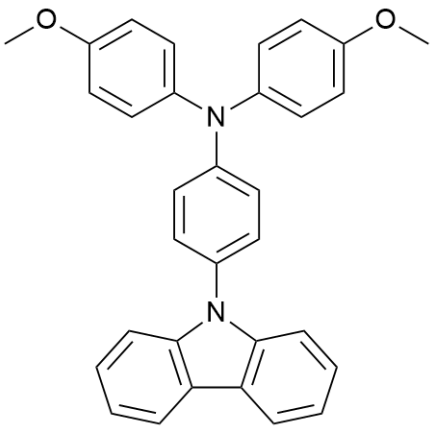

Figure 26: **PSA-025** [32, 43, 45, 46]

For comparative purposes, this molecule was designed to have an electropolymerizable carbazole moiety. The first step of the synthesis is a nucleophilic substitution, followed by a reduction of the nitroxide group into an amine, and finishing with an Ulmann reaction.

The nucleophilic addition of 4-fluoronitrobenze to carbazole (**PSA-014**) was carried out without an issue. The reaction produced the target compound in satisfactory amounts (Yield = 78.0%) and good purity after a methanol washing. The reduction step of the nitroxide group (**PSA-015**) was monitored *via* TLC, and after pouring the reaction mixture into ethanol and water the reaction was confirmed to be successful through ^{1}H NMR, but the compound was proven to be difficult to handle as some of it was left behind during the purification of the target molecule.

During the Ullmann reaction (**PSA-016**), the reaction was monitored through TLC, and extra 4 – iodoanisole was added when necessary to ensure the completion of the reaction, minimizing the presence of the monosubstituted amine. Column chromatography (1:19 ethyl acetate and petroleum ether) was performed after DMA was extracted with a solution of acetonitrile. An ^{1}H NMR was carried out, but the amount of product used was negligible. Thus, the reduction and the Ullmann were repeated with the rest of the nitroxide formed in **PSA-014**, but the amine produced during the second reduction (**PSA-017**) was directly transferred into the second Ullmann reaction (**PSA-018**) without any purification to avoid spillage. Column chromatography was carried in the same conditions as before, and after ^{1}H NMR confirmed the presence of the target molecule within the fractions, a second column was performed to ensure the extraction of as much amount of the product as possible, collecting 64.3 mgs.

This reaction pathway was repeated reactions **PSA-023** (nucleophilic attack), **PSA-024** (reduction), **PSA-025** (Ulmann reduction) (Figure 26) later to upscale the production of the final target compound, resulting in an extra 235 mgs.

After the synthesis of **PSA-025**, **PSA-027** was synthesized.

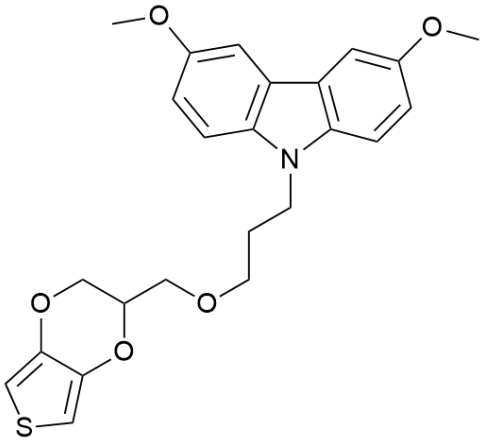

Figure 27: **PSA-027**[10, 14, 34, 39, 60, 64, 75, 86]

PSA-027 (Figure 27) was designed to have closer to a SAMs HTM structure instead of a CMP, but for comparative purposes with the previous compound, the dimethoxycarbazole was chosen as the "head" of the molecule.

The reaction pathway for this molecule was the nucleophilic substitution of 1,4-dibromobutane to dimethoxycarbazole, and a follow up nucleophilic substitution to connect the bromobutane moiety to EDOT. A few attempts were made with previous designs of the molecule, with the use of 1,4-dibromobenzene instead of the alkane, but the reaction between this molecule and the EDOT would not be viable.

The initial nucleophilic substitution (**PSA-026**) was followed by TLC, and after column chromatography (1:9 ethyl acetate: petroleum ether) ^{1}H NMR confirmed the presence of the target molecule and overall, the reaction gave a yield of 28.0%.

The second nucleophilic substitution (**PSA-027**) was also followed by TLC, and the resulting new compound was confirmed by ^{1}H NMR to be a side product produced by the elimination of the bromine in the alkyl bromide to form an alkene. Although there was desired product in other fractals collected in the column chromatography, a weaker base would perhaps result in a higher yield than the one produced with NaH (14.5%), which resulted in ~100 mgs of the target molecule. Fortunately, these two products react differently under vanillin in TLC, with the desired product staining pink, so the formation of each product can be easily monitored.

2.2. Characterization

2.2.1. Optical characterization [7, 12, 38, 49 83, 99]

For UV-vis absorption, stock solutions with concentrations of 1.0 x 10^{-5} mol/dm^3 were made as needed for each compound but with different solvents. For **PSA-013**, the stock solution was in chloroform and for **PSA-025** and **PSA-027** it was in DCM. The change from chloroform to DCM was caused due to the lack of solubility of **PSA-025** and **PSA-027** in chloroform. For fluorescence spectra, the solutions were the same ones used in UV-vis, but the concentrations for **PSA-013** and **PSA-025** is 1.0 x 10^{-4} mol/dm^3, while the concentration used for **PSA-027** is 1.0 x 10^{-6} mol/dm^3.

The UV-vis and fluorescence spectra can be observed in Figures 26 – 28, and the data collected in Table 1.

UV-vis absorption is an experimental procedure to calculate the energy gap between the HOMO and the LUMO of the compound, as well as seeing its absorption. Ideally, the absorption of the compound would not interfere with the absorption of the perovskite (600 – 850 nm) so as to not interfere with the device's efficiency, as well as a high energy gap to ensure high $R_{recombination}$, caused by the difficulty that the electron will experience to relax back to its ground state. To calculate the energy gap, the wavelength of the onset is required as observed by the following formula:

$$E_{gap} = hc/\lambda_{onset}$$

Where E_{gap} is the energy gap in eVs, h is the plank's constant, c is the speed of light in m/s and λ_{onset} is the wavelength of the onset of the peak in UV-vis spectra. This, alongside the HOMO level (see Electronic characterisation), can be used to calculate the LUMO and determine whether the compound has energy levels appropriate for the perovskite device.

Fluorescence spectroscopy[25], on the other hand, is used to calculate the Stokes Shift. This is calculated by subtracting the fluorescence peak with the highest absorption peak from the UV-vis spectra. When an electron absorbs a photon and raises to its excited state, the energy that it holds can be either released fully with a photon of similar wavelength to that of the original photon, which would result in a low Stokes shift, or part of the energy can be used by the molecule and the solution for vibrational relaxation as well as solvent reorganization, which would result in a high Stokes shift. Ideally, if a compound is fluorescent, a low Stokes shift would be desired, as it suggests that the energy of the photon is used efficiently within the device and not wasted as thermal energy (due to vibrational relaxation and solvent reorganization), also called non-radiative recombination loss.

The measurements were taken at the same time, with **PSA-013** made first, then **PSA-025**, and finally **PSA-027**.

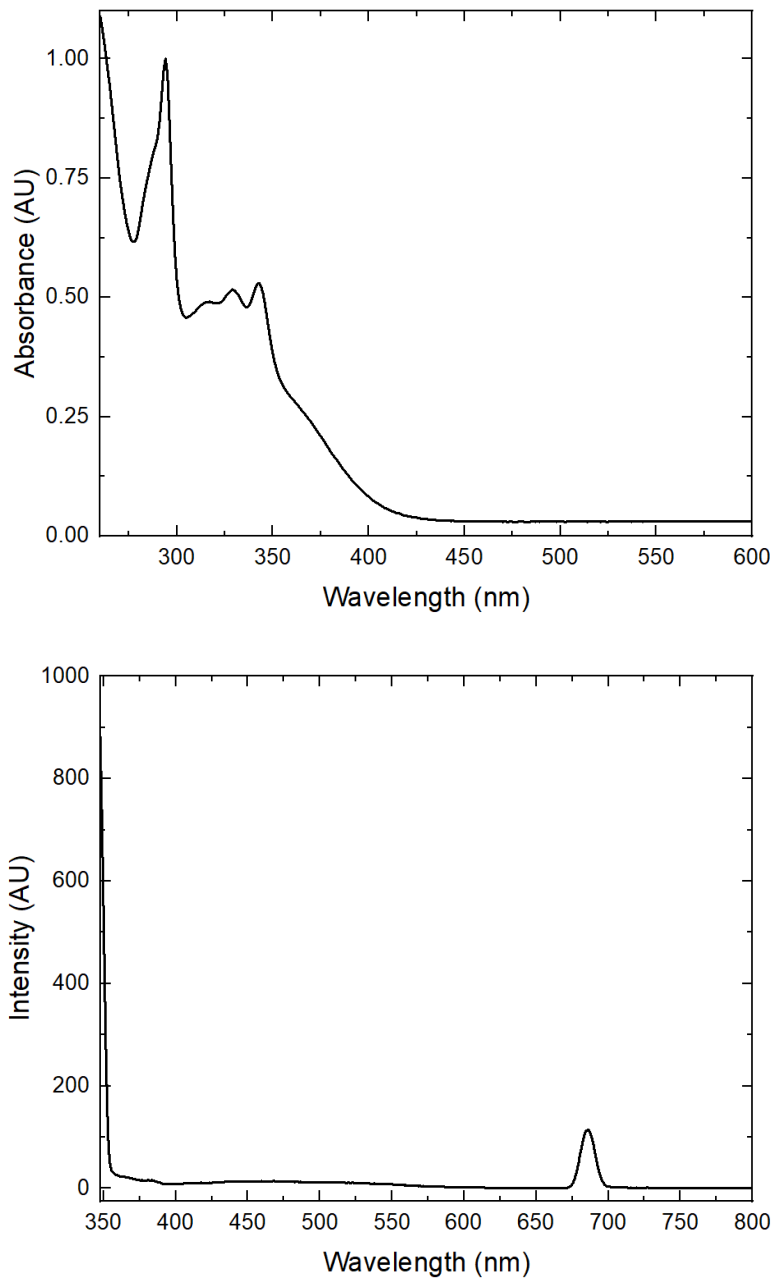

Figure 28: Graphs of the normalised UV-vis absorbance (top) and fluorescence (bottom) spectra of **PSA-013**

PSA-013 absorbed mostly the 300 nm wavelength in the UV-vis (Figure 28), with the highest peak being at 294 nm, and to a smaller extent from 300 nm – 350 nm, which corresponds to the ultraviolet range of the spectrum. Furthermore, the compound would be a good complementation to the natural absorption range of the perovskite (600 – 850 nm). The absorption onset is found at 410 nm (on the violet range), which indicates a large band gap between the HOMO and the LUMO, which would suggest a high $R_{recombination}$.

In the fluorescence spectrum, however, the small peak at around ~680 nm has been attributed to a ghost signal as it is positioned at twice the wavelength of the compound with a much lower magnitude, and thus it could be ignored. Overall, the compound does

not show fluorescence with chloroform and within the wavelength range selected, which could be due to the energy fully quenched by intramolecular vibrational relaxation or solvent collisional quenching.

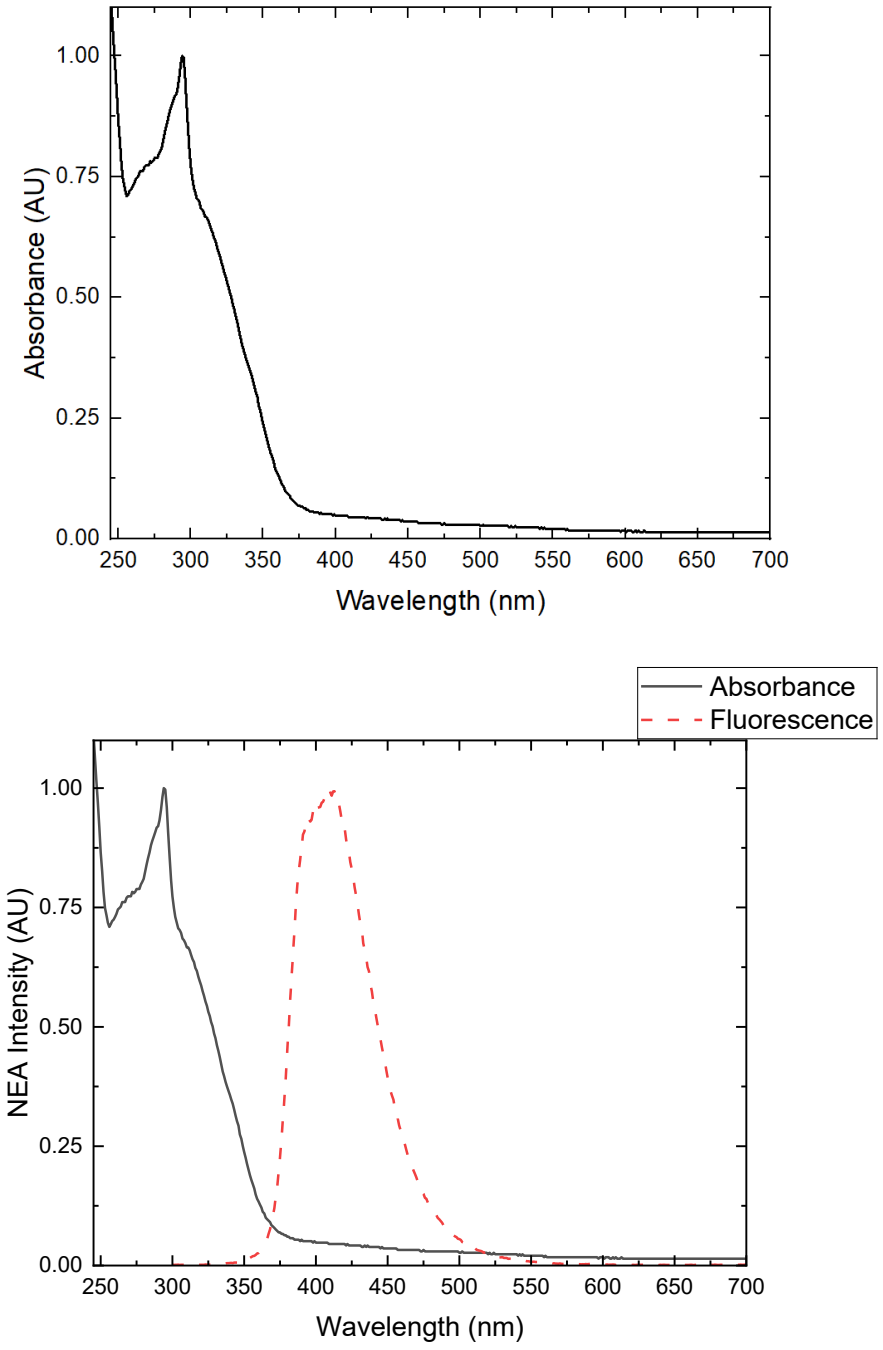

Figure 29: Graphs of the normalised UV-vis absorbance (top) and NEA (Normalised Emission and Absorption) (bottom) spectra of **PSA-025**

PSA-025 absorbs waves on the ~290 nm region, which also corresponds to the ultraviolet region, with the highest peak being at 294 nm (Figure 29). Similarly to the

previous molecule, this does complement the perovskite absorption range, and the absorption onset is on the ultraviolet range (373 nm) indicates a large band gap between HOMO and LUMO, resulting in a high $R_{recombination}$.

In the fluorescence spectrum, the peak is found at 409 nm, and when normalised and compared to the UV-vis, the Stokes Shift is calculated to be 115 nm. This is a high Stokes Shift, which is caused by a high non-recombination energy loss, which would generate a decrease in the efficiency of the excited electron when placed in a device, but this should still be revised *in situ.*

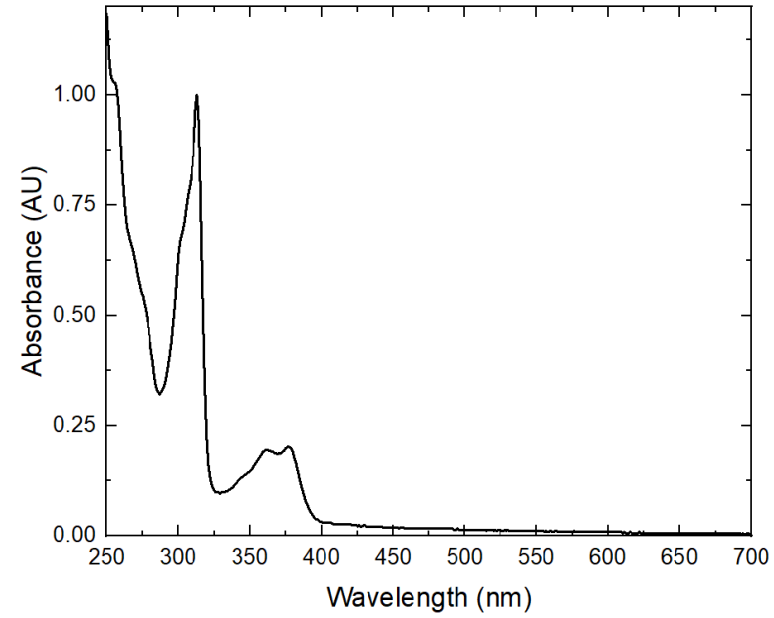

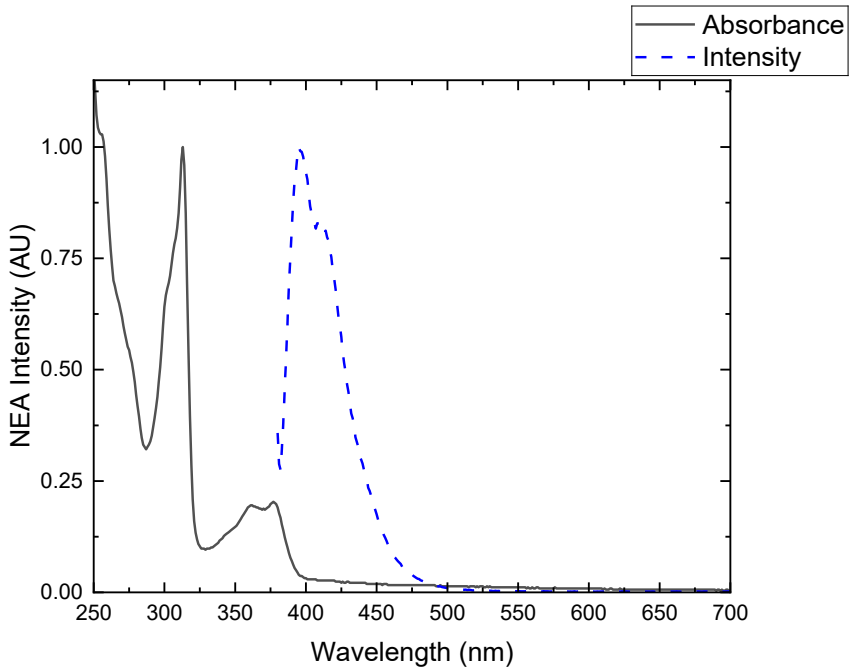

Figure 30: Graphs of the normalised UV-vis absorption (top) and NEA (Normalised Emission and Absorption) (bottom) spectra of **PSA-027**

PSA-027 absorption has a sharp peak at 313 nm, but there is also a broad peak between ~360 nm and ~380 nm which corresponds to the violet range of the visible light, which is compatible with the perovskite's absorption range (Figure 30). The absorption onset lies on the violet region (395 nm), which indicates a large band gap between HOMO and LUMO, resulting in a high $R_{recombination}$.

In the fluorescence spectra the main peak is at 395 nm, with a broad shoulder that encompasses the 405 nm – 420 nm region. Nonetheless, when normalised and compared to the UV-vis absorbance, the Stokes Shift is shown to be 82 nm, which although lower than **PSA-025**, it is still high, suggesting a high non-radiative recombination loss.

-	**PSA-013**	**PSA-025**	**PSA-027**
Onset (nm)	410	373	395
Max. UV point (nm)	294	294	313
Fluorescence (nm)	-	409	395
Stokes Shift (nm)	-	115	82
Energy gap (eV)	3.026	3.327	3.141

Table 1: Optical characterisation data of **PSA-013**, **PSA-025** and **PSA-027**

2.2.2. Electronic characterization[99]

For electronic characterization, 1 x 10^{-5} mol/dm^3 solutions were made with DCM. Both CV and SWV were carried out, CV to observe the compounds' electrochemical behaviours and SWV to obtain the ionisation potential. The ionisation potential, can be calculated using the following formula:

$$E_{IP} = -(E_{ox}^{1/2} + 4.80\ eV)$$

Where E_{IP} is the energy level of the ionisation potential, which is an approximate representation of the HOMO, and $E_{ox}^{1/2}$ is the standard oxidation half reaction potential, which is the voltage that creates the first oxidation peak of the SWV, although the oxidation onset in CV can also be used. Once the HOMO is obtained, the LUMO can be estimated using the following equation:

$$LUMO = HOMO - E_{gap}$$

Where E_{gap} is the energy gap obtained previously in the optical characterization.

For reference, the average HOMO level of perovskites lies around -5.40 eV, while the average LUMO lies around -3.9 eV, although it depends on the perovskite used.

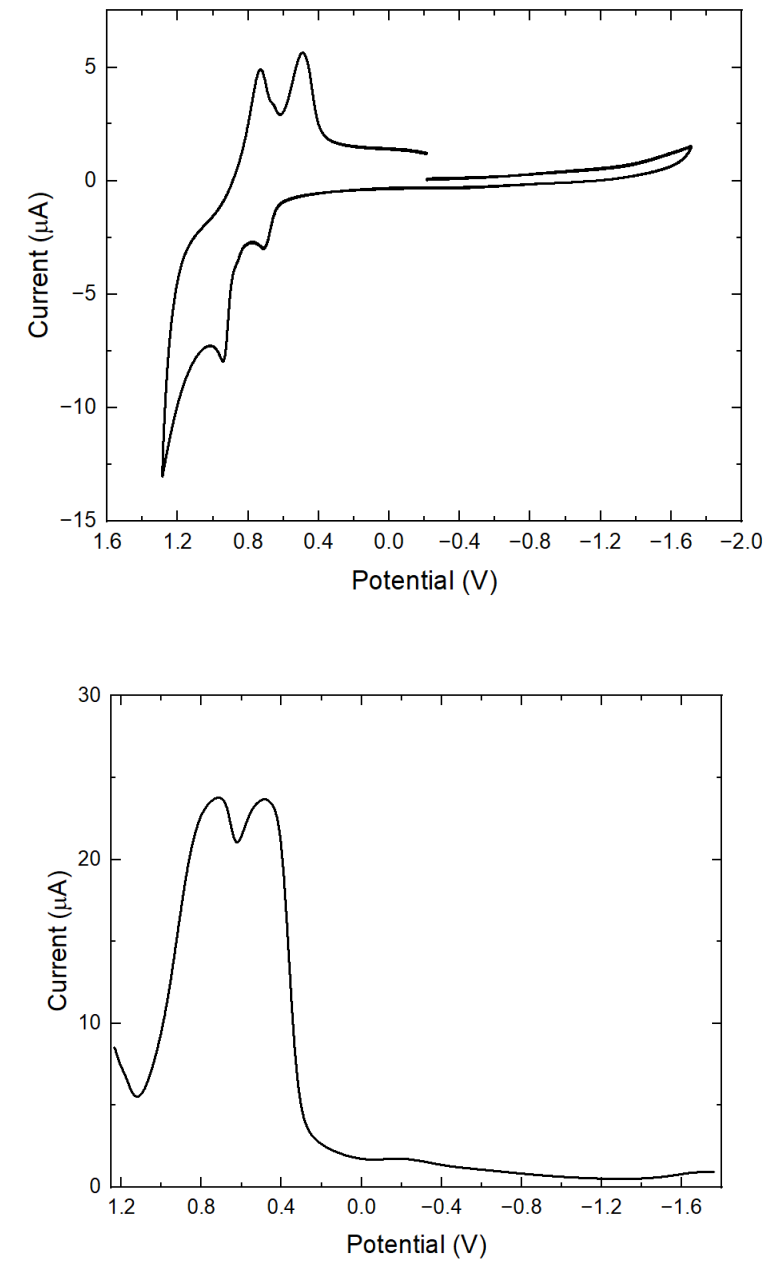

Figure 31: Graphs of the CV (top) and SWV (bottom) of **PSA-013**

In the CV, **PSA-013** (Figure 31) has two peaks in the cathodic wave and their corresponding two anodic peaks, which demonstrate that the redox reaction happening in solution is pseudoreversible and within the electrochemical window (1.60 V - -2.00 V). In the SWV, the estimated HOMO is observed to be -5.32 eV, and the LUMO is then calculated to be -2.29 eV. The HOMO is higher than that of perovskites, and thus it would allow holes to pass, and the LUMO is higher than that of perovskites, and thus it would block any electrons, and avoiding potential recombination (high $R_{recombination}$).

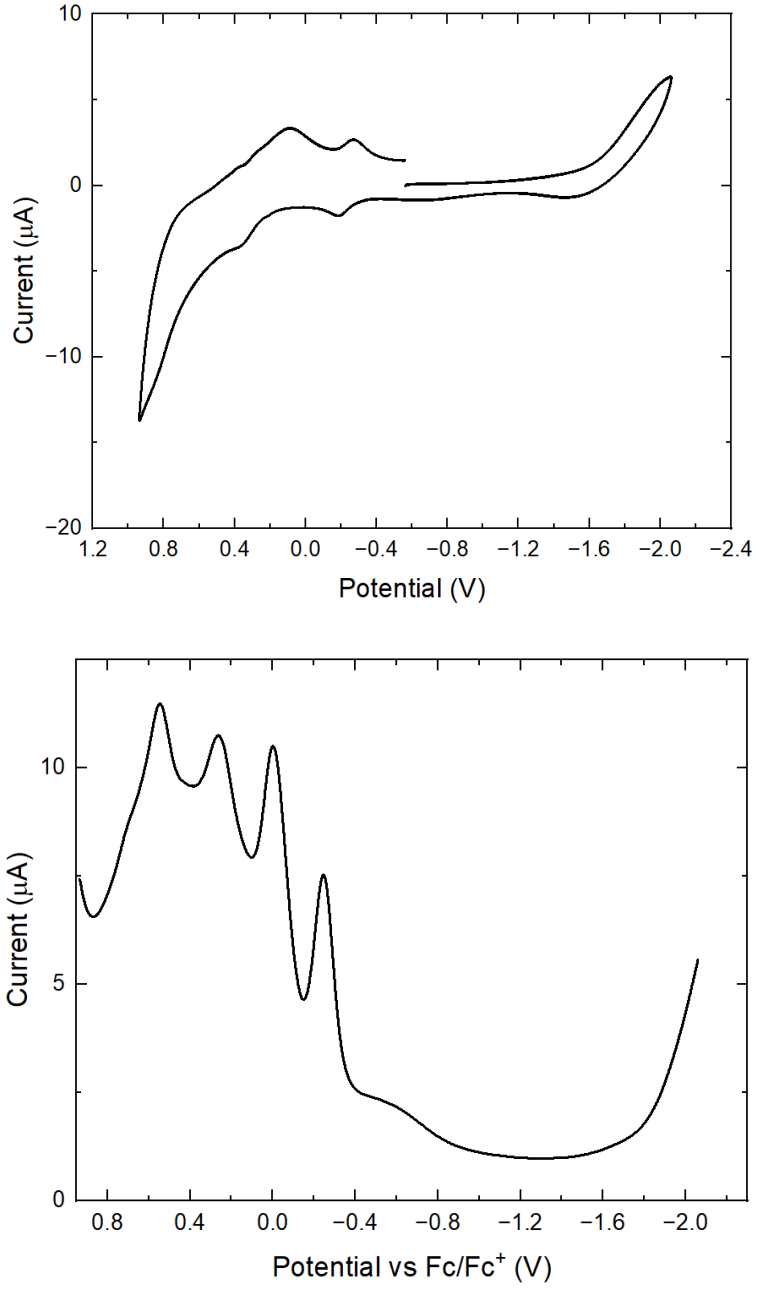

Figure 32: Graphs of the CV (top) and SWV (bottom) of **PSA-025**

PSA-025 shows two clear peaks in the CV (Figure 32), with a broad shoulder around 0.80 V. Due to the shorter electrochemical window, the broad shoulder could be considered a second peak which was cut short, as two peaks in the 0.50 V – 1.20 V region would be attributed to the electrochemical behaviour of the carbazole moiety within the molecule, as observed for **PSA-013**. The SWV shows the three sharp peaks of the molecule, two corresponding to the carbazole moiety (0.60 V and 0.40 V) and the third peak at 0.25 V corresponding to the TPA moiety, with the fourth peak at 0.00 V being the one created by ferrocene. According to SWV, **PSA-025** has an approximate HOMO level of -4.57 eV, and a LUMO level of -1.24 eV. These levels are appropriate for its use as an HTM.

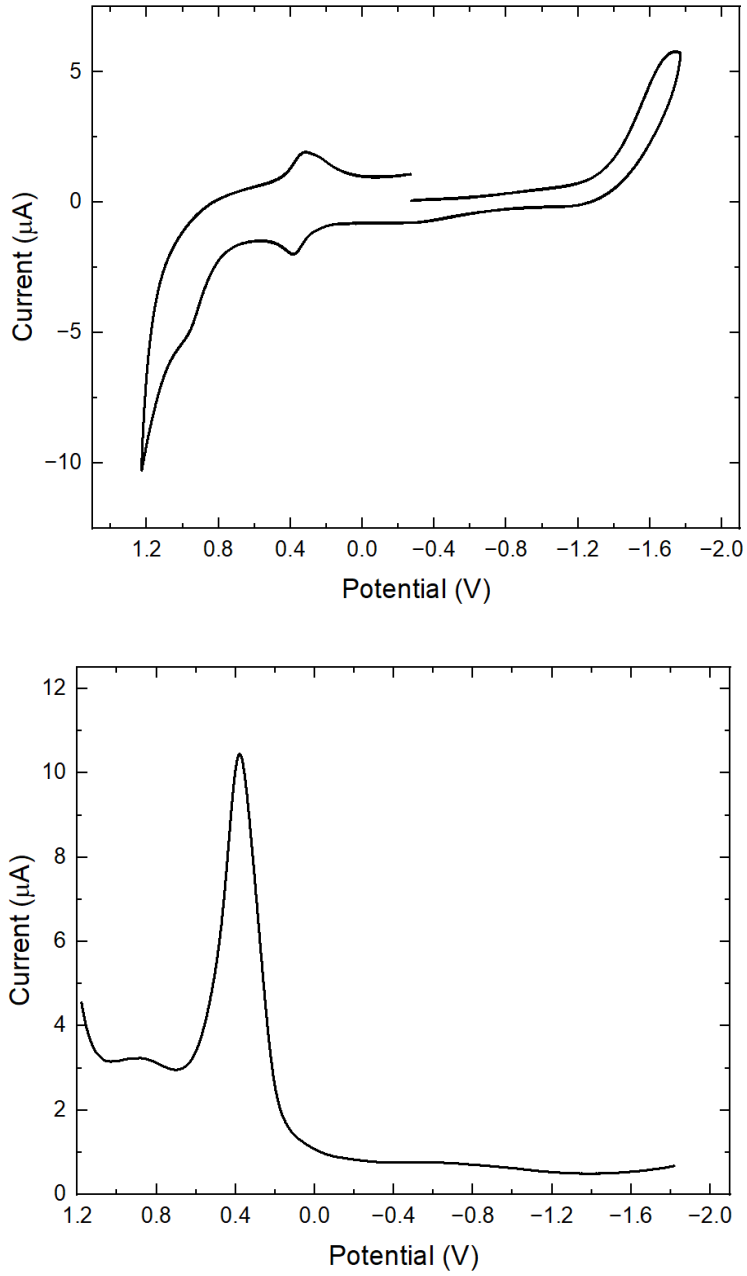

Figure 33: Graphs of the CV (top) and SWV (bottom) of **PSA-027**

PSA-027 (Figure 33) shows a pair of peaks at 0.3 V, which was attributed to the EDOT reversible redox reaction. Two extra peaks should appear for the 2,7-dimethoxycarbazole moiety, but it was presumed to have been displaced by the EDOT moiety and should be found outside the electrochemical window displayed. In SWV, this behaviour is further highlighted due to the increase in current towards the edge of the potential window, suggesting further peaks. The HOMO is approximately -5.18 eV and the LUMO -2.04 eV, which are also values compatible with the ones displayed by perovskites energy levels.

-	**PSA-013**	**PSA-025**	**PSA-027**
HOMO (eV)	-5.146	-4.417	-4.981
Energy gap (eV)	3.026	3.327	3.141
LUMO (eV)	-2.393	-1.089	-1.840

Table 2: Electrical characterisation data of **PSA-013**, **PSA-025** and **PSA-027**

2.2.3. Thermal characterization [99]

TGA and DSC were carried out on these materials to investigate their thermal stability. TGA was carried out to observe if the compounds' decomposition temperature (mass drops below 90%), and DSC to follow any potential glass transition temperature (T_g) that may occur below temperatures of 500˚ C. These two analytical techniques are fundamental to check if a compound could withstand the temperatures within the device and whether there is any change in the 3D structure of a compound which could change its conductivity and be detrimental to the stability of devices.

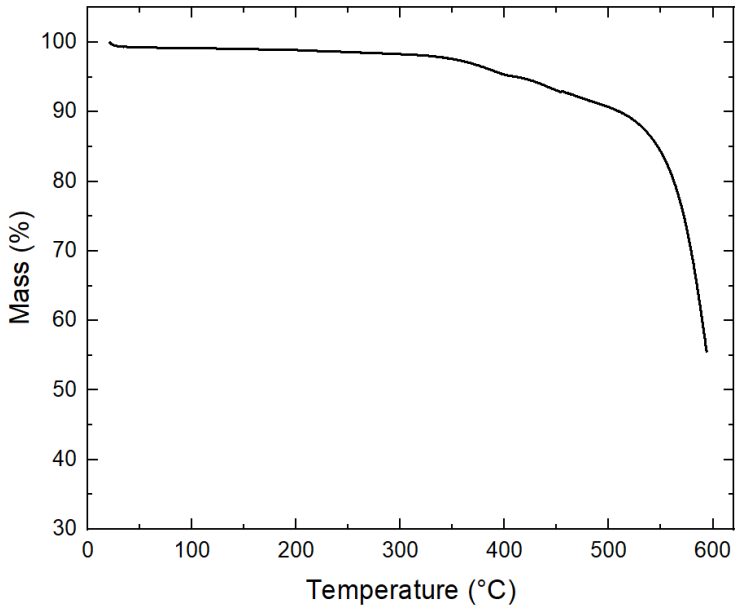

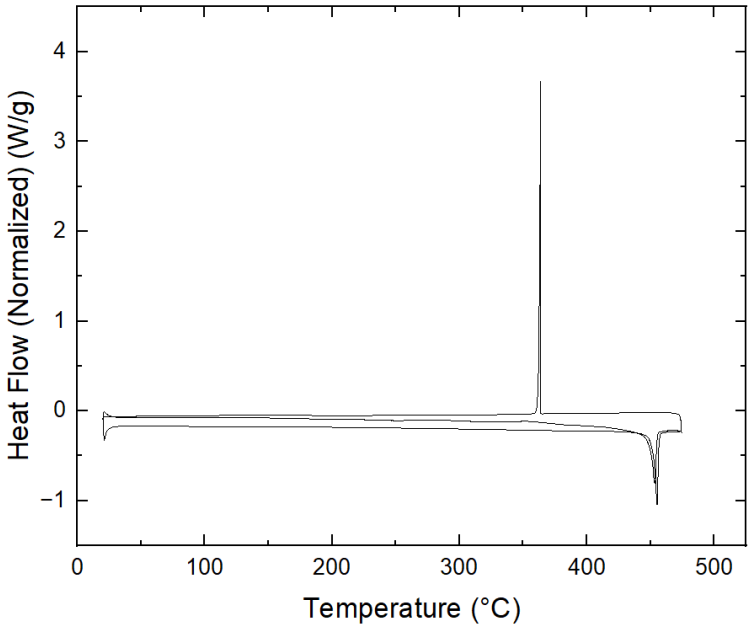

Figure 34: Graphs of the TGA (top) and DSC (bottom) for **PSA-013**

PSA-013 manages to maintain over 90% of its mass until it reaches to 510˚C. This temperature is remarkably high and proves that the compound could be stable within the device. For DSC (Figure 34), the only noticeable peaks are at ~450˚C and at ~360˚C, corresponding to **PSA-013**s' T_g and its melting point. These temperatures are well above the ones found in a device, so the compound should have a stable structure within a device.

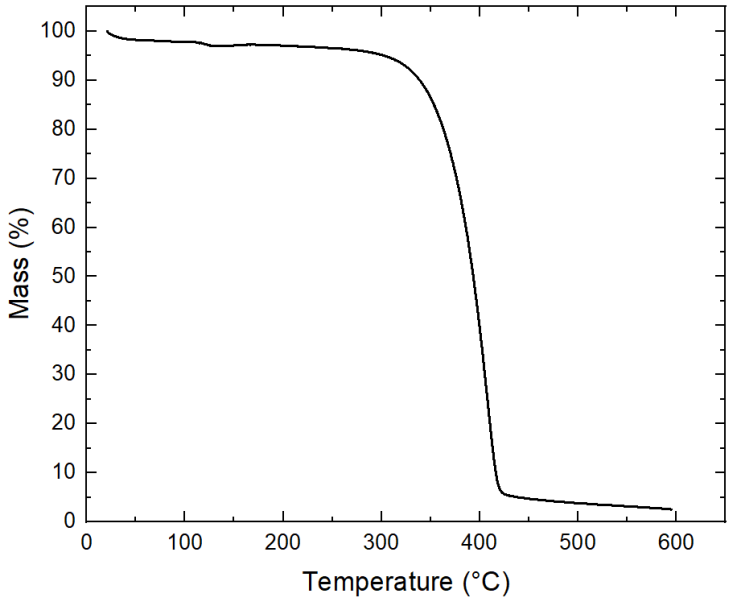

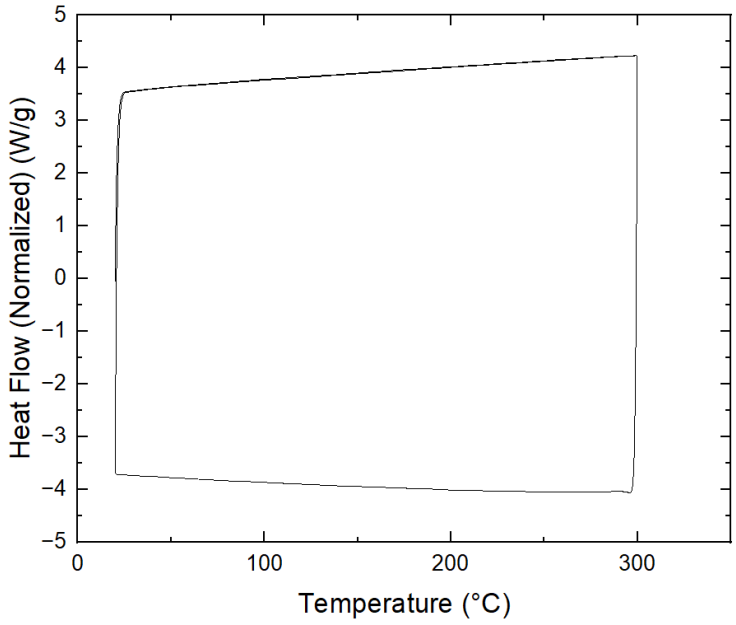

Figure 35: Graphs of the TGA (top) and DSC (bottom) for **PSA-025**

PSA-025 retained most of its mass until the temperature reached 339°C, suggesting that it may be stable within a device. In DSC (Figure 35), no T_g was observed within the thermal window shown above, and thus **PSA-025** would be expected to maintain its structure in a device. Nonetheless, there is noticeable thermal hysteresis upon cooling from 300° C back to room temperature, as the heat flow is different depending on whether the compound is being cooled or not. Usually, hysteresis is an attribute that is not ideal for an HTM, as it implies an intramolecular reorganization which could result in a difference in conductivity. However, due to the symmetry of the hysteresis as well as the heat flow starting and finishing at the same point, this potential change is reversible, and thus although there is hysteresis, it will hopefully not be a major issue for this material.

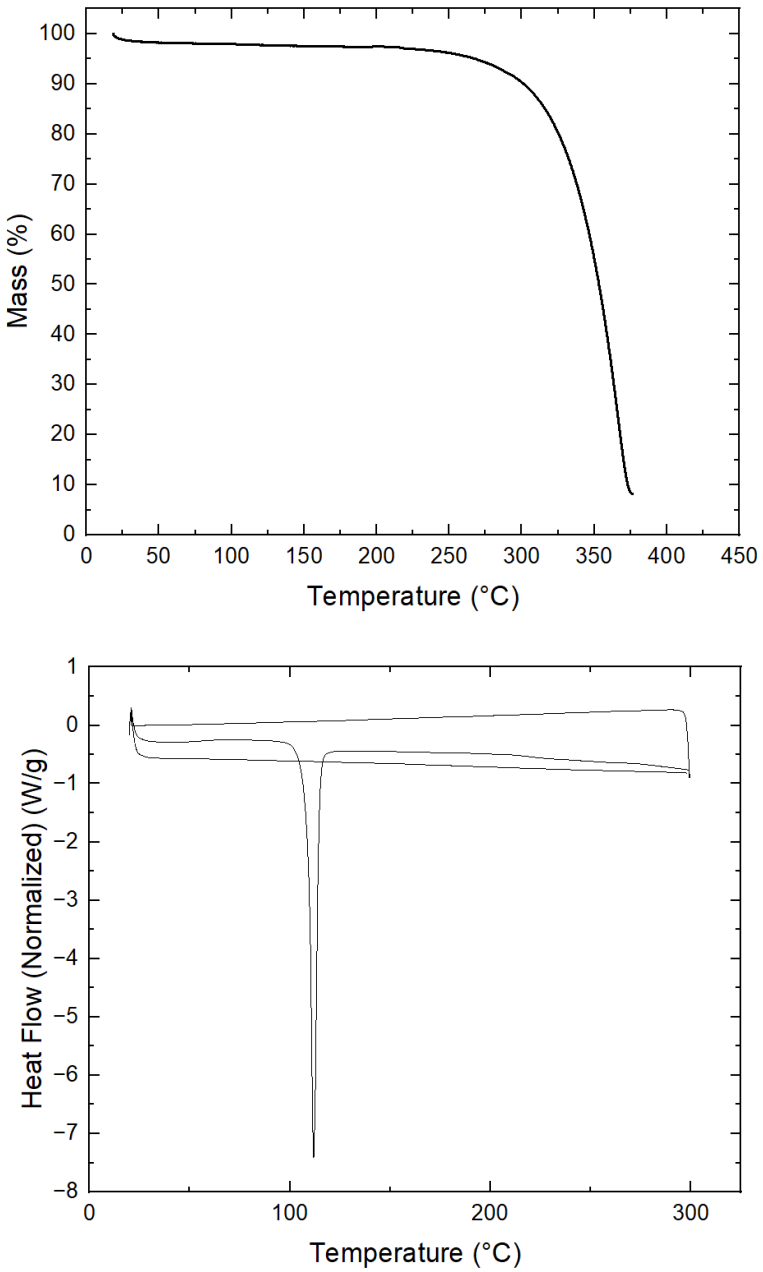

Figure 36: Graphs of the TGA (top) and DSC (bottom) for **PSA-027**

PSA-027 retained over 90% of its mass in temperatures up to 300˚C, as shown in its TGA, which shows that it would be structurally stable in a device. In the DSC (Figure 36), however, there is a spike at around 100˚C, but because it only appears in the first round of the DSC, it is unclear whether this is the materials T_g.

2.3. DFT modelling

Density functional theory (DFT) calculations were used to create models of the theoretical spread of the HOMO and the LUMO of the molecules, as well as confirming the approximate values of the HOMOs and the LUMOs determined experimentally. How the molecular orbitals are spread throughout the molecule give information regarding the physical properties of the compound[112].

PSA-013 electropolymerized as expected, but **PSA-025** did not. Upon further evaluation, it was observed that the LUMO of **PSA-025** was located within the moiety which would electropolymerize, while **PSA-013** did not. A hypothesis was made based upon observation correlating the location of the LUMO within a molecule and its feasibility to electropolymerize, which was then used to predict the electropolymerization of **PSA-027**. Upon further study, the cause of this phenomenon was observed to be due to the resonance structures of the molecules, as the resonance structures of **PSA-025** resulted in a very unstable oxidised intermediate, which could explain the lack of electropolymerization.

a)

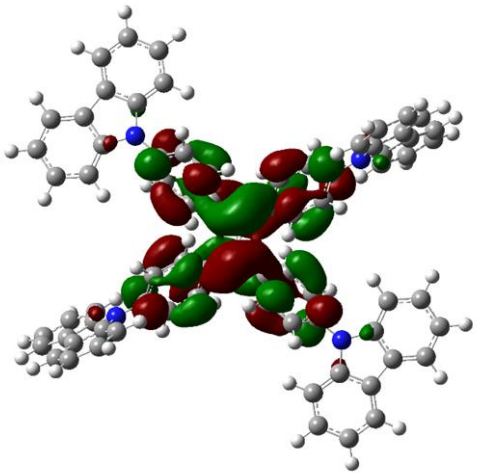

b)

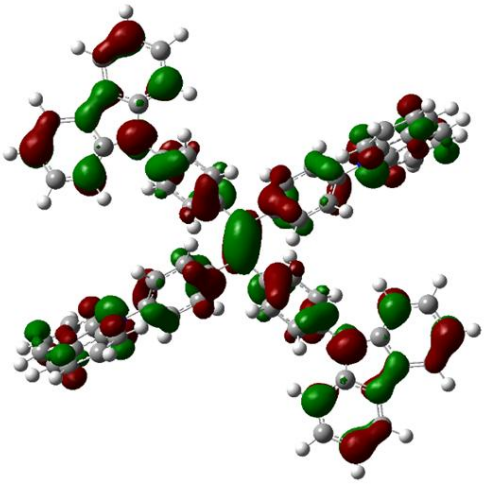

Figure 37: a) LUMO and b) HOMO of **PSA-013**

PSA-013's HOMO (Figure 37) is observed to be localised throughout the centre of the molecule, but it also spreads throughout the molecule. The HOMO and the LUMO levels for **PSA-013** are calculated to be -5.30 eV and -1.85 eV respectively, both compatible values with a perovskite's energy levels for good hole mobility and good electron blocking. The experimental value calculated in the electrochemical characterization section for HOMO and LUMO were -5.32 eV and -2.29 eV respectively, which are in accordance with the gas phase theoretical values provided by DFT. According to the hypothesis previously mentioned, as the LUMO is not placed in the carbazole moiety where electropolymerization is expected to occur, electropolymerization is likely successful, which is in accordance with the results published by Venkata Suresh Mothika *et al.*[93].

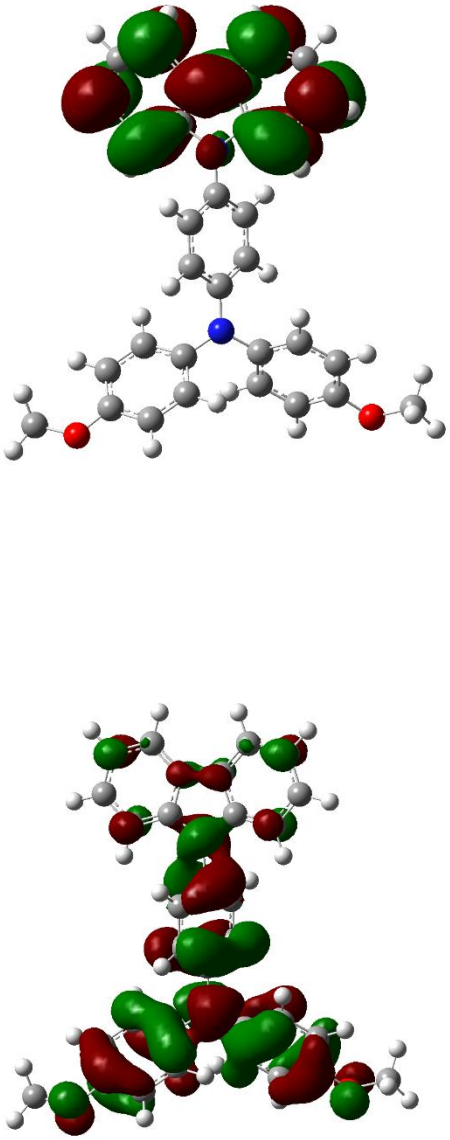

Figure 38: LUMO (top) and HOMO (bottom) for **PSA-025**

PSA-025's HOMO (Figure 38) is mostly located in the TPA and aryl moieties of the compound, while the LUMO is located exclusively in the carbazole moiety. Both energy levels are well-defined within specific areas of the molecule. The calculated values for the HOMO and the LUMO are -4.79 eV and -0.50 eV respectively. The theoretical HOMO confirms the experimentally calculated HOMO (-4.57 eV) but the theoretical value for the LUMO seems much lower than the experimentally observed (-1.24 eV). Nonetheless, the HOMO and both LUMOs are still complementary with a perovskite's energy levels. However, following the hypothesis previously mentioned, the LUMO is observed to be localised over the moiety where electropolymerization is expected to occur, and thus electropolymerization is not likely to be successful in this molecule.

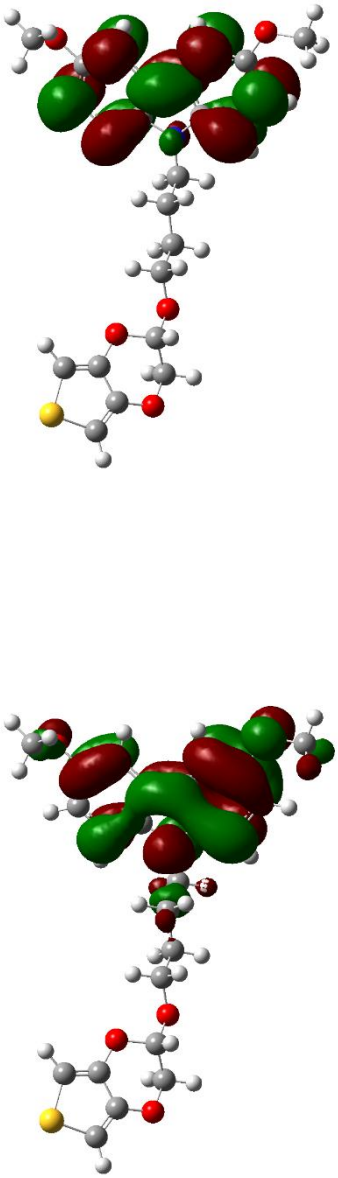

Figure 39: LUMO (top) and HOMO (bottom) for **PSA-027**

PSA-027's HOMO (Figure 39) is located on the same moiety as the LUMO: namely the dimethoxycarbazole unit. The theoretical values of the HOMO and the LUMO of **PSA-027** are -5.03 eV and -0.72 eV respectively. Both values are different than the ones calculated experimentally, with the experimental value of the HOMO being higher (-4.57 eV) and the experimental value of the LUMO being lower (-1.24 eV). Nonetheless, both the HOMOs and LUMOs are still complementary with a perovskite's energy levels. Following the hypothesis previously mentioned, as the LUMO is not located within the EDOT moiety of **PSA-027**, which is the expected electropolymerization area, the electropolymerization is likely to be successful.

2.4. Electropolymerization

2.4.1. The process

PSA-013, **PSA-025** and **PSA-027** were dissolved in DCM (1.0 x10^{-4} moldm^{-3}) and were used for the electropolymerization studies. A blank measurement (Figure 40) was carried out to confirm that DCM does not have any redox reaction within the potential window chosen for the electropolymerization of the compounds. CVs were run on ferrocene as this would be used for the internal reference for the electropolymerisation experiments.

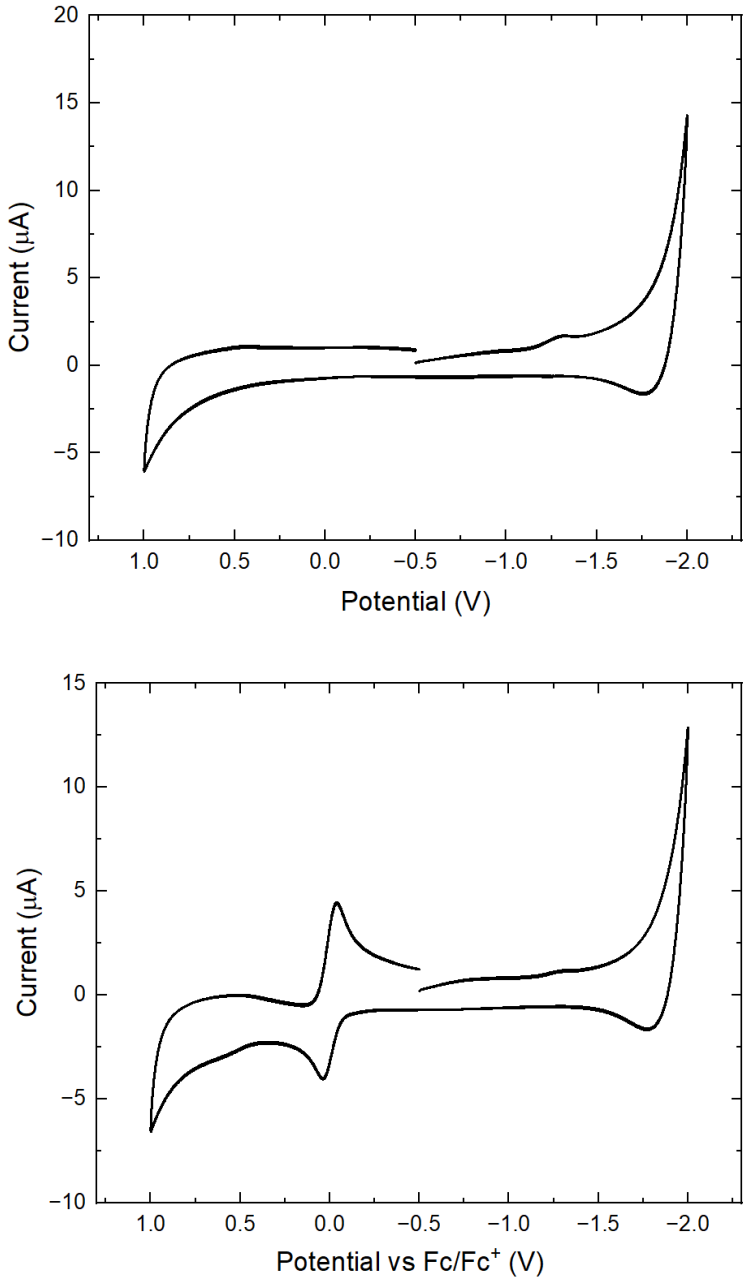

Figure 40: Blank CV measurement (top) and Fc/Fc^+ in blank CV measurement (bottom)

The first run of the CV was carried out to confirm the redox waves observed in the previously recorded CVs were in accordance with the ones observed before running the electropolymerization process. Furthermore, it also confirms the appropriate potential window for the electropolymerization onto ITO. Multiple scans were then run and the changes in the CVs were monitored. After the electropolymerization, the scan rates were plotted against the peak current to check for successful electropolymerization, which would produce a straight line with a positive gradient[8].

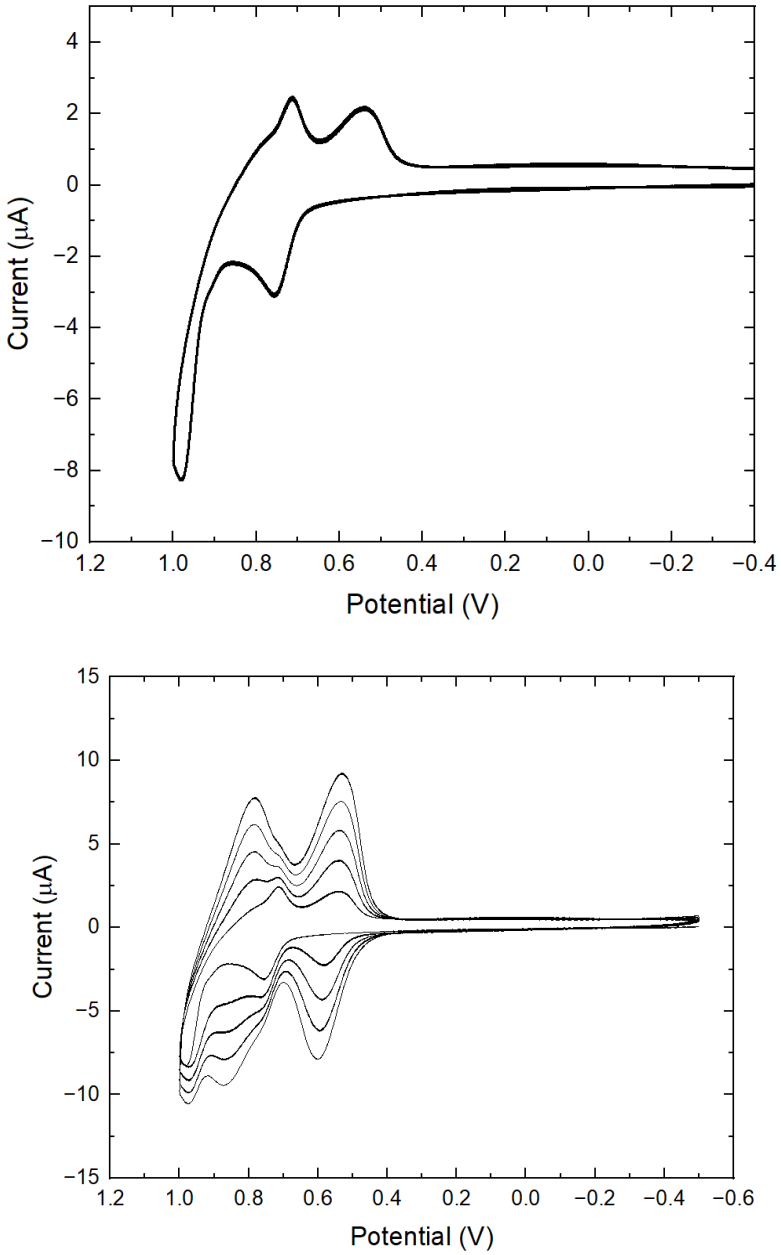

Figure 41: Single scan CV (top) and 5 scans CV (bottom) of **PSA-013**

The first CV single run of **PSA-013** (Figure 41) was identical to the one shown during the preliminary electrochemical characterization. As mentioned before, the two peaks

have been attributed to the oxidation of the carbazole units. During electropolymerization, the two sets of peaks in the cathodic and anodic waves increase symmetrically, which suggests that electropolymerization is successful. There is a slight change in the potential as the electropolymerization progresses showing that more conjugated oligomers are being produced. It is worth mentioning that a transparent film was observed in the platinum working electrode, which was caused by the deposition of the electropolymerized film.

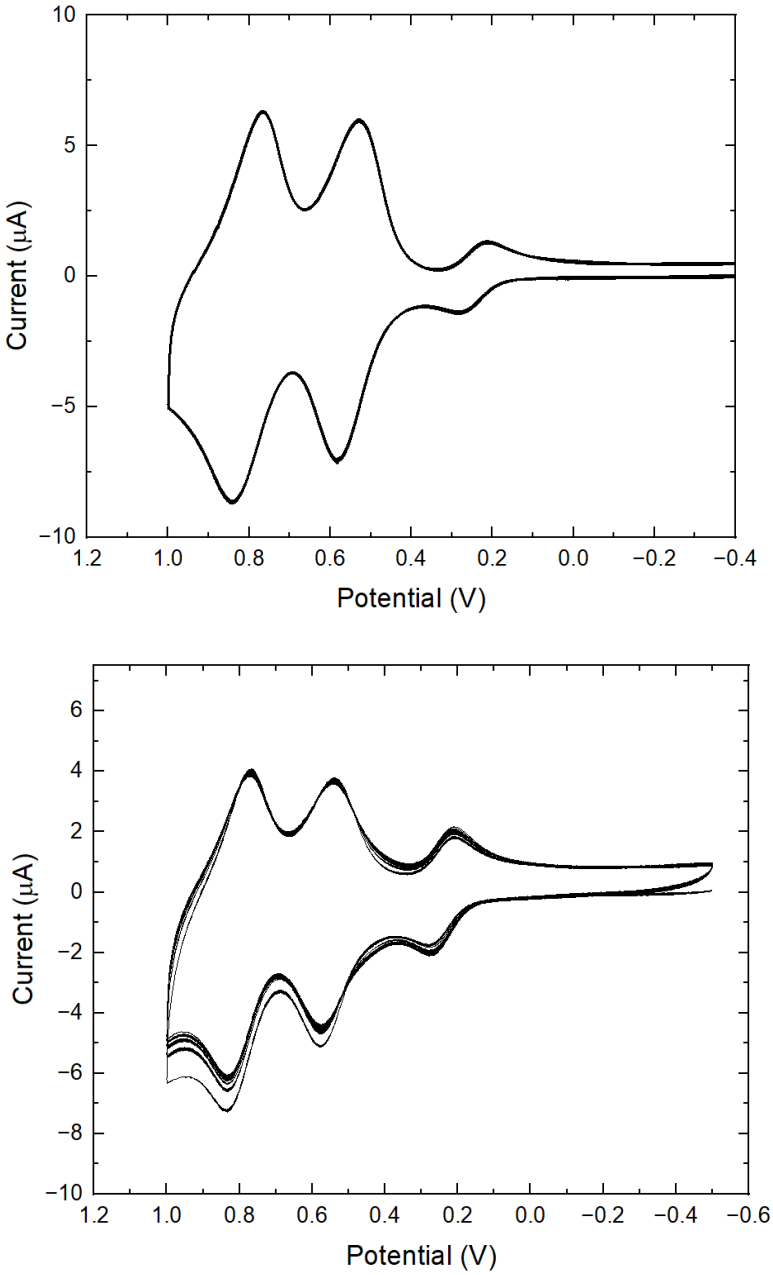

Figure 42: Single scan CV (top) and 5 scans CV (bottom) of **PSA-025**

The first scan of the CV of **PSA-025** (Figure 42) is identical as the one observed before. Upon repeated scans the peak currents do not increase significantly and there is no new

peak formed due to a more highly conjugated system indicating that electropolymerisation is not occurring in line with DFT predictions.

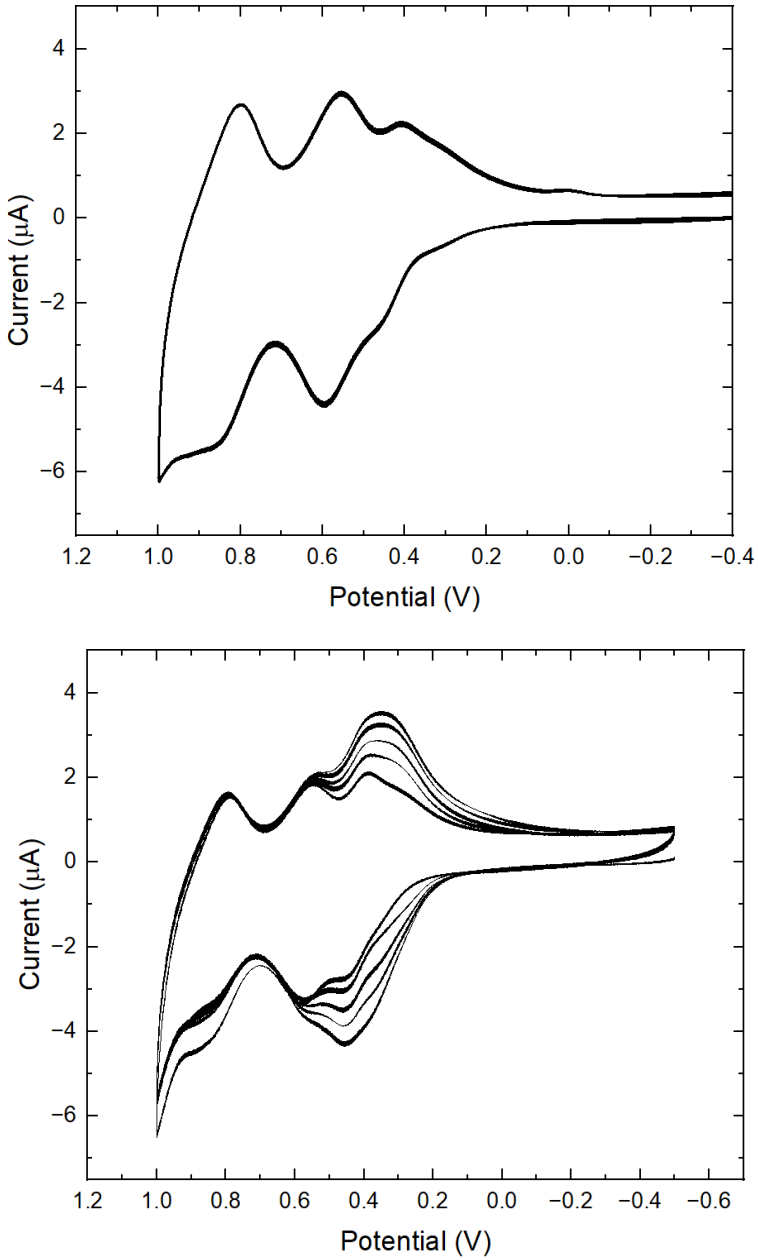

Figure 43: Single scan CV (top) and 5 scans CV (bottom) of **PSA-027**

PSA-027 was designed to have dimethoxy moieties connected to the 2- and the 7-positions of the carbazole moiety to avoid electropolymerization of this moiety, and as shown in the CV (Figure 43), the peaks which correspond to the dimethoxycarbazole stayed the same, while the peak corresponding to the EDOT moiety increased symmetrically both in the anodic and the cathodic wave. This demonstrated that the electropolymerization in **PSA-027** occurs in the EDOT moiety.

2.4.2. Scan rate vs peak current

For scan rate vs peak current plots, four different CV scans were undertaken: 25, 50, 75 and 100. For each number of scans, the working electrode was then placed within a clean solution of DCM and a CV was carried out with different scan rates. The peak current was then recorded and plotted. Generally, for the scan rate vs peak current to be considered successful, there should be a straight line with a positive gradient.

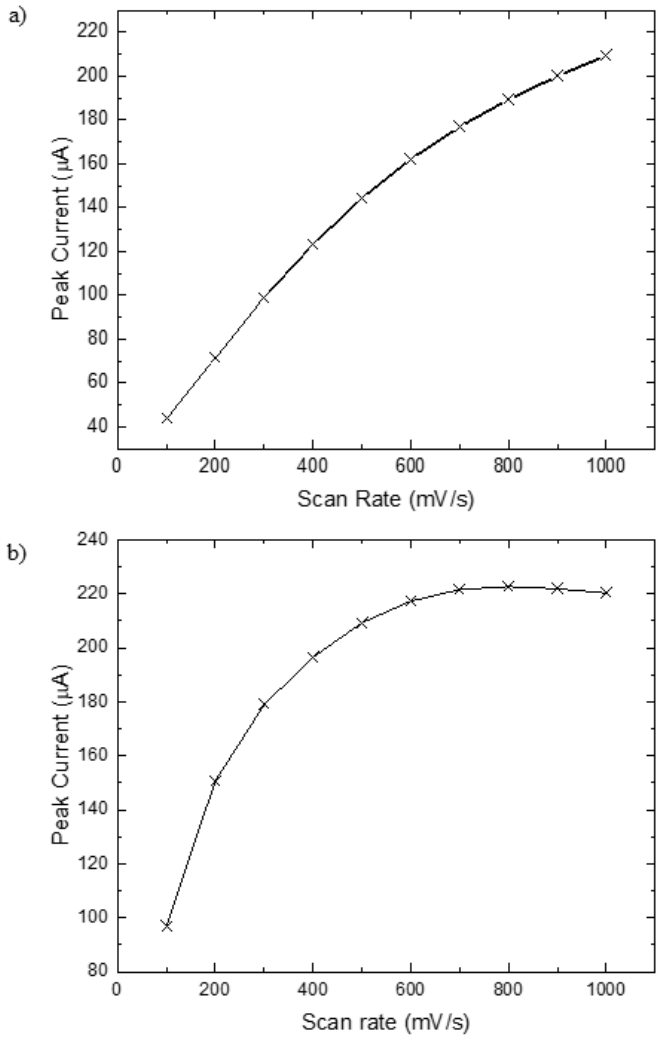

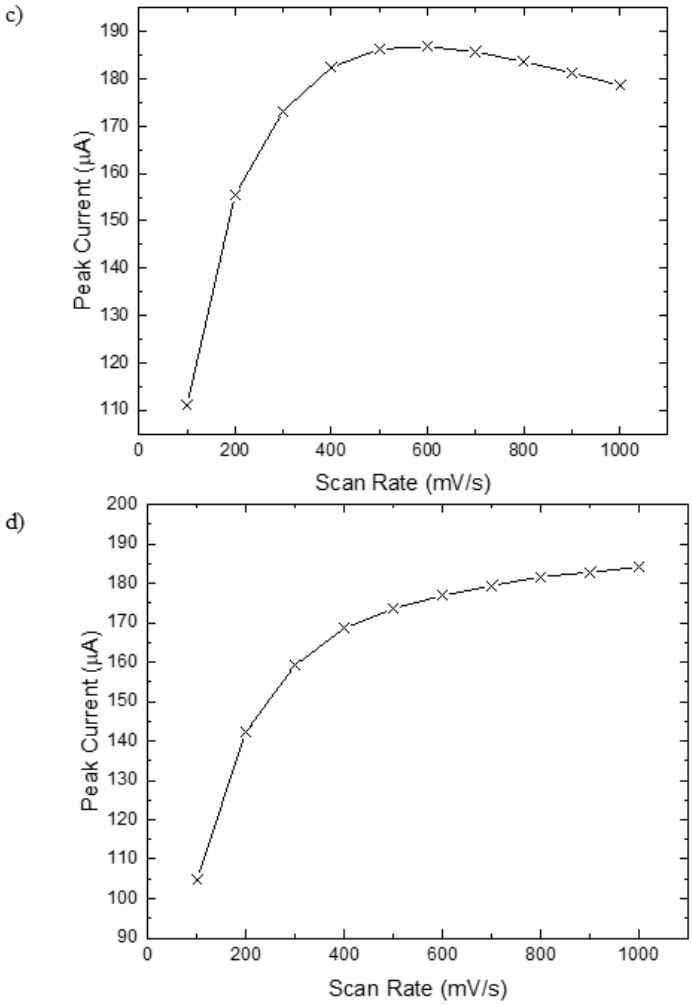

Figure 44: Scan rate vs peak current for a) 25, b) 50, c) 75 and d) 100 scans for **PSA-013**

For **PSA-013** (Figure 44), it can be readily seen that for lower scans (eg. 25 scans) the plot of the scan rate versus peak current is more linear than those observed with more scans. The data suggests for larger scans that either the electropolymerisation process has mixed kinetics (eg. diffusion and adsorption), the films are poorly surface confined or that for thicker films increased electrical resistance is occurring.

a)

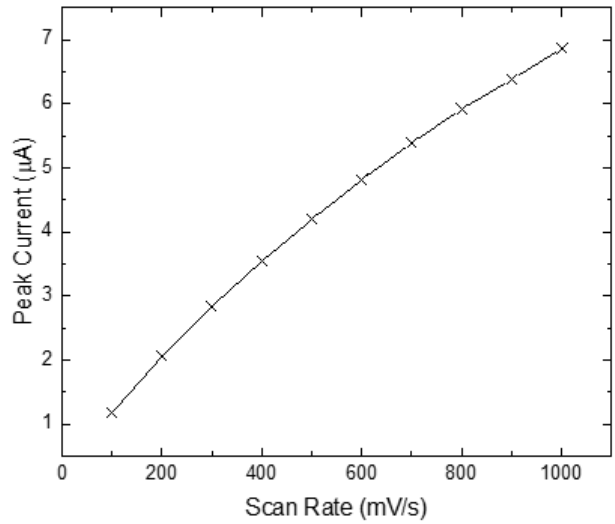
Peak Current (μA)
Scan Rate (mV/s)
1
2
3
4
5
6
7
0
200
400
600
800
1000

b)

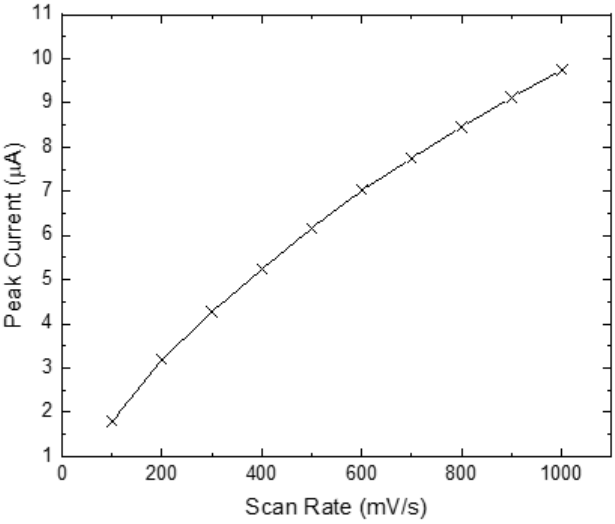
Peak Current (μA)
Scan Rate (mV/s)
1
2
3
4
5
6
7
8
9
10
11
0
200
400
600
800
1000

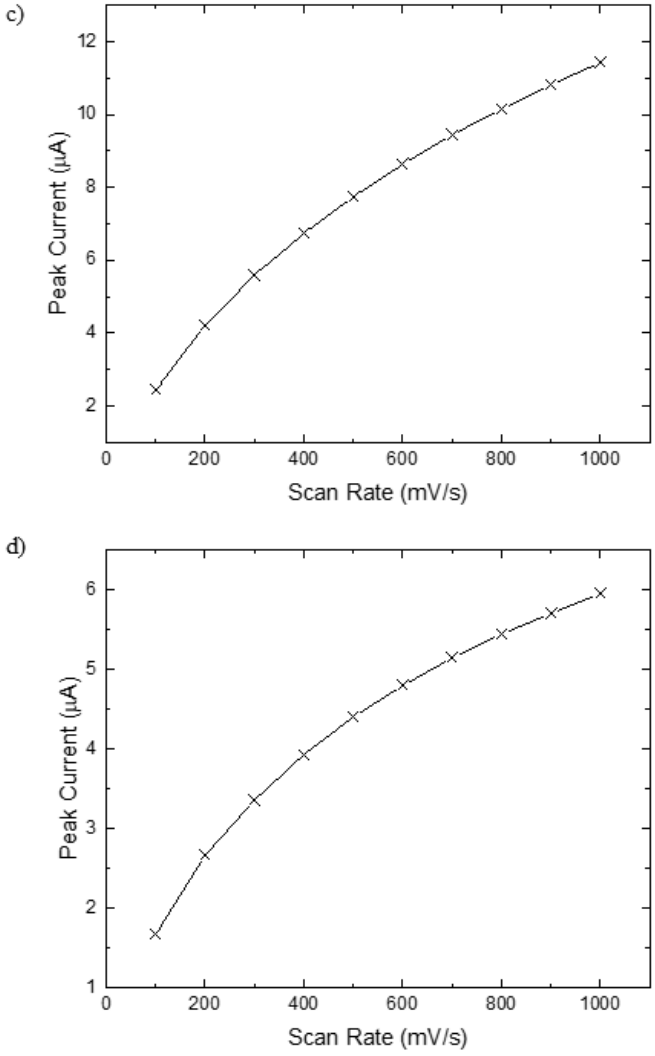

Figure 45: Scan rate vs peak current for a) 25, b) 50, c) 75 and d) 100 scans for **PSA-025**

For **PSA-025** (Figure 45), the plots of scan rate versus peak current were much more linear. However, there was no evidence from the electropolymerisation CVs that electropolymerisation was occurring. Due to time constraints, we therefore decided not to study this material further.

a)

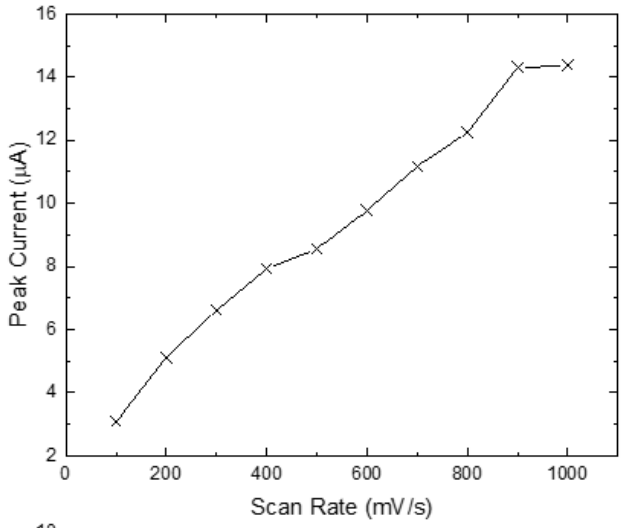
Peak Current (μA)
Scan Rate (mV/s)
2
4
6
8
10
12
14
16
0
200
400
600
800
1000

b)

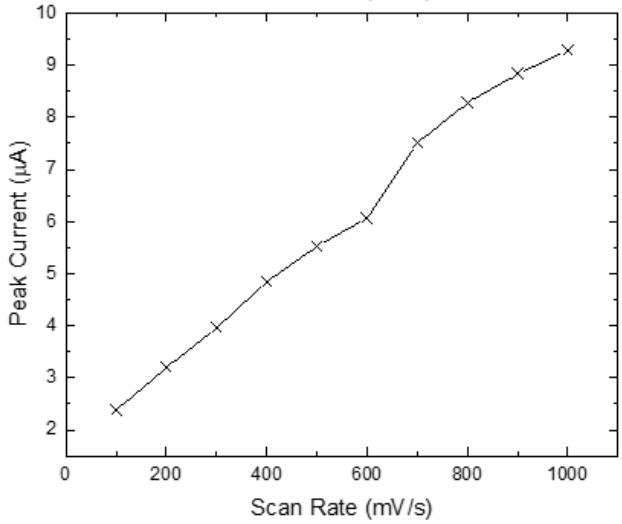
Peak Current (μA)
Scan Rate (mV/s)
2
3
4
5
6
7
8
9
10
0
200
400
600
800
1000

c)

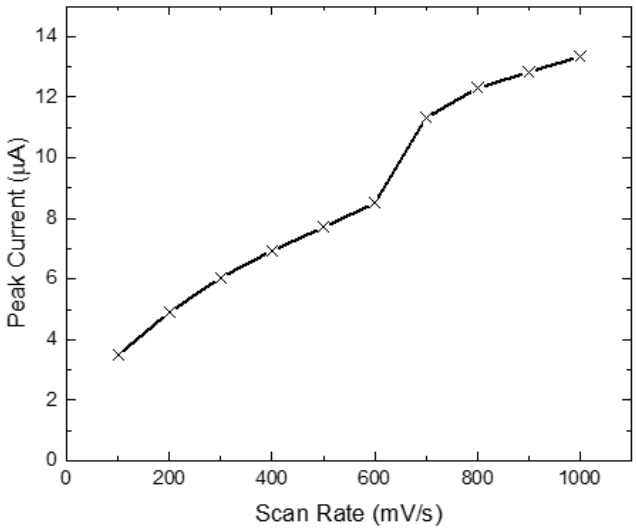
Peak Current (μA)
Scan Rate (mV/s)
0
2
4
6
8
10
12
14
0
200
400
600
800
1000

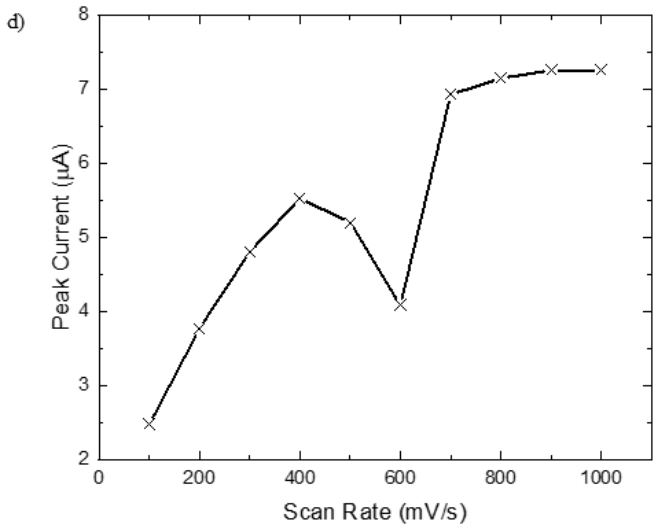

Figure 46: Scan rate vs peak current for a) 25, b) 50, c) 75 and d) 100 scans for **PSA-027**

For **PSA-027** (Figure 46), there was a general linear relationship between scan rate versus peak current suggesting some degree of surface confined behaviour. There were some noticeable anomalies observed for the 100 scans plot which were assumed to be caused by experimental error.

2.5. ITO electropolymerization and characterization

For the electropolymerization of the films in ITO glass plates, the set up used is the same as previously mentioned in the Introduction, with the ITO glass plates substituting the working electrode, and using a 150 ml beaker instead of the cell used for electropolymerization. The lid was made *via* a cardboard box to accommodate the larger cell (Figure 47).

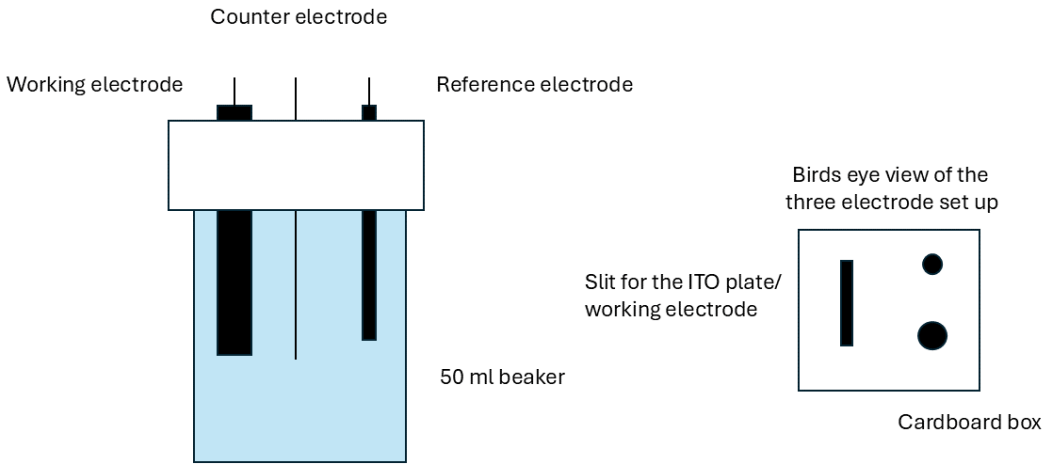

Figure 47: New set up for producing electropolymerized films

Two control runs were made, with the first one used to check the set up works as well as monitoring the electropolymerization of **PSA-013** into the ITO, and the second run to monitor the electropolymerization of **PSA-027** into ITO. These two runs were determined to be successful within the potential window selected, as observed below.

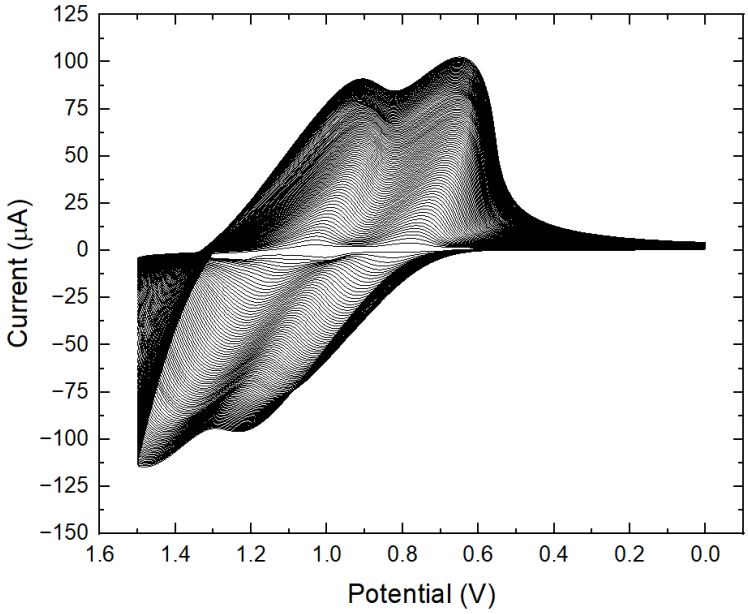

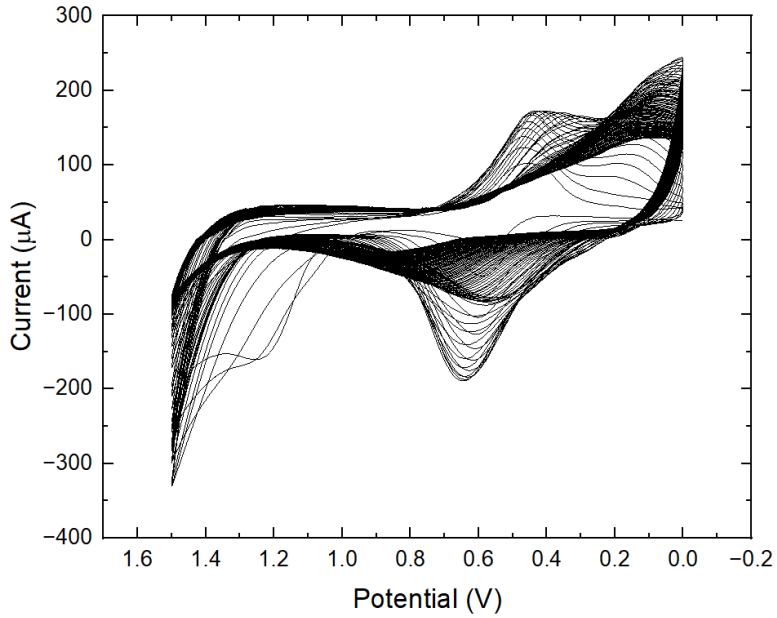

Figure 48: Test for electropolymerization in ITO for **PSA-013** (top) and for **PSA-027** (bottom)

These two ITO plates were used for characterization (Figure 48), and an extra 16 ITO plates were made, 8 for each molecule, for both thickness and conductivity testing, which will be discussed later in the Conductivity measurements section. The graphs for these scans can be observed in the General Methods section of the thesis. For the characterization of the ITO plates, FTIR and UV-vis were carried out.

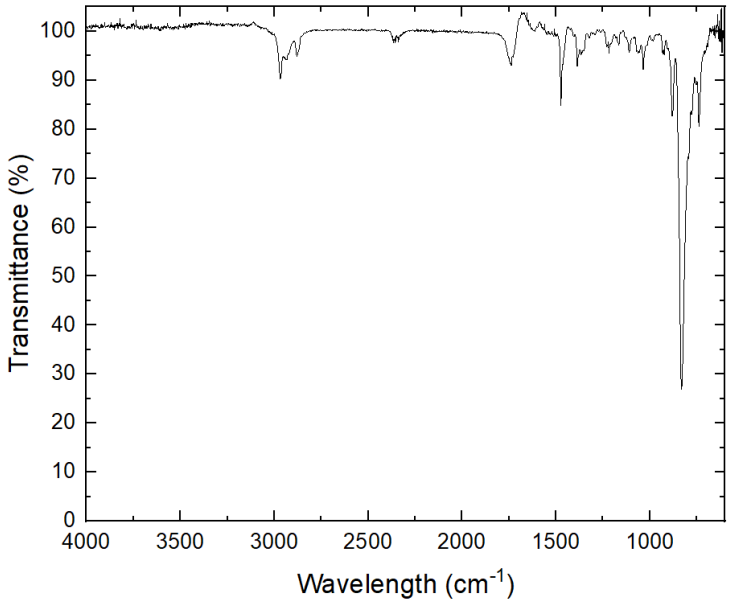

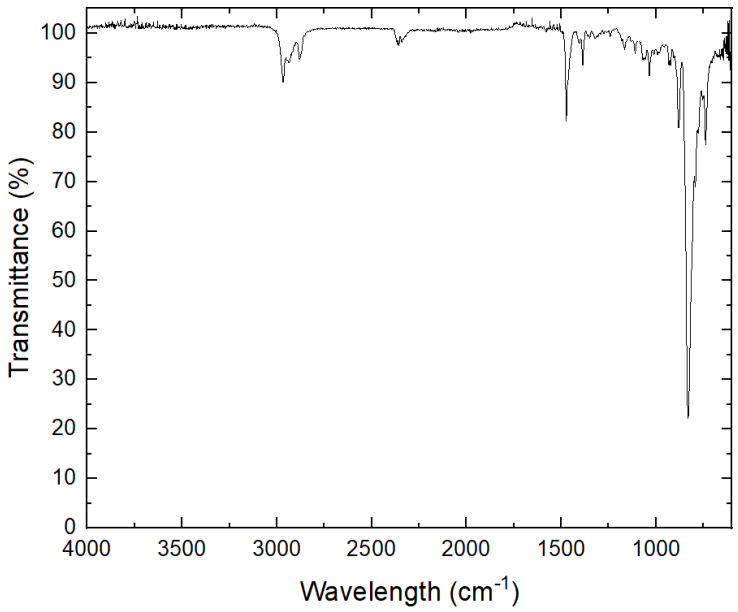

Figure 49: FTIR for electropolymerized **PSA-013** (top) and **PSA-027** (bottom)

For the FTIR (Figure 49), the polymer was scraped from the ITO and placed in the FTIR. The FTIR showed the expected post electropolymerization peaks, which was attributed to the formation of polymers. The carbazole moiety peaks remain (~3217 cm^{-1}, ~1484 cm^{-1} and ~750 cm^{-1}) in both FTIRs, and overall, the peaks are very similar. However, in the FTIR of **PSA-013** there is a large peak at ~1680 cm^{-1} corresponding to C = C, which is not as present with the FTIR for **PSA-027**, which was attributed to the larger conjugated system present in **PSA-013**. For **PSA-027**, the peak at ~750 cm^{-1} has diminished, which has been attributed to the C-H bond near the sulphur atom, which upon electropolymerization would disappear.

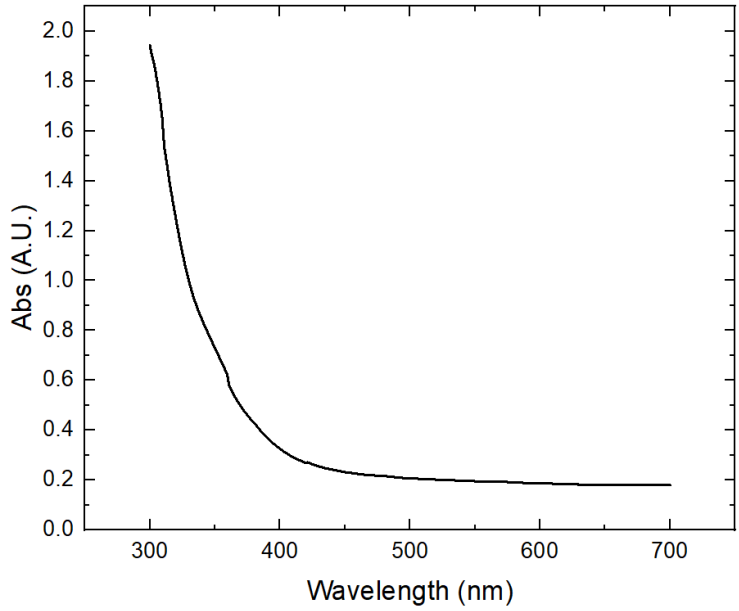

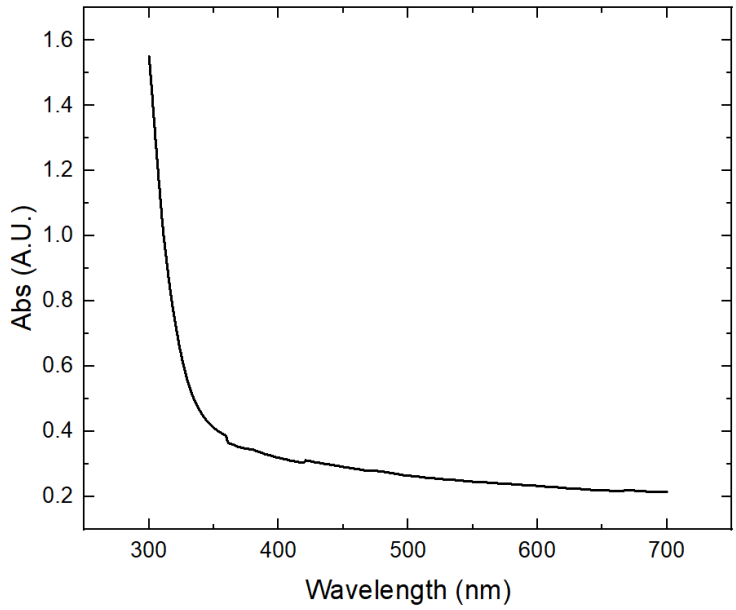

Figure 50: UV-vis for electropolymerized **PSA-013** (top) and **PSA-027** (bottom)

In UV-vis (Figure 50), the ITO plate with the polymers were directly placed within the spectrometer. In both spectra, the general pattern is the same. There are some low absorptions for both in the 350 – 430 nm region, and no distinct peak. As the blank measurement displayed no peaks whatsoever, the results displayed were attributed to the ITO plate doing most of the absorption.

2.6. Conductivity measurements

The ITO slides with electropolymerized films of **PSA-013** and **PSA-027** underwent thickness measurements and conductivity measurements using films deposited using 25, 50, 75 and 100 scans. AFM was used for the thickness measurements, as the thickness of the film is necessary for the conductivity measurements, as well as for calculating the surface roughness of the films, as usually smoother films tend to conduct electricity better due to a lower number of traps and defects. In all of the electropolymerized films on ITO, the lower part of the plate is much thicker than the top. This has been attributed to gravity, with an increase in size of the polymer resulting in an increase in material 'slumping' towards the bottom part of the plate. Because of this, the average thickness was taken.

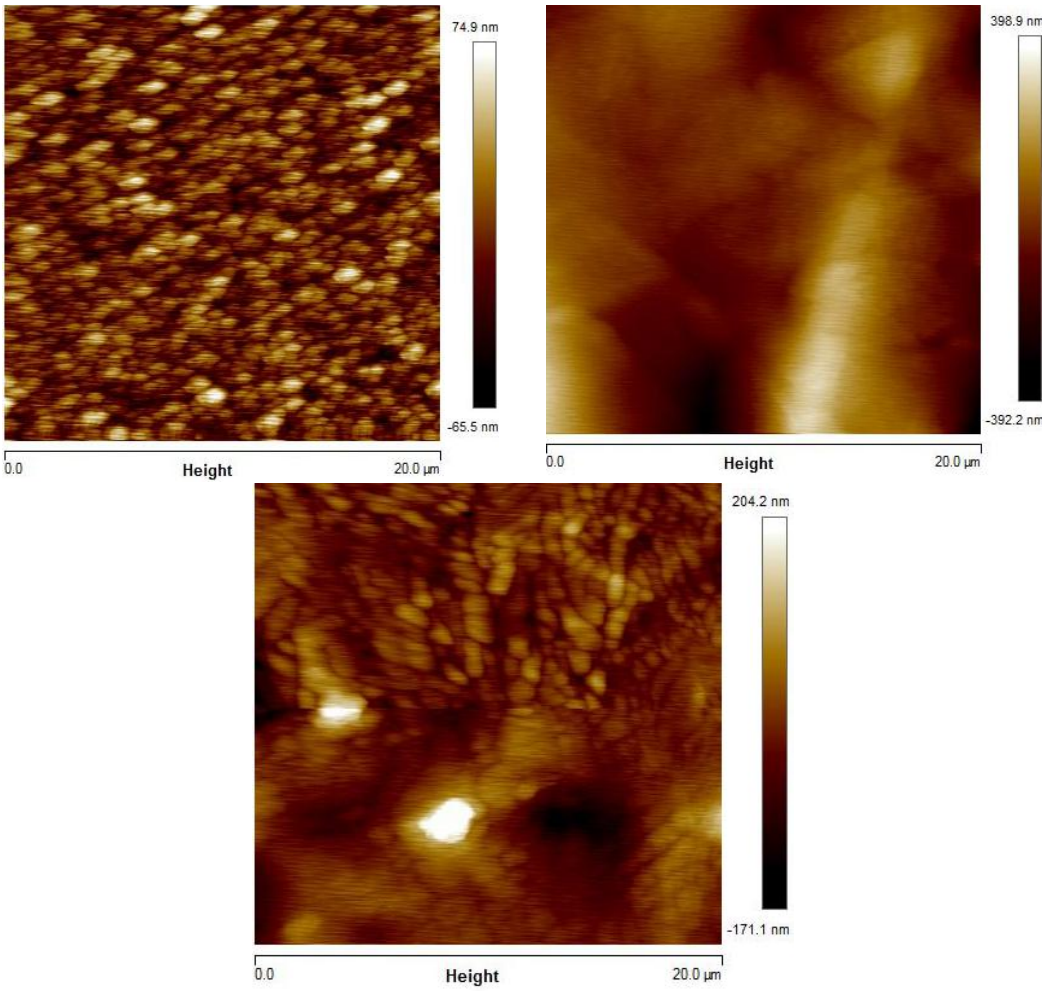

Figure 51: AFM images of a blank ITO (top left) and an ITO plate with 25 scans (top right) and 100 scans (bottom) of **PSA-013**

ITO had an average roughness (root mean square) of 19.4 nm, which is considered smooth. **PSA-013** had an average roughness of 90.7 nm with 25 scans, which decreased to 49.5 nm with 100 scans (Figure 51), while **PSA-027** had an average roughness of 32.9 nm, which increased slightly to 35.1 nm with 100 scans (Figure 52). The AFM

indicates that the conductivity of **PSA-027** may be higher than the conductivity of **PSA-013**, due to its lower roughness.

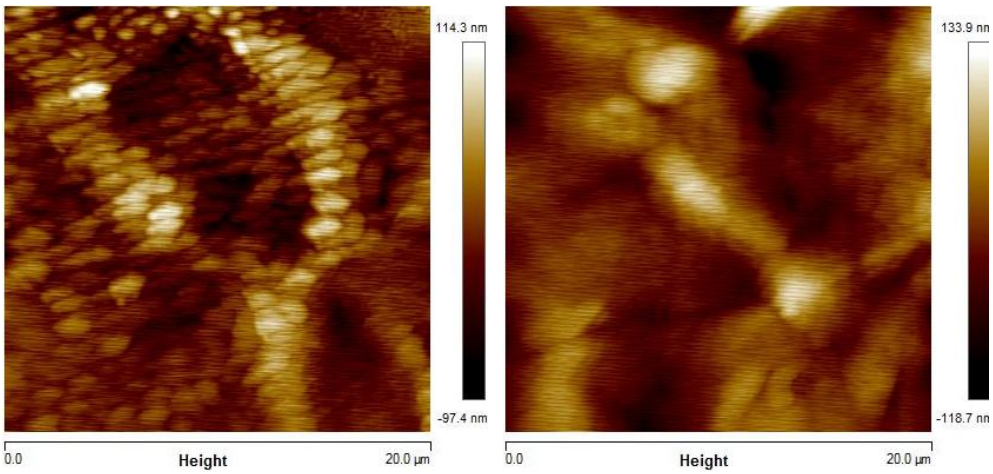

Figure 52: AFM images of an ITO plate with 25 scans (left) and 100 scans (right) of **PSA-027**

PSA-013 had an average thickness of 515 nm for 25 scans, 564 nm for 50 scans, 623 nm for 75 scans and 915 nm for 100 scans, while **PSA-027** had an average thickness of 623 nm for 25 scans, 867 nm for 50 scans, 885 nm for 75 scans and 938 nm for 100 scans. Throughout the different scan rates, the change in thickness is much larger in **PSA-013** than in **PSA-027**. This most likely arises due to the difference in how each molecule electropolymerizes, with the **PSA-013** polymer resembling a polymeric network, while **PSA-027** electropolymerizes linearly, layer by layer. For most HTM layers, a standard thin film has thickness below 100 nm. The films electropolymerized into ITO plates are very thick for a thin film, which could in principle increase the R_{series}.

For the intrinsic conductivity measurements, **PSA-013** falls from ~0.093 mS/cm to ~0.053 mS/cm for 25, 50 and 75 scans, but from 75 scans onwards the conductivity rises to ~0.065 mS/cm as seen in Figure 52. **PSA-027**, on the other hand, increases steadily from ~0.06 mS/cm for 25 scans, to ~0.15 mS/cm for 850 nm (a bit below 50 scans), and then fall to ~0.13 mS/cm (Figure 54).

The variance overall is much higher for **PSA-013** than for **PSA-027 (**Figure 53) and the highest current is much higher for **PSA-027** than for **PSA-013**, which means that **PSA-027** is much more reproducible and a better organic semiconductor than **PSA-013**. For reference, Spiro-OMeTAD has an intrinsic conductivity of ~0.128 mS/cm[113], making **PSA-027** a promising HTM.

	Average Thickness (nm)	Average Thickness (nm)
Number of scans	**PSA-013**	**PSA-027**
25	515	623
50	564	867
75	623	885
100	915	938

Table 3: Average thickness and number of scans for each molecule

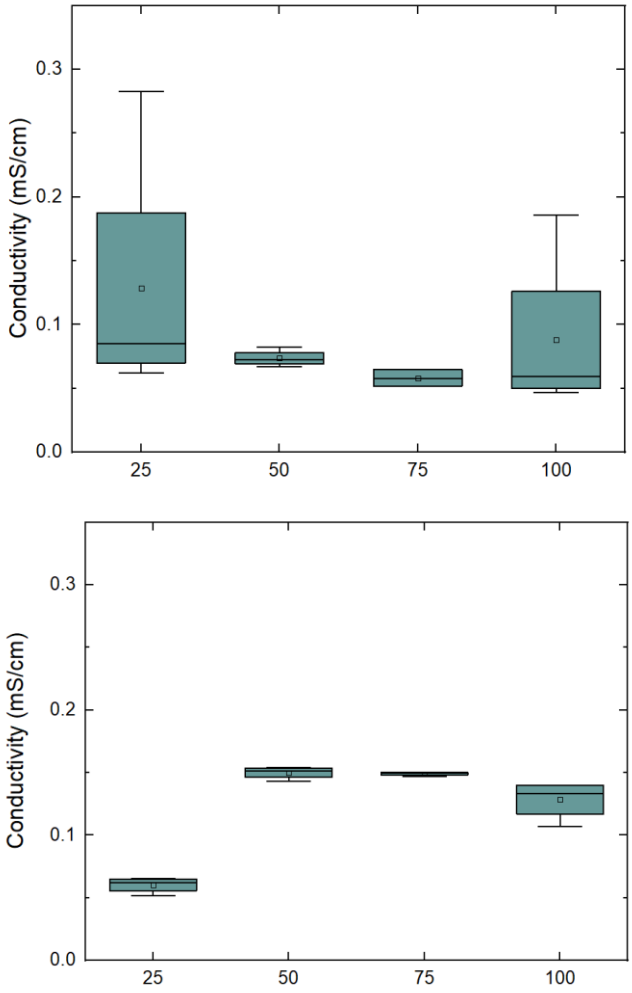

Figure 53: Standard deviation of the conductivity based on number of scan rates of **PSA-013** (top) and of **PSA-027** (bottom)

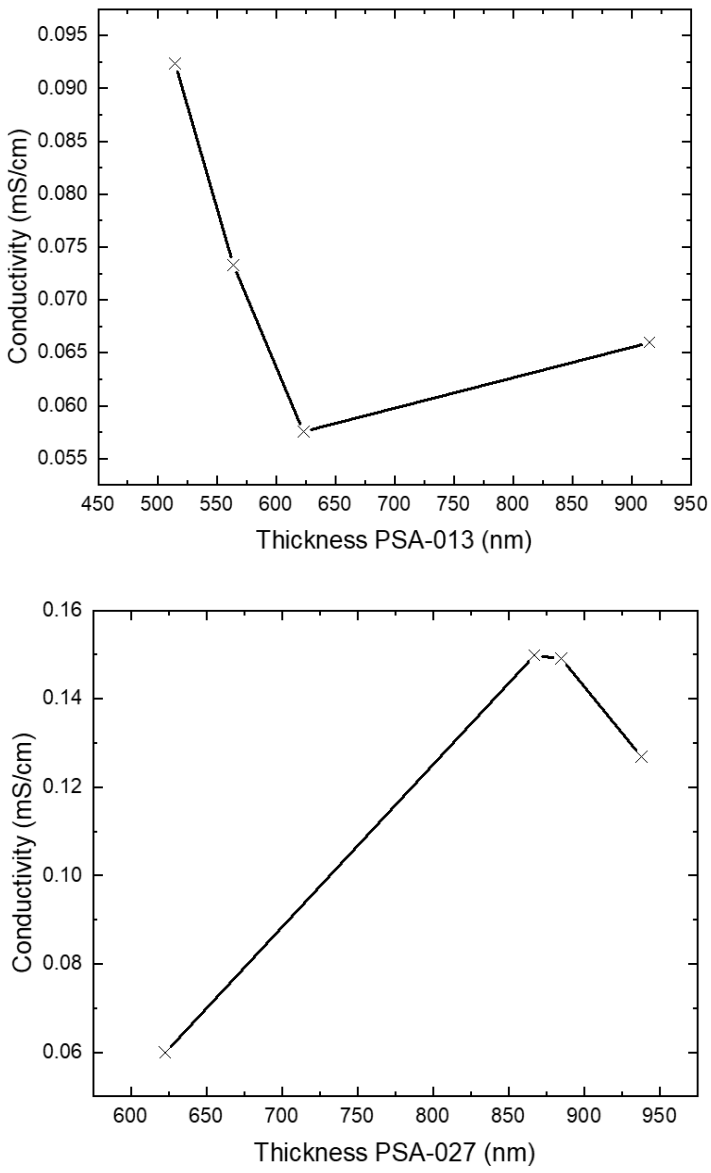

Figure 54: Conductivity vs Thickness plots of **PSA-013** (top) and **PSA-027** (bottom)

2.7. Conclusion and future work

In conclusion, three possible electropolymerisable HTMs have been synthesised (**PSA-013**, **PSA-025** and **PSA-027**). The optoelectronic properties of these molecules have been investigated by UV-vis and fluorescence spectroscopy and their redox properties have been investigated using cyclic and square wave voltammetry. DFT modelling proved useful in predicting their HOMO and LUMO energies as well as giving insight into whether the materials will electropolymerize.

Electropolymerisation studies conducted on the materials gave mixed results with **PSA-013** and **PSA-027** showing evidence of electropolymerisation, whereas **PSA-025** was discarded from this study due to its apparent inability to electropolymerize. **PSA-013** and **PSA-027** were electropolymerized onto ITO glass and their film thickness and intrinsic conductivities were determined. **PSA-027** demonstrated the highest intrinsic conductivity, surpassing that of Spiro-OMeTAD, suggesting its potential future use as a HTM.

Future work could look at investigating improving the electropolymerisation of **PSA-027** in terms of film uniformity and quality in efforts to improve the conductivity of the films. Furthermore, like Spiro-OMeTAD, it appears necessary to dope **PSA-027** if highly conducting films are to be produced. Finally, the carbazole head group of **PSA-027** could be replaced by another redox active unit such as triphenylamine in efforts to improve both morphology and conductivity of the films.

3. Experimental

3.1 Computational details

Fluorochem® and BLD Pharmatech Ltd. supplied all starting reactants and reagents found within this thesis, and the dry solvents used were either purchased from Merck® or collected from the Pure Solv 500 MD™ solvent purification system. TLC was carried out with Merck® silica gel (6A) covered aluminium plates F254, and for column chromatography 60A silica gel from Fluorochem® was used.

Both ^{1}H NMR and ^{13}C NMR were carried out in a Bruker A VIII400 MHz spectrometer, and the solvents used were either deuterated acetone or deuterated chloroform, depending on solubility of the compound.

UV-vis spectra were collected using a Shimadzu UV-3600 UV-Vis-NIR spectrophotometer, and fluorescent spectra with a Shimadzu RF-5301PC spectrofluorometer. For UV-vis, solutions in DCM of $1x10^{-4}$ mol/dm^3 were used and for fluorescence measurements $1x10^{-5}$ mol/dm^3 solutions were used. The cuvettes were cleaned with DCM (the solvent used for these studies). For the electropolymerized films, the ITO plates with the samples were attached to the spectrometer and the spectroscopy was then carried out.

For FTIR analysis, a Jasco FR/IR 4100 was used. A small, solid sample was used for each compound. For the electropolymers, the ITO plates were scratched with a spatula into the surface in which the analysis will be conducted after proper cleaning with methanol.

TGA was carried out with a NETZSCH TG 209 F3 Tarsus® and DSC was collected in a NETZSCH-Geratebau gmbh DSC 214 Polyma.

Electrochemistry and electropolymerization studies were carried out using a CH Instrument Electrochemical Workstation (CHI 440a). All solutions used recorded in DCM ($1x10^{-5}$ mol/dm^3). Tetra-n-butylammonium pentafluoride (0.1 M) was used as the electrolyte.

For conductivity studies and thickness, a Bruker Innova (Tapping mode) and a Lucalab Pro 4 were used respectively. In both cases, the ITO plates were used as substrate.

An Agilent 6546 Q-TOF-MS High Resolution Accurate Mass spectrometer was used to obtain mass spectra.

DFT calculations were performed using Gaussian 16 and the structures were inputted and visualised using GaussView.

3.2 Synthesis

For all reactions undertaken the solutions were degassed and all glassware (round bottom flasks, condensers, stirrers, and double-necked round bottom flasks) were placed in an oven at 180˚C for ~2 hours prior to use. All reactions were carried out under a N_2 environment. For oxygen sensitive reactions, the degassing step may occur after the first compound was added, followed by N_2 addition. The reactions were checked with TLC for completeness, usually under a solution of 2:8 Ethyl acetate: Petroleum ether unless otherwise mentioned.

Synthesis of PSA-006[94]

Compound (**1**) (800 mg/ 2.53 mmol (20 equiv.)) was added to chloroform (15.0 ml) at 0˚C, followed by $FeBr_3$ (20.0 mg/ 0.13 mmol (1.0 equiv.)) and Br_2 (1.00 ml/ 10.3 mmol (80 equiv.)). The mixture was then warmed to room temperature under stirring for 3 hours. The solution was then poured into water and DCM. Afterwards, $Na_2S_2O_4$ was added until the red colour of the bromine disappears. The DCM layer was separated from the aqueous layer, dried with $MgSO_4$, and then filtered and concentrated under reduced pressure, affording 1.47 g of the target product. Yield = 98.0 %. ^{1}H NMR δ: 7.68 (d, J = 4.0 Hz, 1H, ArH), 7.53 (dd, J_1 = 8.4 Hz J_2 = 2.0 Hz, 1H, ArH), 6.82 (d, J = 2.0 Hz, 1H, ArH).

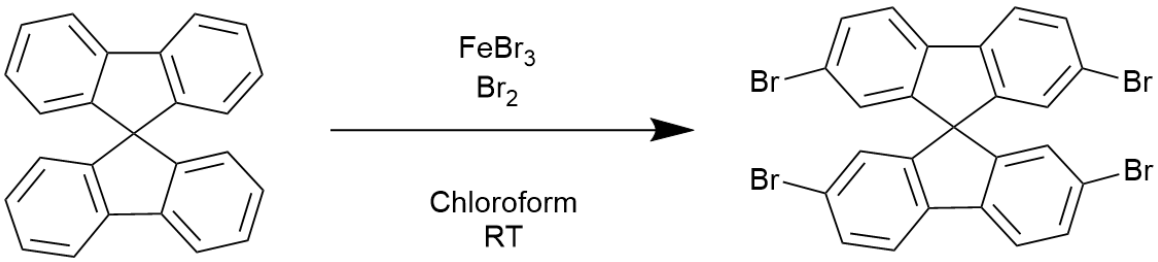

Attempted synthesis of PSA-007[94]

PSA-006 (500 mg/ 0.79 mmol (1.0 equiv.)) was added to o-dichlorobenzene (12.0 ml), followed by CuI (60.0 mg/ 0.31 mmol (0.4 equiv.)), carbazole (657 mg/ 3.93 mmol (5.0 equiv.)), K_2CO_3 (652 mg/ 4.72 mmol (6.0 equiv.)) and 2,2'-bipyridine (50.0 mg/ 0.31 mmol (0.4 equiv.)). The reaction mixture was then heated to 150˚C for two days. The temperature was increased to 175˚C and left overnight. The reaction was then poured into water, washed with DCM, dried with $MgSO_4$, filtered and concentrated under reduced pressure. Column chromatography (1:9 DCM: Petroleum Ether) was used to obtain a product, however the ^{1}H NMR was not consistent with the proposed structure of the desired product. ^{1}H NMR δ: 8.08 (d, J = 7.2 Hz, 2H, ArH), 7.43 (qd, J_1 = 8.0 Hz J_2 = 2.0 Hz, 3H, ArH), 7.24 (qd, J_1 = 8.0 Hz J_2 = 2.0 Hz, 2H, ArH).

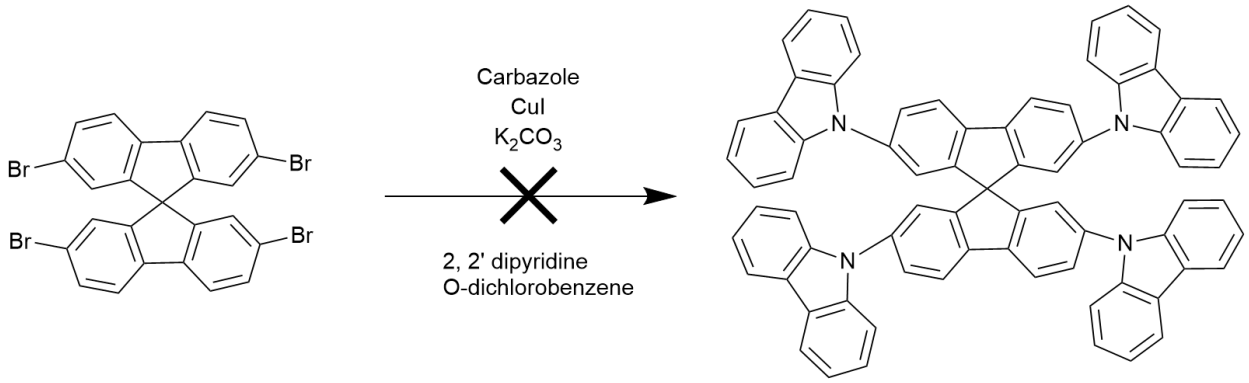

Attempted synthesis of PSA-009[89]

PSA-006 (203 mg/ 0.32 mmol (1.0 equiv.)), compound **2** (580 mg/ 1.58 mmol (5.0 equiv.)), K_2CO_3 (436 mg/ 3.16 mmol (10 equiv.)), $Pd(PPh_3)_4$ (38.0 mg/ 0.03 mmol (0.1 equiv.)), THF (22.0 ml) and distilled water (5.0 ml) were added and heated at 80°C overnight (>12 h). The reaction was then poured into water and washed with DCM, separated, dried with $MgSO_4$, filtered and concentrated under reduced pressure. ^1H NMR showed that it was mostly starting material.

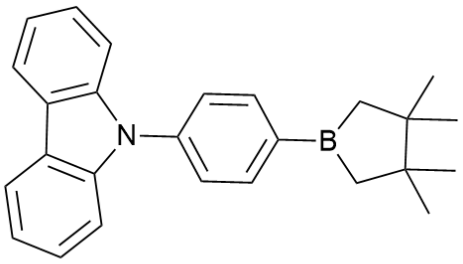

Compound 2

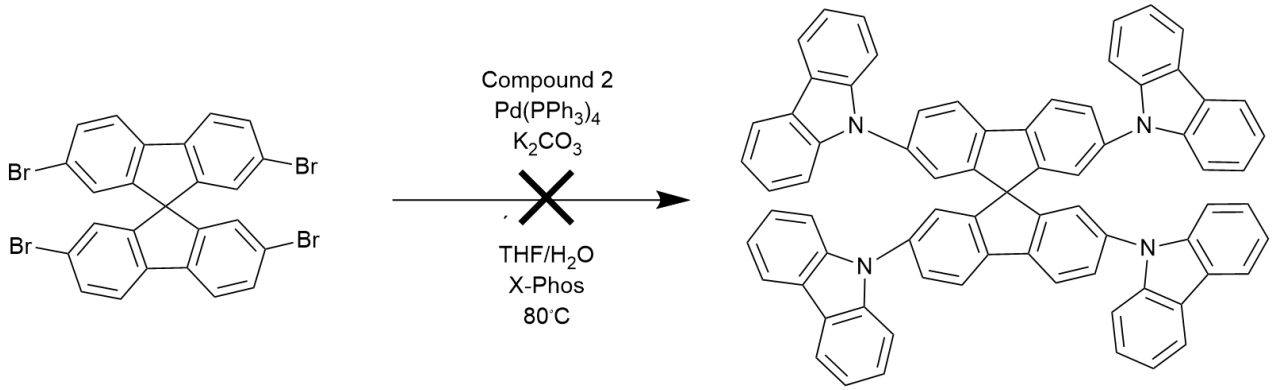

Attempted synthesis of PSA-011[77]

Carbazole (238 mg/ 1.42 mmol (4.5 equiv.)), K_2CO_3 (197 mg/ 1.42 mmol (4.5 equiv.)), CuI (3.00 mg/ 0.02 mmol (0.05 equiv.)), 18-crown-6 (1.40 mg/ 0.01 mmol (0.02 equiv.)) were added to DMA (20.0 ml) and stirred overnight at 165˚C. This solution turned from white to red. **PSA-006** (200 mg/ 0.32 mmol (1.0 equiv.)) was then added to DMA (3.00 ml), and this solution added to the mixture with the rest of the reactants and left to react for 24 h at 170˚C. The reaction was then left overnight at 185˚C. Afterwards, the reaction was quenched with water and filtered. TLC (2:8 ethyl acetate:petroleum ether) showed promising results, but ^{1}H NMR was not consistent with the structure of the target material.

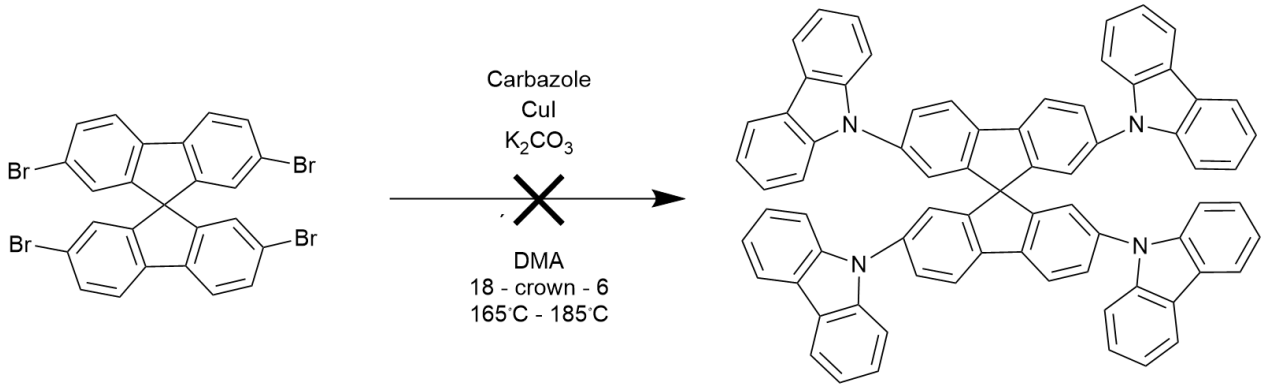

Synthesis of PSA-012[93]

Tert-Bu OK (1.64 mg/ 14.6 mmol (3.0 equiv.)) and carbazole (2.04 mg/ 12.2 mmol (2.5 equiv.)) were added to DMF (anhydrous) (16.0 ml), and then left at 70˚C for 10 min. After that, bis(4 – fluorophenyl)methanone (1.06 g/ 4.88 mmol (1.0 equiv.)) was dissolved in DMF (9.00 ml) and added to the previous solution. The reaction mixture was then heated at 70˚C for ~5 min and then left over 12 h under stirring. This mixture adopted bright orange-like colour, and while drying, it turned yellow-like on the TLC. It was then poured into ice water, filtered and recrystallised from acetone to produce 1.11 g of the yellow target compound. Yield = 44.4%. ^{1}H NMR δ: 8.18 (m, 2H, ArH), 7.81 (d, J = 8.0 Hz, 1H, ArH), 7.57 (d, J = 8.0 Hz, 1H, ArH), 7.47 (td, J_1 = 10.0 Hz J_2 = 2 Hz, 1H, ArH), 7.35 (td, J_1 = 8.0 Hz J_2 = 1 Hz, 1H, ArH).

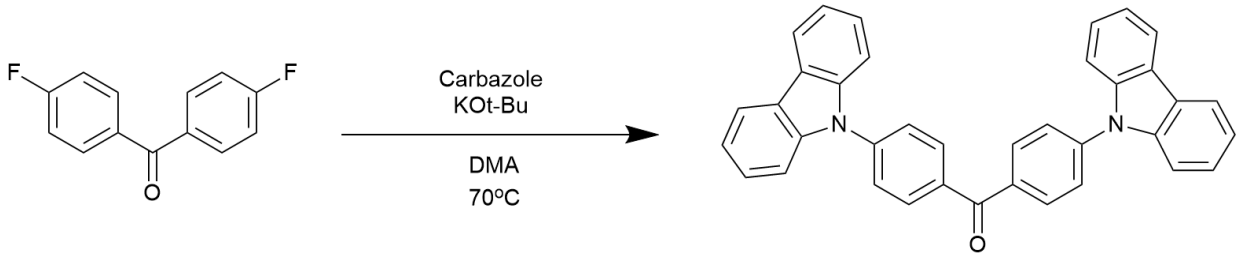

Synthesis of PSA-013[93]

PSA-012 (1.11 g/ 2.17 mmol (2.0 equiv.)) and cooled to -78˚C in a dry ice – acetone bath. After 20 min under stirring, $TiCl_4$ (0.30 ml/ 2.74 mmol (2.5 equiv.)) was added, and left for 20 more minutes. Afterwards, the reaction was left to warm to room temperature and heated at 70˚C for >12 h. The reaction was then poured into water and washed with DCM and brine. The organic phase was then dried with $MgSO_4$, filtered and concentrated under reduced pressure. Trituration was then carried out (MeOH and DCM), filtered, and left on a vacuum oven (50˚C) overnight to yield the product (350 mg). Yield = 33.0%. Melting point: >300˚ C. ν_{max} (cm^{-1}): 3217 (C-$H_{carbazole}$), 1629 (C=C), 1554 (C=C_{phenyl}), 1487 (C=$C_{carbazole}$), 1383 (C-N), 750 (C-H). ^{1}H NMR δ: 8.16 (d, J = 8.0 Hz, 1H, ArH), 7.54 (s, 2H, ArH), 7.45 (d, J = 8.0 Hz, 1H, ArH), 7.36 (td, J_1 = 10.0 Hz J_2 = 0.8 Hz, 1H, ArH), 7.3 (td, J_1 = 8.0 Hz J_2 = 0.7 Hz, 1H, ArH). ^{13}C NMR δ: 141, 133, 127, 126, 124, 121, 110. Mass Spectroscopy (ESI^+) m/z: 993.3966. Elemental Analysis: C (89.17%), H (4.44%), N (4.95%) (Expected: C (89.52%), H (4.84%), N (5.65%)).

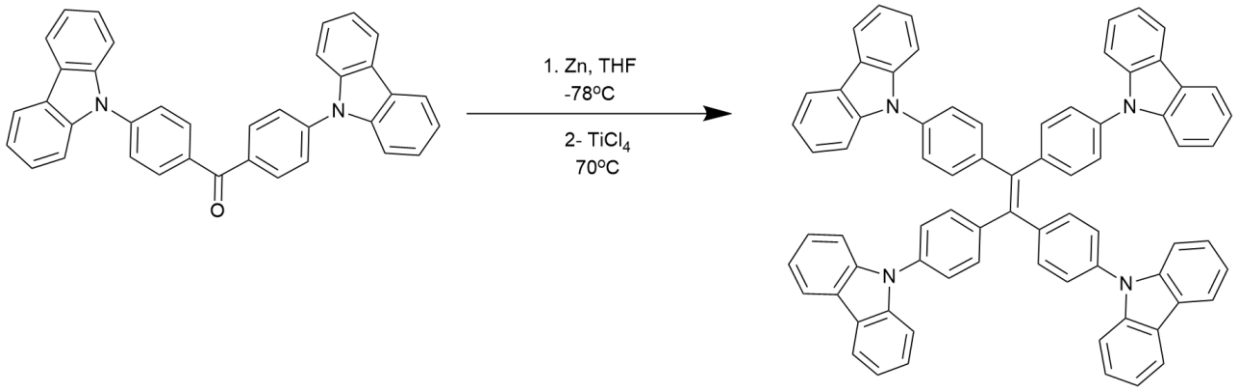

Synthesis of PSA-014[45, 46]

This reaction follows the same procedure as **PSA-023**, with the same ratios, but different quantities.

Carbazole (2.00 g/ 12.0 mmol (1.0 equiv.)), 4-fluoronitrobenze (1.69 g/ 12.0 mmol (1.0 equiv.)) and K_2CO_3 (3.30 g/ 24.0 mmol (2.0 equiv.)) were added to DMF (15.0 ml), left at room temperature for 20 min and then placed at 70˚C under stirring for >24 h. The reaction was poured into ice water, filtered, washed with water and left at a vacuum oven to dry (50˚C). Some carbazole was observed within the filtrate, but a methanol wash up was enough to dissolve this impurity, leaving with 3.00 g of the target product being collected without any need of further purification. Yield = 78.0%. ^{1}H NMR δ: 8.57 (d, J = 8.0 Hz, 1H, ArH), 8.25 (d, J = 8.0 Hz, 1H, ArH), 8.01 (d, J = 12.0 Hz, 1H, ArH), 7.60 (d, J = 8.0 Hz, 1H, ArH), 7.49 (td, J_1 = 10.0 Hz J_2 = 0.8 Hz, 1H, ArH), 7.36 (t, J = 8.0 Hz, 1H, ArH).

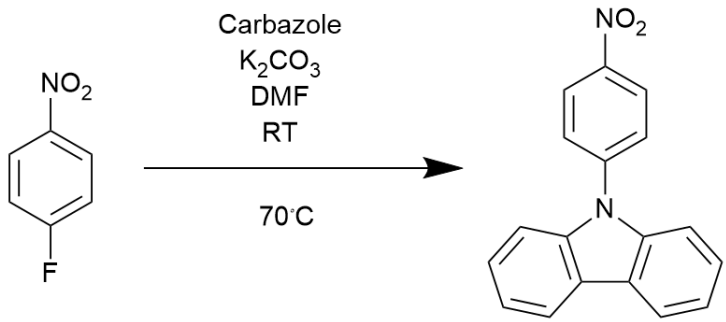

Synthesis of PSA-015[43, 46]

This reaction follows the same procedure as **PSA-017** and **PSA-024**, with same proportions, but different amounts. The only major change is that for **PSA-017** and **PSA-024** the solution after completion was directly used on the following reactions.

PSA-014 (2.00 g/ 6.94 mmol (1.0 equiv.)) and Pd/C (60% coverage) (103 mg/ 0.97 mmol (0.1 equiv.)) were added to ethanol (200 ml) and heated to 83°C. Once at that temperature, hydrazine monohydrate was added drop wise (2.00 ml/ 41.6 mmol (6.0 equiv.)) and the reaction was left to react overnight (>2 h). The reaction was then filtered over a celite pad while hot and washed with DCM once it cooled. The combined washings were concentrated under reduced pressure, resulting in an oil which was used in the next step without any further purification. ^{1}H NMR δ: 8.10 (d, J = 10.0 Hz, 1H, ArH), 7.36 (qd, J_1 = 7.4 Hz J_2 = 1.8 Hz, 1H, ArH), 7.27 (m, 2H, ArH), 7.22, (qd, J_1 = 7.4 Hz J_2 = 1 Hz, 2H, ArH), 6.84 (d, J = 10.0 Hz, 1H, ArH).

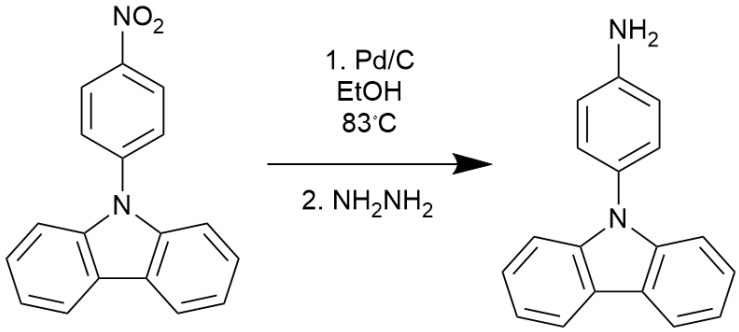

Synthesis of PSA-016[32]

This procedure has the same ratios as **PSA-018** and is similar to **PSA-025**, but without the 18-C-6.

PSA-015 (181 mg/ 0.704 mmol (1.0 equiv.)), 4-iodoanisole (182 mg/1.94 mmol (2.7 equiv.)), Cu powder (49.2 mg/ 1.94 mmol (2.5 equiv.)) and K_2CO_3 (105 mg/ 3.87 mmol (5.5 equiv.)) were added to DMA (10.1 ml) and heated at 175°C for >24 h. Extra 4-iodoanisole was added (308 mg) and left overnight. The reaction was then washed with brine and DCM, filtered and concentrated under reduced pressure. Column

chromatography (1:19 ethyl acetate and petroleum ether) produced a yellow solid (20 mg). Yield = 5.49%. Melting point: 72° C - 77° C. ν_{max} (cm^{-1}): 1500 ($C{=}C_{phenyl}$), 1454 ($C{=}C_{carbazole}$), 1313 ($C\text{-}N_{carbazole}$), 1237 (C-O), 1036 ($C\text{-}O_{methoxy}$), 826 ($C\text{-}H_{phenyl}$), 749 ($C\text{-}H_{carbazole}$). ^{1}H NMR δ: 8.20 (d, J = 8.0 Hz, 1H, ArH), 7.40 (m, 3H, ArH), 7.26 (qd, J_1 = 7.2 Hz J_2 = 2.0 Hz, 1H, ArH), 7.21 (d, J = 10.0 Hz, 2H, ArH), 7.08 (d, J = 9.0 Hz, 1H, ArH), 6.98 (dt, J_1 = 11.0 Hz J_2 = 4.0 Hz, 2H, ArH), 3.70 (s, 3H, $-OCH_3$). ^{13}C NMR δ: 206.5, 206.0, 157.8, 149.6, 142.3, 141.5, 128.7, 128.3, 127.0, 124.1, 121.2, 120.7, 116.0, 110.7, 55.9. Mass Spectroscopy (ESI^+) m/z: 471.2070. Purity = ~ 100%. Elemental Analysis: C (81.89%), H (5.55%), N (5.60%) (Expected: C (81.70%), H (5.53%), N (5.96%)).

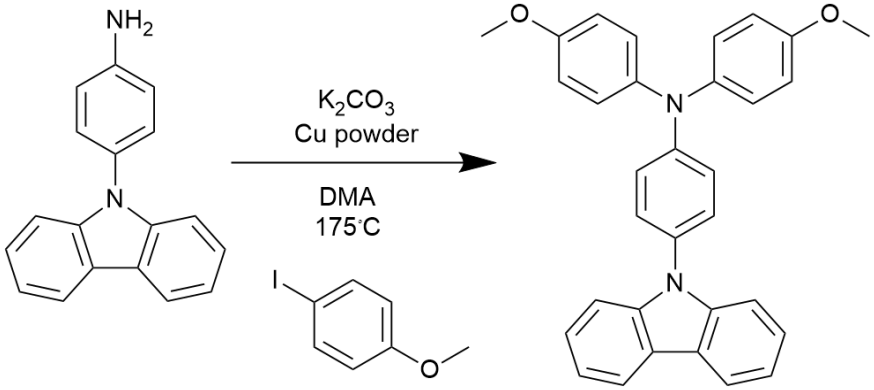

Attempted synthesis of PSA-021[10]

4-Bromophenol (1.81 g/ 10.4 mmol (1.0 equiv.)) was dissolved into DMF (15.0 ml), and placed in an ice bath for ~30 min. After that, TBDMS-Cl (2.38 g/ 15.7 mmol (1.5 equiv.)) and imidazole (1.20 g/ 17.8 mmol (1.7 equiv.)) were added and left under stirring under room temperature overnight (>4 h). The reaction was then poured into ice water (~0°C), NH_4Cl (15.0 ml of saturated solution) was added, and the crude material collected by filtration. Unfortunately, the analytical data was not consistent with the proposed structure of the product.

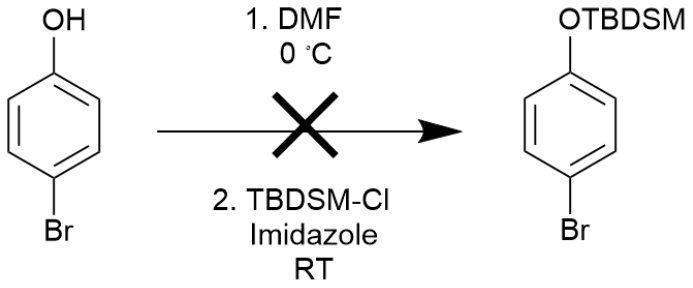

Synthesis of PSA-025[32]

This procedure is similar to **PSA-016/PSA-018**, but with 18-C-6 and Cu.

PSA-025 (1.91 g/ 7.41 mmol (1.0 equiv.)), 4-iodoanisole (3.66 g/ 15.7 mmol (2.1 equiv.), Cu powder (0.48 g/ 7.27 mmol (0.98 equiv.)), K_2CO_3 (2.16 g/ 15.5 mmol (2.1 equiv.)) and 18-crown-6 (102 mg/ 0.39 mmol (0.05 equiv.)) were added to DMA (21.0 ml) and left covered in Al paper and heated at ~175˚ C for >24 h. The reaction was then left to cool to room temperature, filtered under vacuum, washed with brine and DCM, dried with $MgSO_4$, filtered and concentrated under reduced pressure. Column chromatography (1:19 ethyl acetate petroleum ether) successfully obtained 235 mg of product. Yield = 6.73%. H^1 NMR is the same as the one mentioned at **PSA-016**.

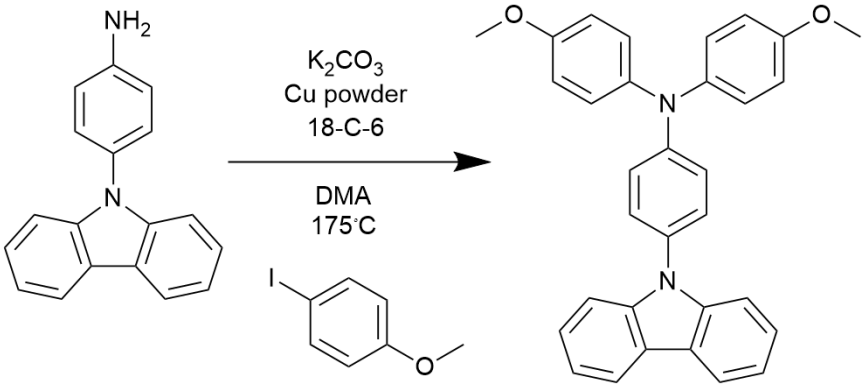

Synthesis of PSA-026[75]

Dimethoxycarbazole (1.00 g/ 4.40 mmol (1.0 equiv.)) and KOH (792 mg/ 14.1 mmol (3.2 equiv.)) were dissolved in acetone (10.0 ml), 1,4 dibromobutane (2.60 ml/ 21.8 mmol (5.0 equiv.)) was then added and left to react under stirring overnight at 20˚C. The reaction was then washed with brine and DCM, dried with $MgSO_4$, filtered and concentrated under reduced pressure. Column chromatography (1:9 ethyl acetate: petroleum ether) successfully obtained 0.56 g of product. Yield = 28.0%. ^1H NMR δ: 7.68 (d, J = 4.0 Hz, 1H, ArH), 7.46 (d, J = 8.0 Hz, 1H, ArH), 7.07 (dd, J_1 = 8.0 Hz J_2 = 2.8 Hz, 1H, ArH), 4.42 (t, J = 8.0 Hz, 1H, ArH), 3.88 (s, 3H, -OCH_3), 3.51 (t, J = 8.0 Hz, 1H, AlkH), 2.79 (m, 4H, AlkH).

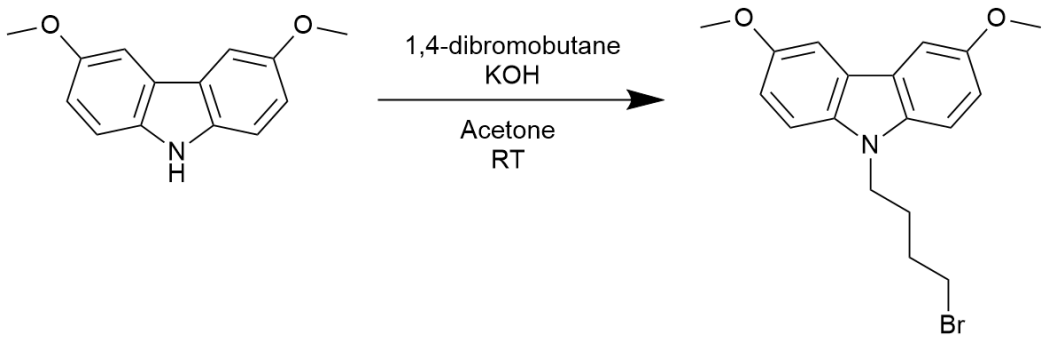

Synthesis of PSA-027[75]

For this reaction, three solutions are made, and then combined. In the first solution, NaH (1.26 g/ 31.5 mmol (20 equiv.)) was added to THF (15.0 ml) and degassed. For the second solution, hydroxymethyl EDOT (270 mg/ 1.57 mmol (1.0 equiv.)) and 18-crown-6 (32.0 mg/ 0.12 mmol (5% weight equiv.)) were added to THF (5.00 ml), and degassed. For the third solution, **PSA-026** (550 mg/ 1.52 mmol (1.0 equiv.)) was added to THF (~5.00 ml), and degassed. The first solution was placed on an ice bath for 15 min and once it reaches 0˚C, the second solution was added dropwise. This solution was then added to solution three, adding some THF (5.00 ml) to ensure the full transfer of materials. After 5 minutes, the reaction was heated to 75˚C and left overnight. The mixture was poured into water and washed with DCM. Brine was added and the organic layer was then dried with $MgSO_4$, filtered, and concentrated under reduced pressure. Purification using column chromatography (1:19 ethyl acetate: petroleum ether) resulted in the target product as an oil (~ 100 mg). Yield = 14.5%. ν_{max} (cm^{-1}): 3000 ($C\text{-}H_{alkyl}$), 1482 ($C{=}C_{carbazole}$), 1328 (C-N), 1289 ($C\text{-}H_{alkyl}$), 1158 ($C\text{-}O_{methoxy}$), 1066 ($C\text{-}O_{EDOT}$), 1020 and 912 (OC-O-CO), 758 ($C\text{-}H_{EDOT}$). ^{1}H NMR δ: 7.67 (d, J = 3 Hz, 2H, ArH), 7.43 (d, J = 8.0 Hz, 2H, ArH), 7.05 (dd, J_1 = 8.0 Hz J_2 = 4.0 Hz, 2H, ArH), 6.40 (q, J = 8.0 Hz, 2H, ArH), 4.36 (t, J = 6.8 Hz, 2H, AlkH), 4.23 (m, 2H, AlkH), 3.98 (dd, J_1 = 12.0 Hz J_2 = 8.4 Hz, 1H, AlkH), 3.59 (qd, J_1 = 10.0 Hz J_2 = 4.0 Hz, 2H, AlkH), 3.46 (t, J = 6.0 Hz, 2H, AlkH), 2.08 (s, 2H, EDOT ArH), 1.89 (quintuplet, J = 12.0 Hz, 2H, AlkH), 1.60 (quintuplet, J = 8.0 Hz, 2H, AlkH). ^{13}C NMR δ: 206.4, 206.0, 197.4, 157.8, 149.6, 142.3, 141.5, 128.8, 128.3, 127.0, 124.1, 121.2, 121.1, 120.7, 116.0, 110.8, 55.9. Mass Spectroscopy (ESI^+) m/z: 454.1693.

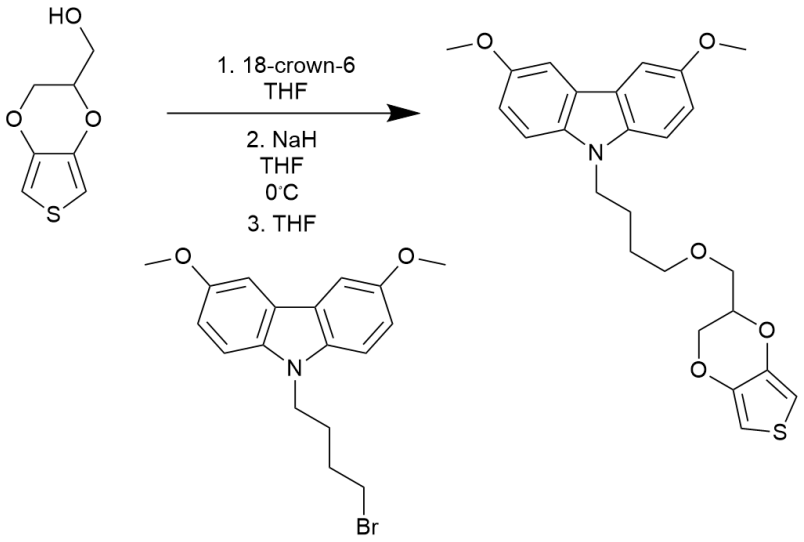

Appendix

1. Electrochemistry:

Figure 55: Bare ITO electrodes recorded in a DCM solution of electrolyte (from top to bottom: 25 scans, 50 scans, 75 scans and 100 scans):

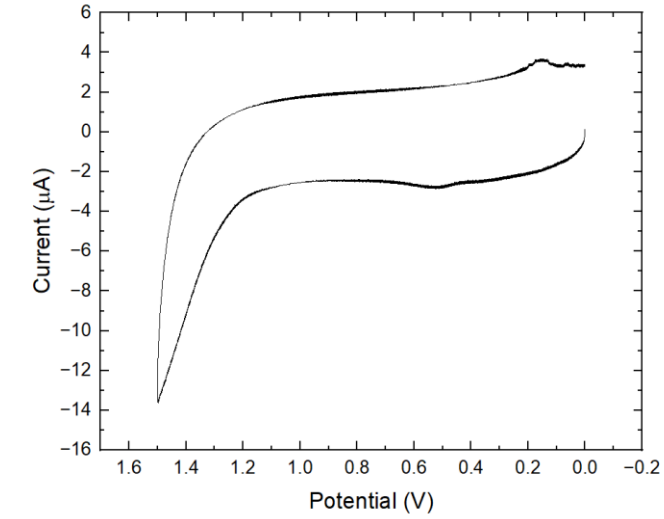

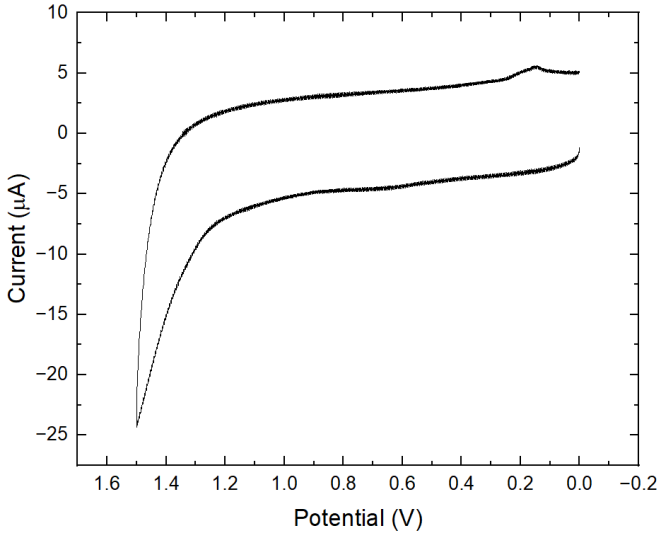

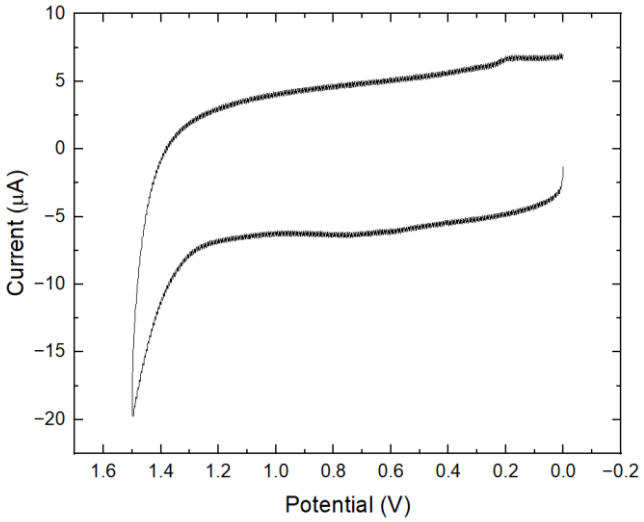
Current (μA)
Potential (V)
10
5
0
−5
−10
−15
−20
1.6
1.4
1.2
1.0
0.8
0.6
0.4
0.2
0.0
−0.2

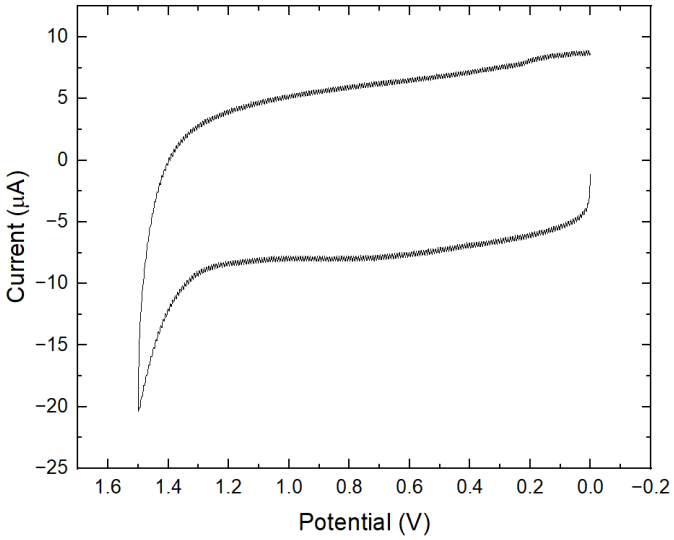
Current (μA)
Potential (V)
10
5
0
−5
−10
−15
−20
−25
1.6
1.4
1.2
1.0
0.8
0.6
0.4
0.2
0.0
−0.2

Figure 56: CVs showing the electropolymerization of **PSA-027** (top) and **PSA-013** (bottom) into ITO:

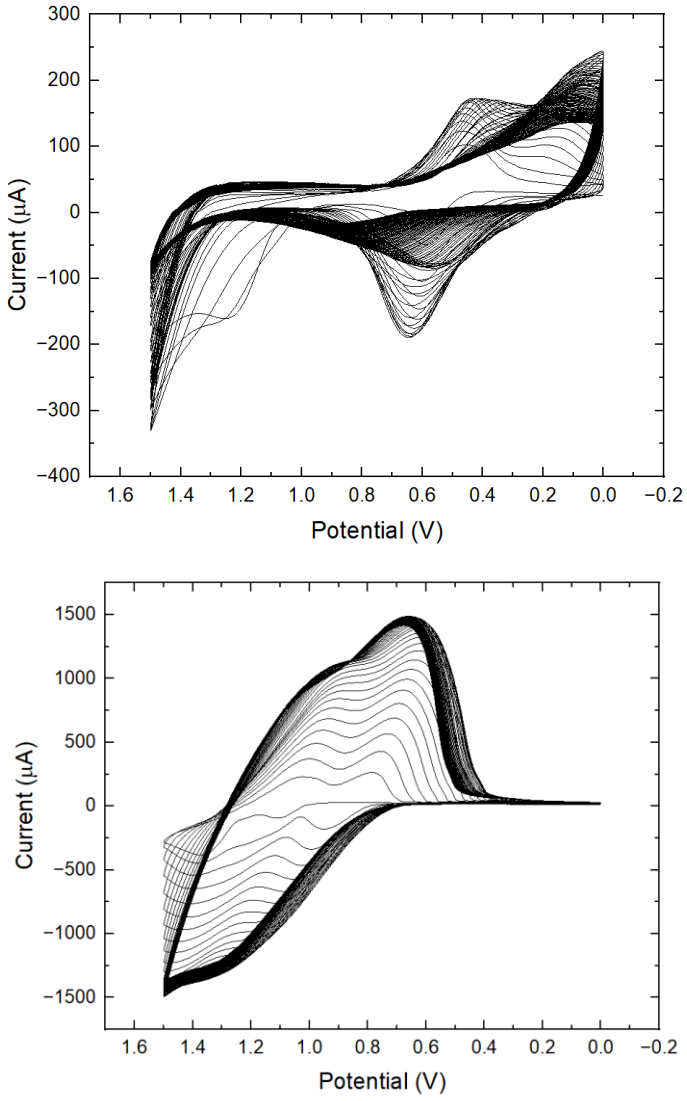

Figure 57: CVs of the electropolymerized **PSA-013** onto ITO used for conductivity measurements (from top to bottom: 25 scans, 50 scans, 75 scans and 100 scans):

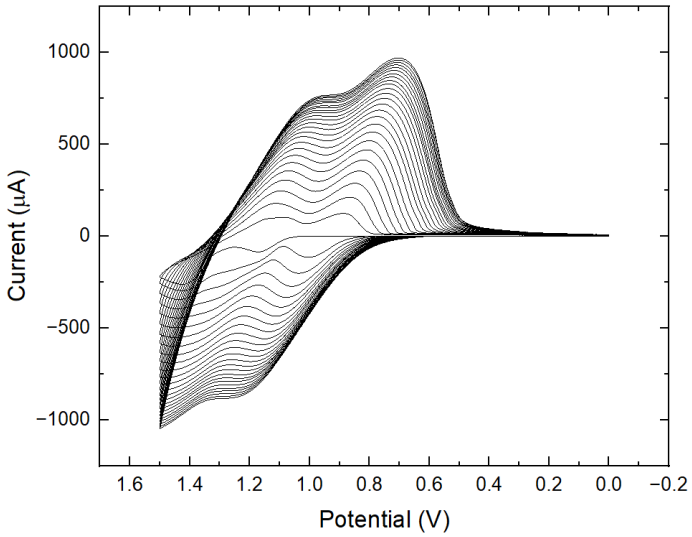

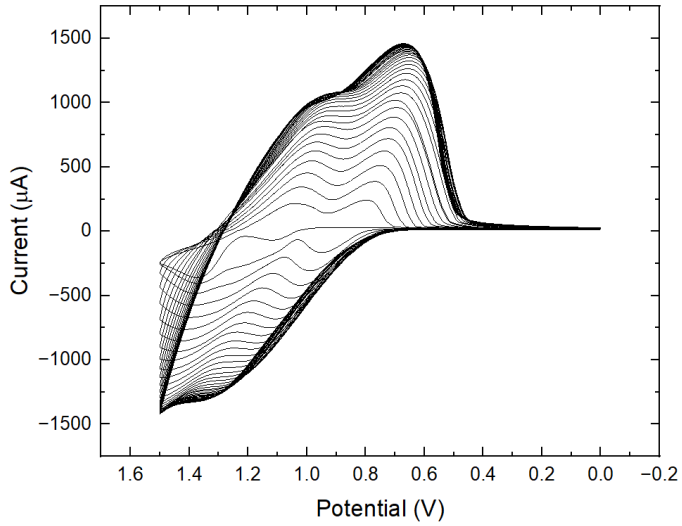

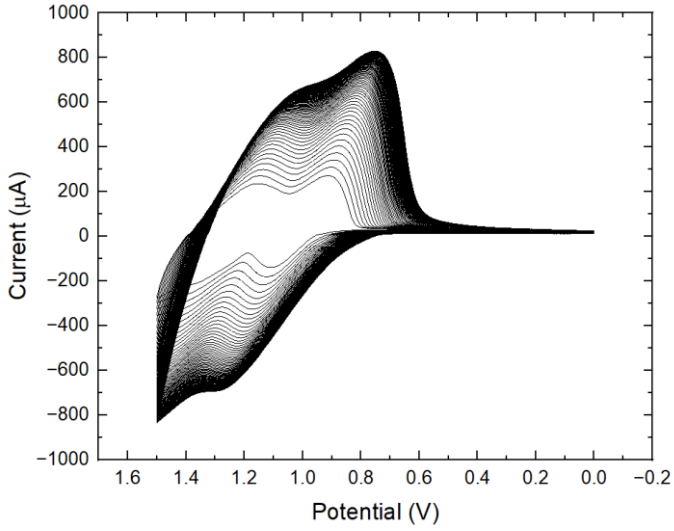

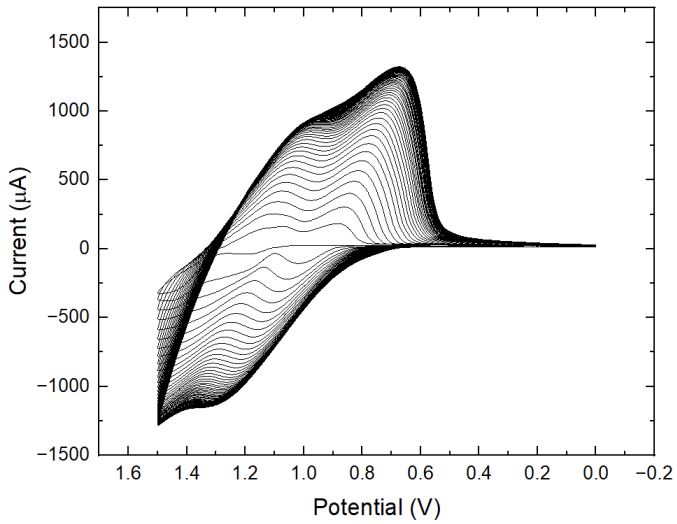

Figure 58: CVs of the electropolymerisation of **PSA-013** onto ITO used for thickness measurements (from top to bottom: 25 scans, 50 scans, 75 scans and 100 scans):

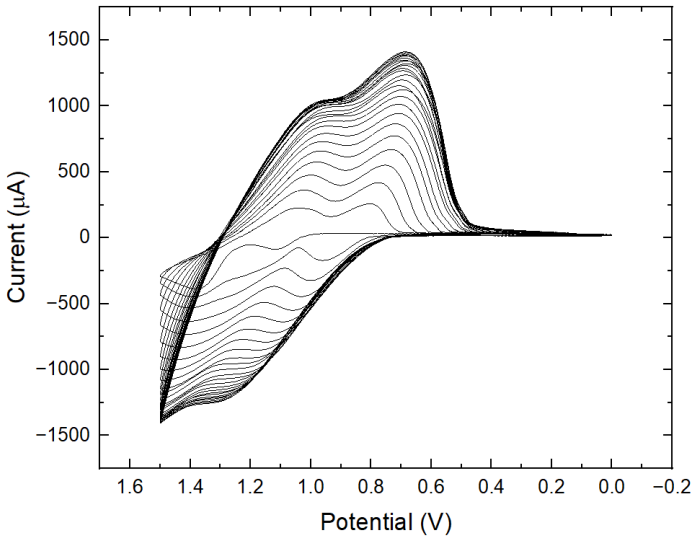

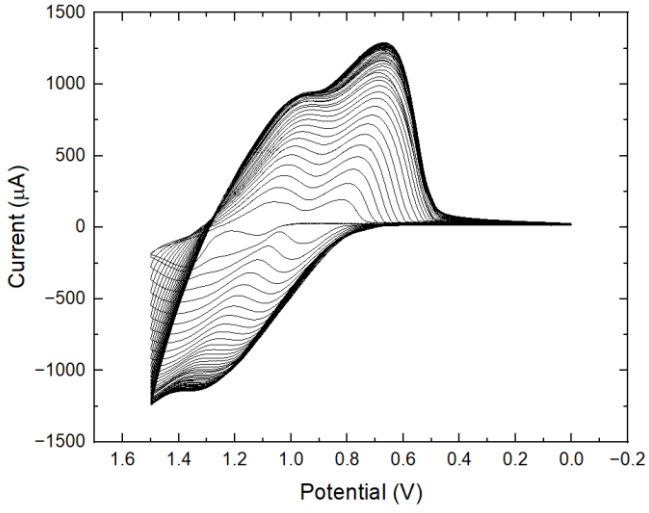

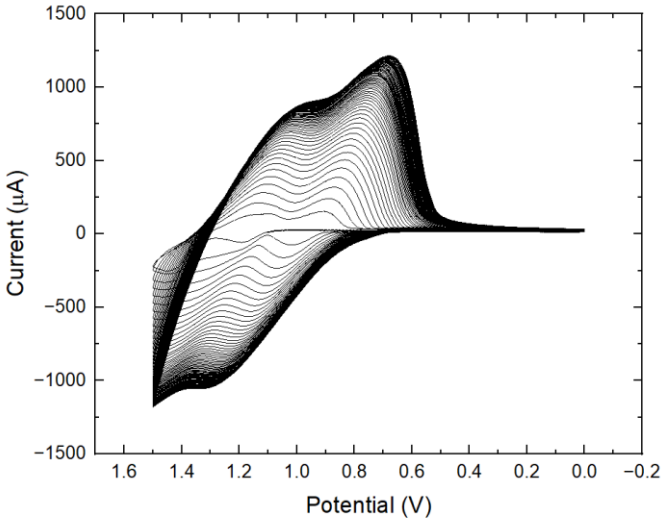
1500
1000
500
0
−500
−1000
−1500
Current (μA)
1.6
1.4
1.2
1.0
0.8
0.6
0.4
0.2
0.0
−0.2
Potential (V)

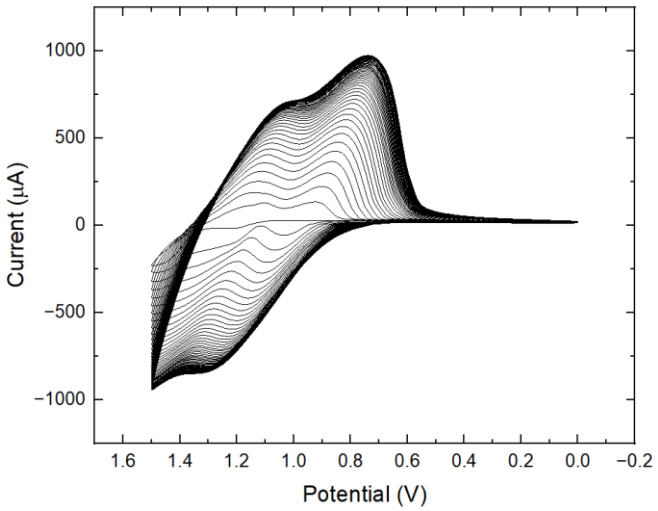
1000
500
0
−500
−1000
Current (μA)
1.6
1.4
1.2
1.0
0.8
0.6
0.4
0.2
0.0
−0.2
Potential (V)

Figure 59: CVs of the electropolymerisation of **PSA-027** onto ITO used for conductivity measurements (from top to bottom: 25 scans, 50 scans, 75 scans and 100 scans):

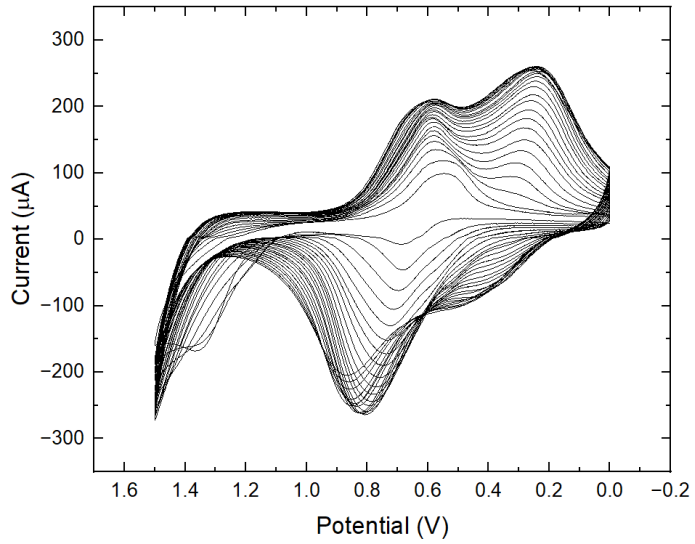

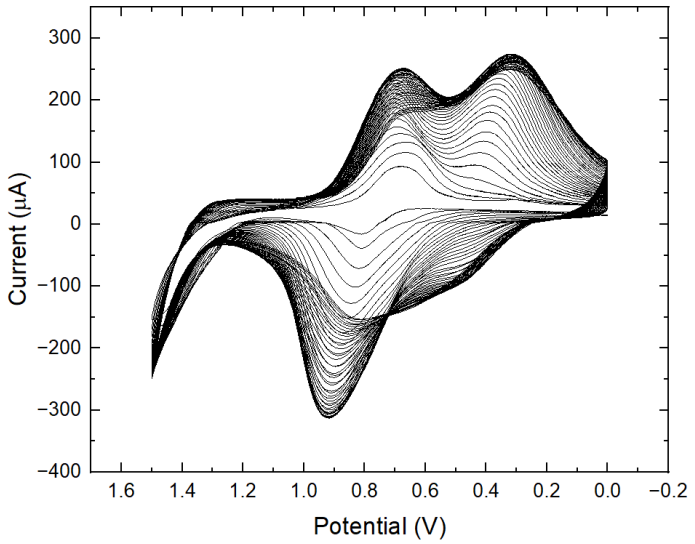

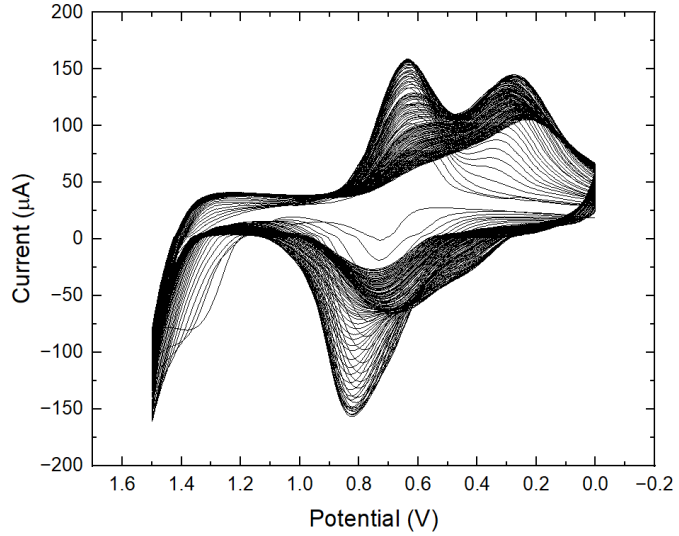

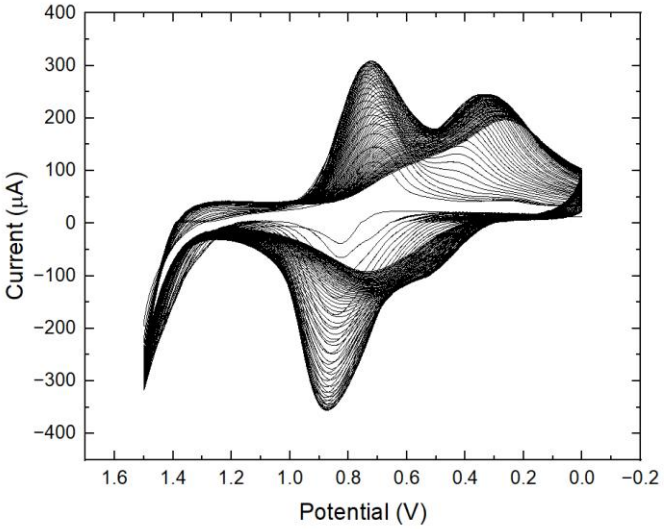
Current (μA)
400
300
200
100
0
−100
−200
−300
−400
1.6
1.4
1.2
1.0
0.8
0.6
0.4
0.2
0.0
−0.2
Potential (V)

Figure 60: CVs of the electropolymerisation of **PSA-027** onto ITO used for thickness measurements (from top to bottom: 25 scans, 50 scans, 75 scans and 100 scans):

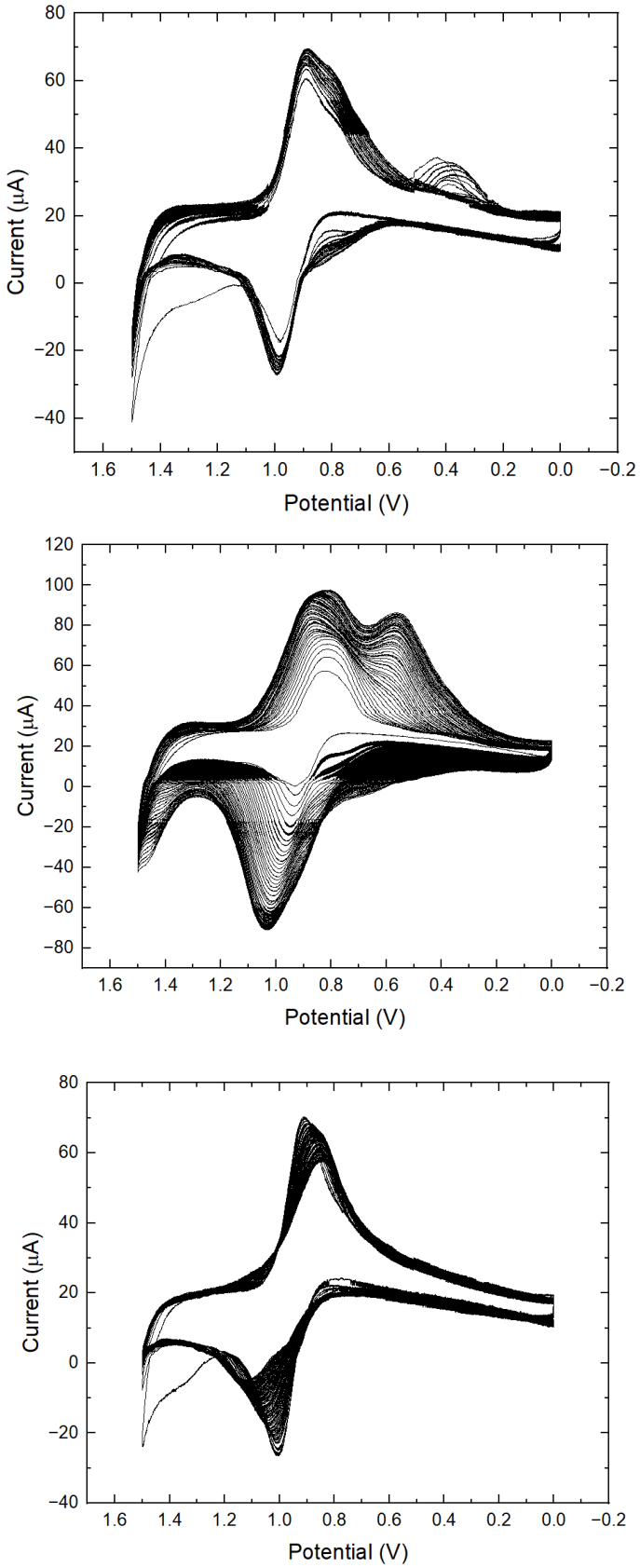

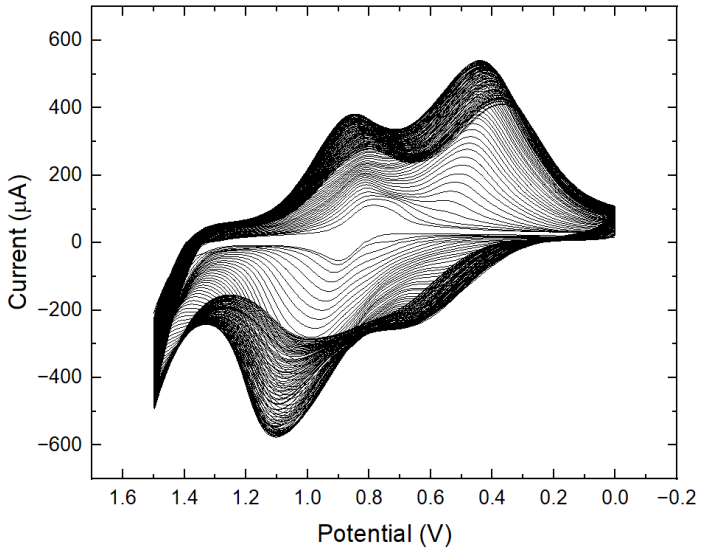

2. Film thickness measurements:

Figure 61: Comparative graphs between the difference in thickness throughout the slides of the two molecules (from top to bottom: 25 scans, 50 scans, 75 scans and 100 scans):

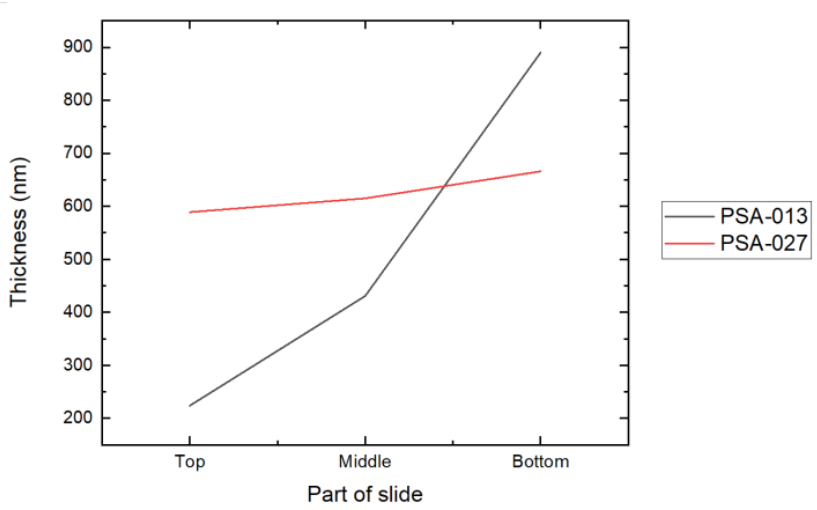

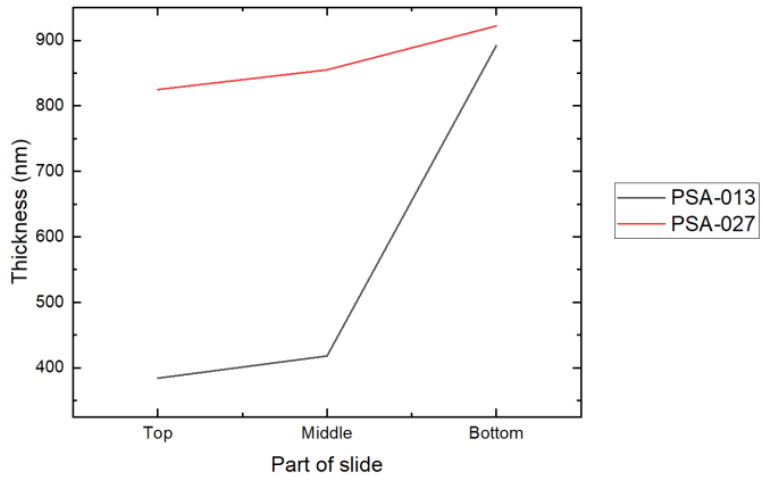
900
800
700
600
500
400
Thickness (nm)
Top
Middle
Bottom
Part of slide
PSA-013
PSA-027

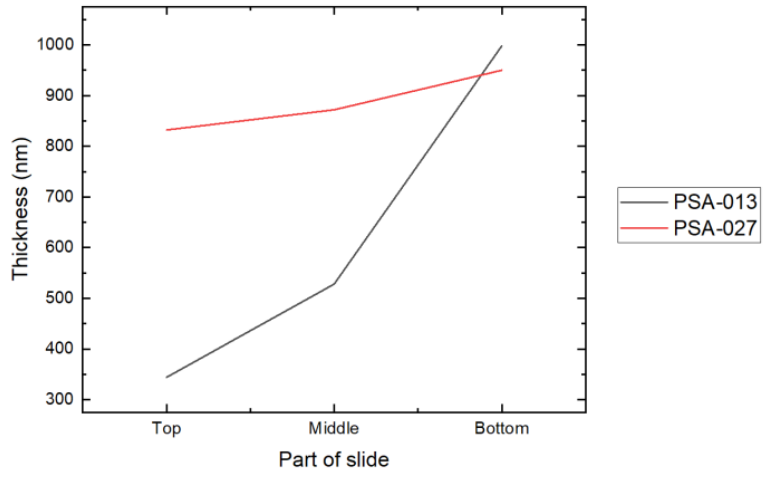
1000
900
800
700
600
500
400
300
Thickness (nm)
Top
Middle
Bottom
Part of slide
PSA-013
PSA-027

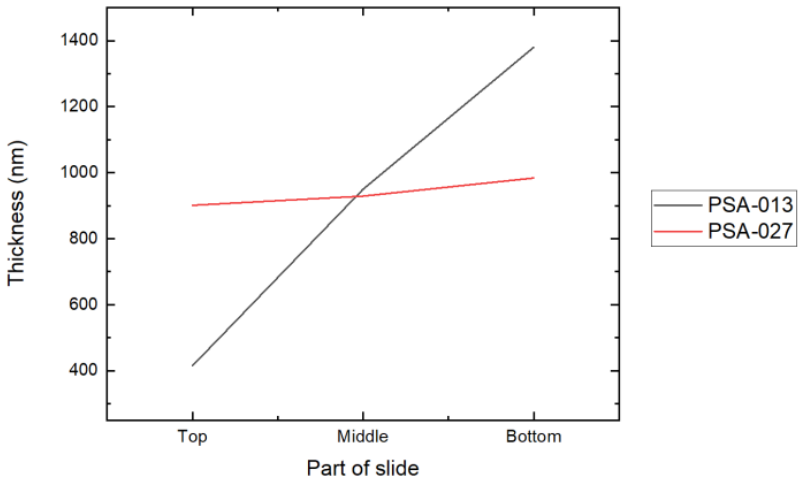
1400
1200
1000
800
600
400
Thickness (nm)
Top
Middle
Bottom
Part of slide
PSA-013
PSA-027

3. NMR spectra:

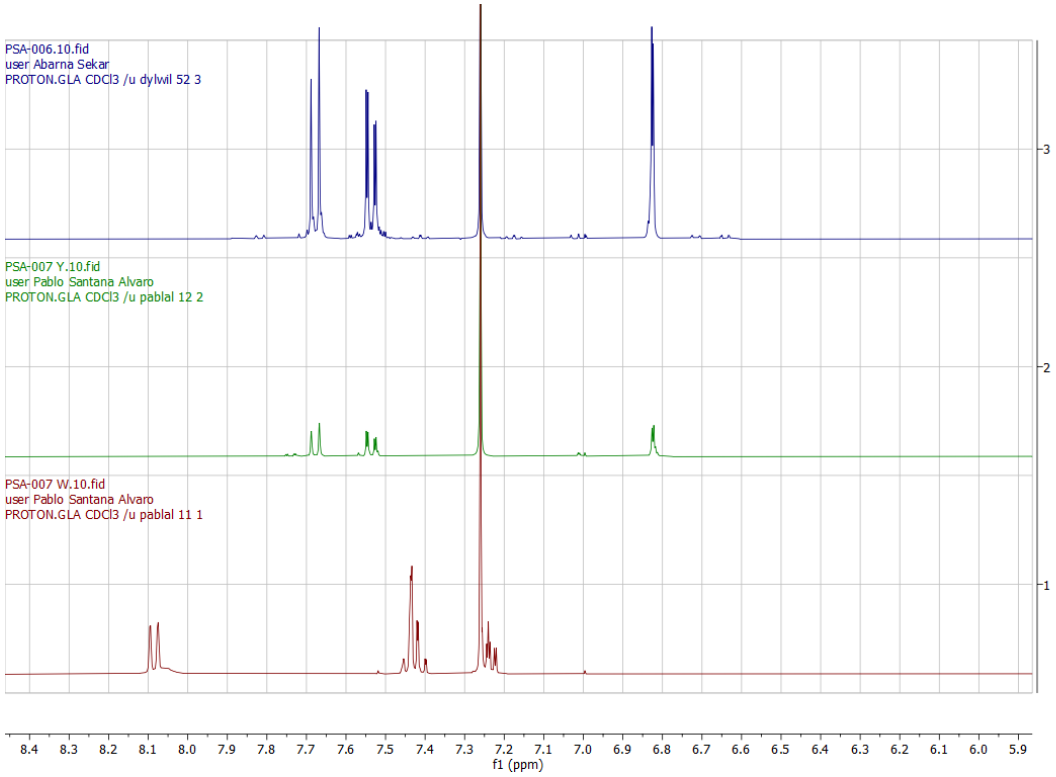

Figure 62: Comparative ^{1}H NMRs ($CDCl_3$) between **PSA-006** (top) and **PSA-007**. Within **PSA-007** there were two solids, a white one (W, bottom) and a yellow one (Y, middle)

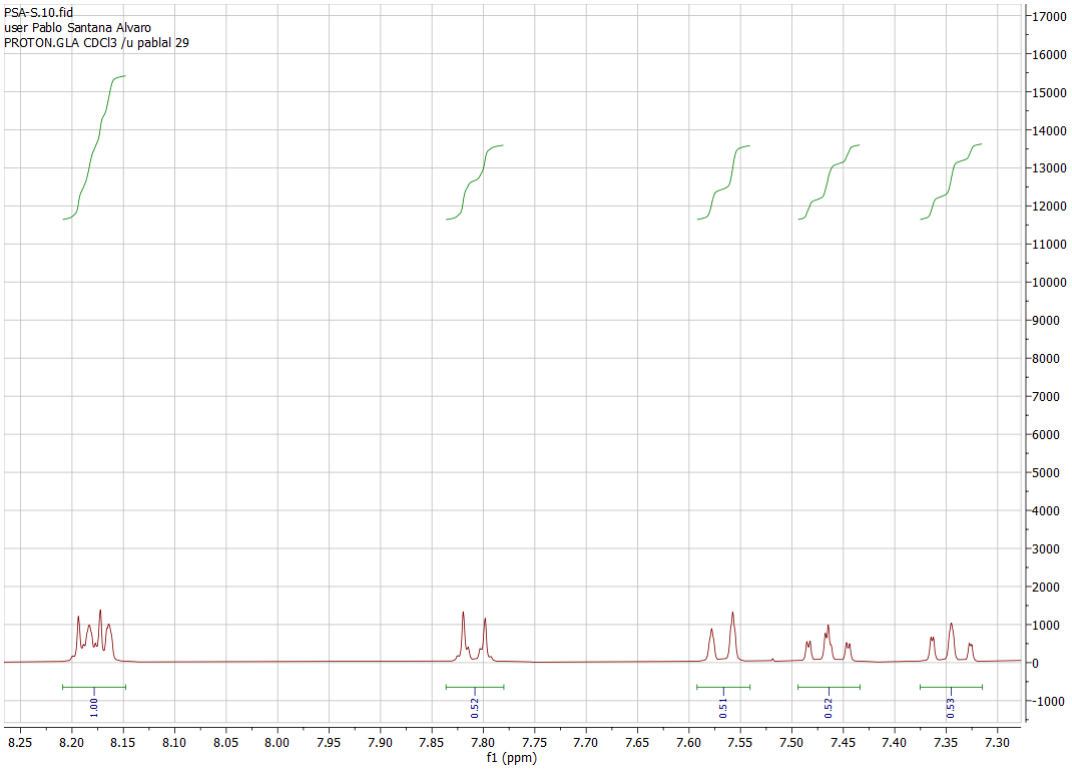

Figure 63: Partial ^{1}H NMR ($CDCl_3$) of **PSA-012**

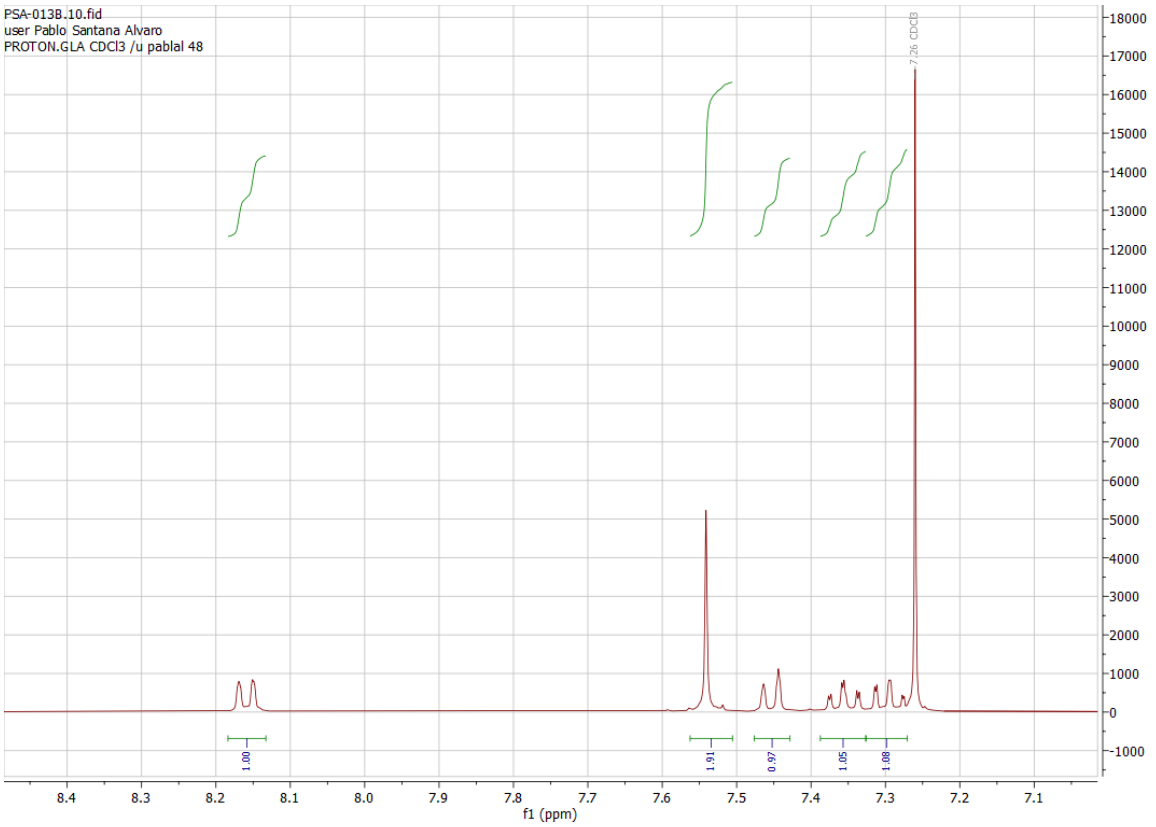

Figure 64: Partial ^{1}H NMR ($CDCl_3$) of **PSA-013**

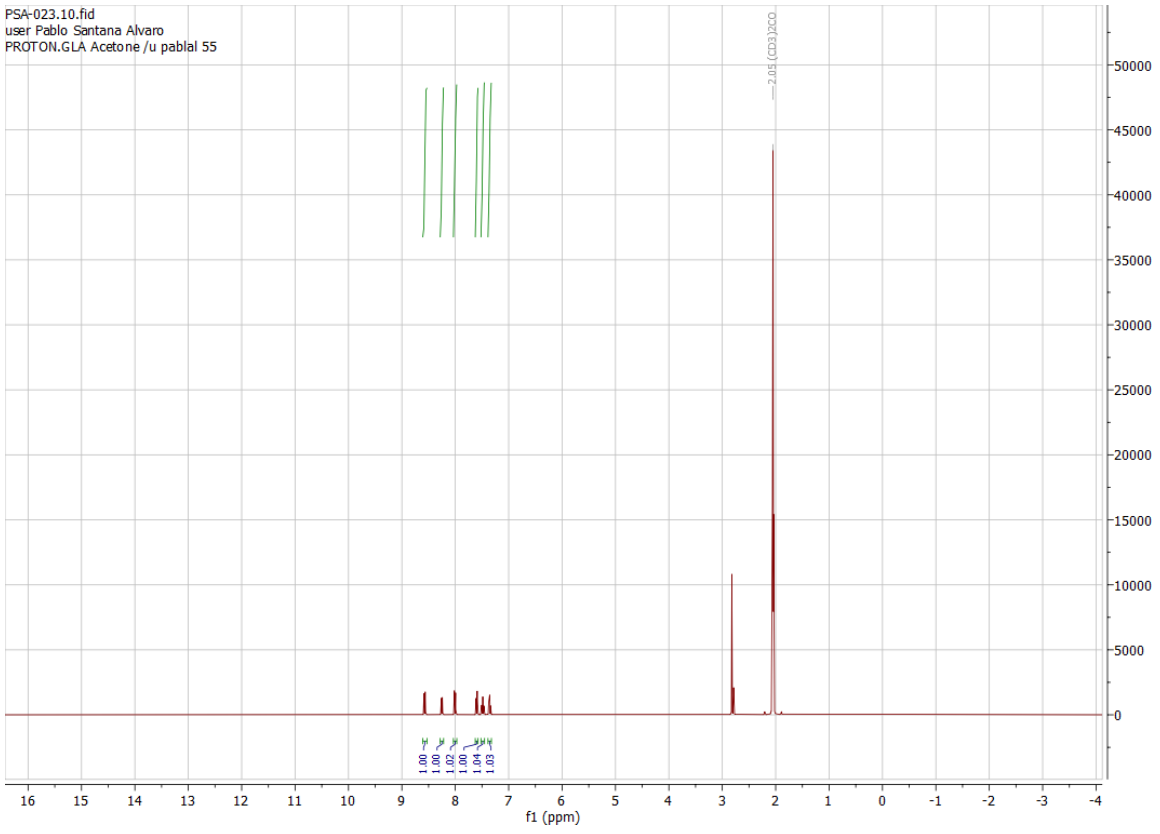

Figure 65: ^{1}H NMR (d6-acetone) of **PSA-014/PSA-023**

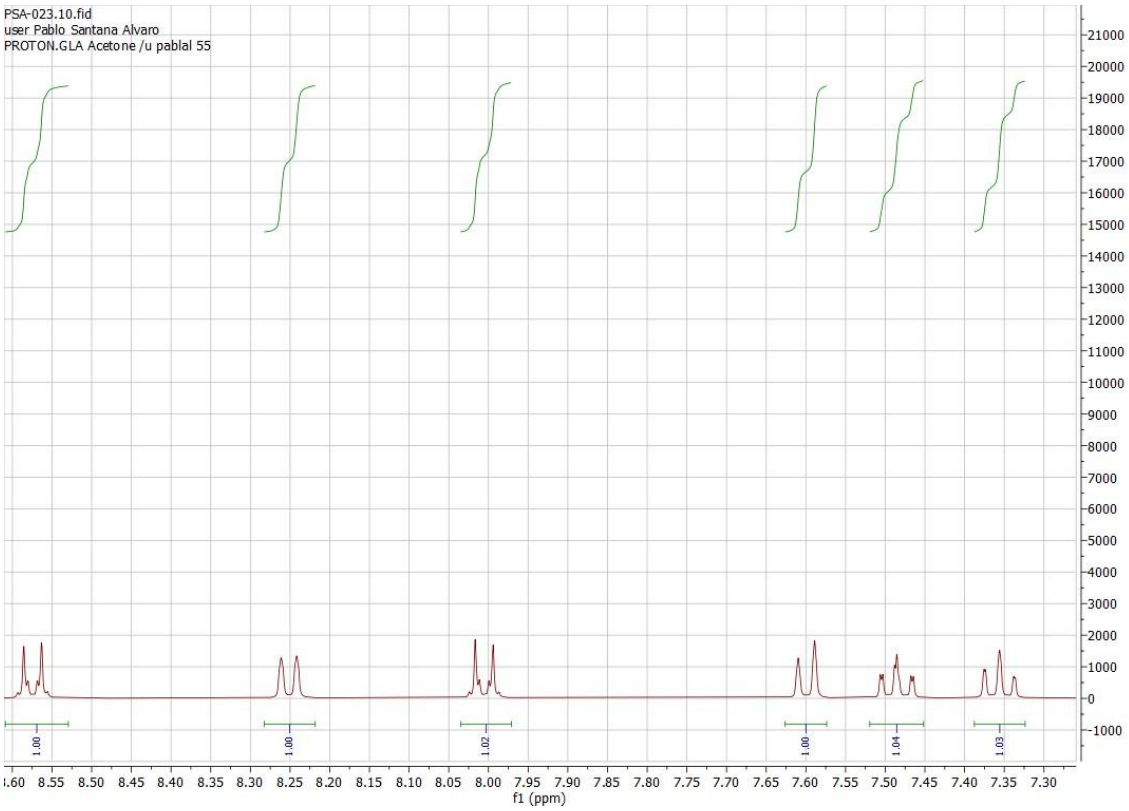

Figure 66: Partial ^{1}H NMR (d6-acetone) of **PSA-014/PSA-023**

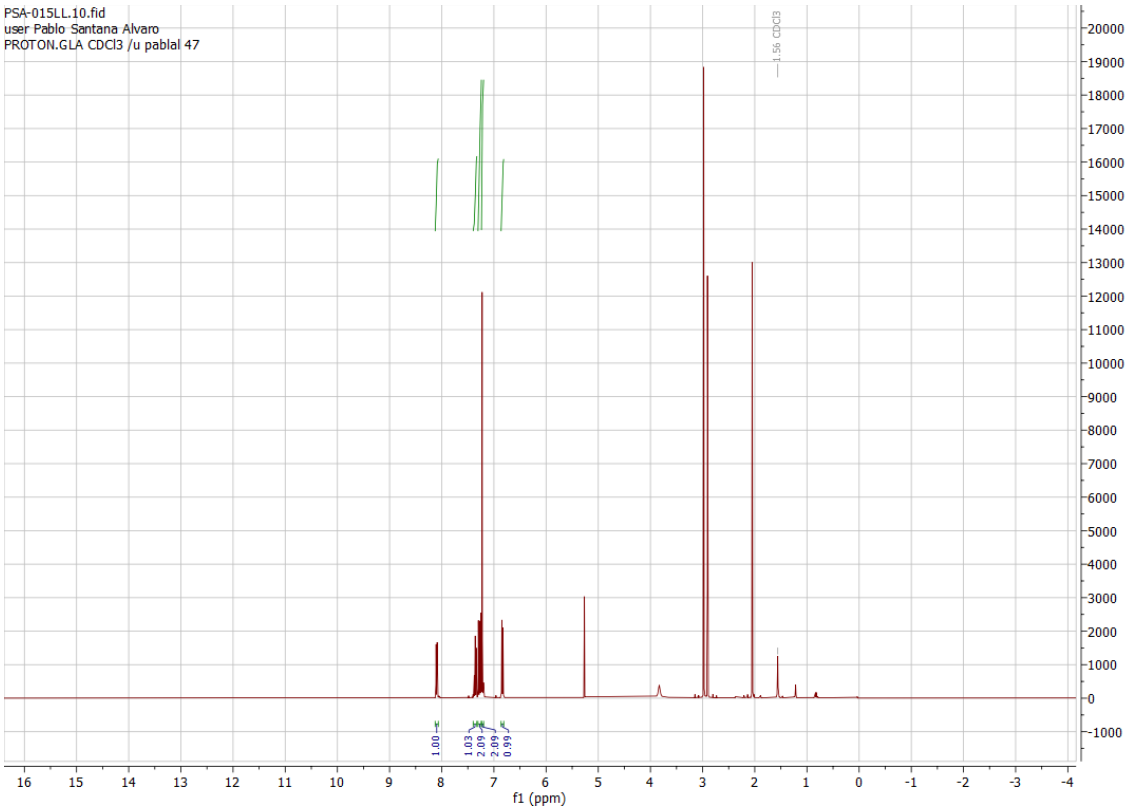

Figure 67: ^{1}H NMR ($CDCl_3$) of **PSA-015**

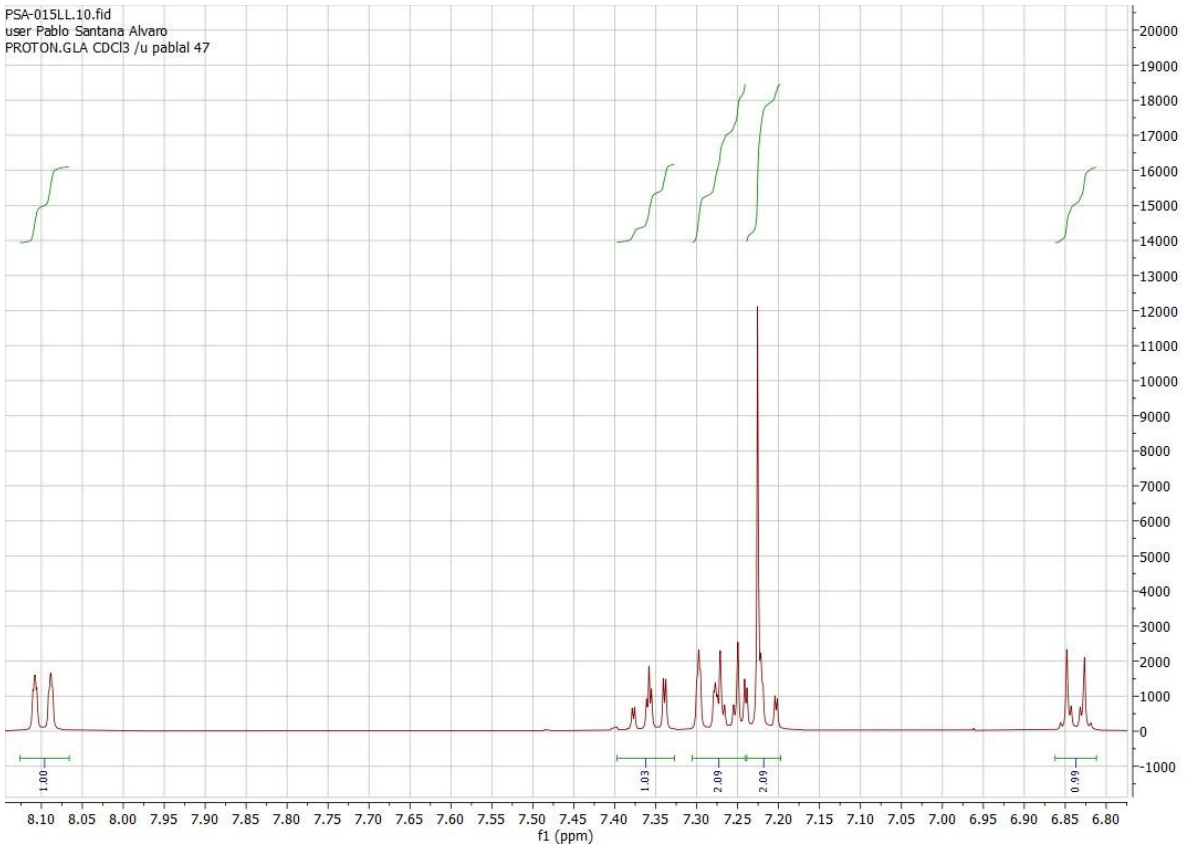

Figure 68: Partial ^{1}H NMR ($CDCl_3$) of **PSA-015**

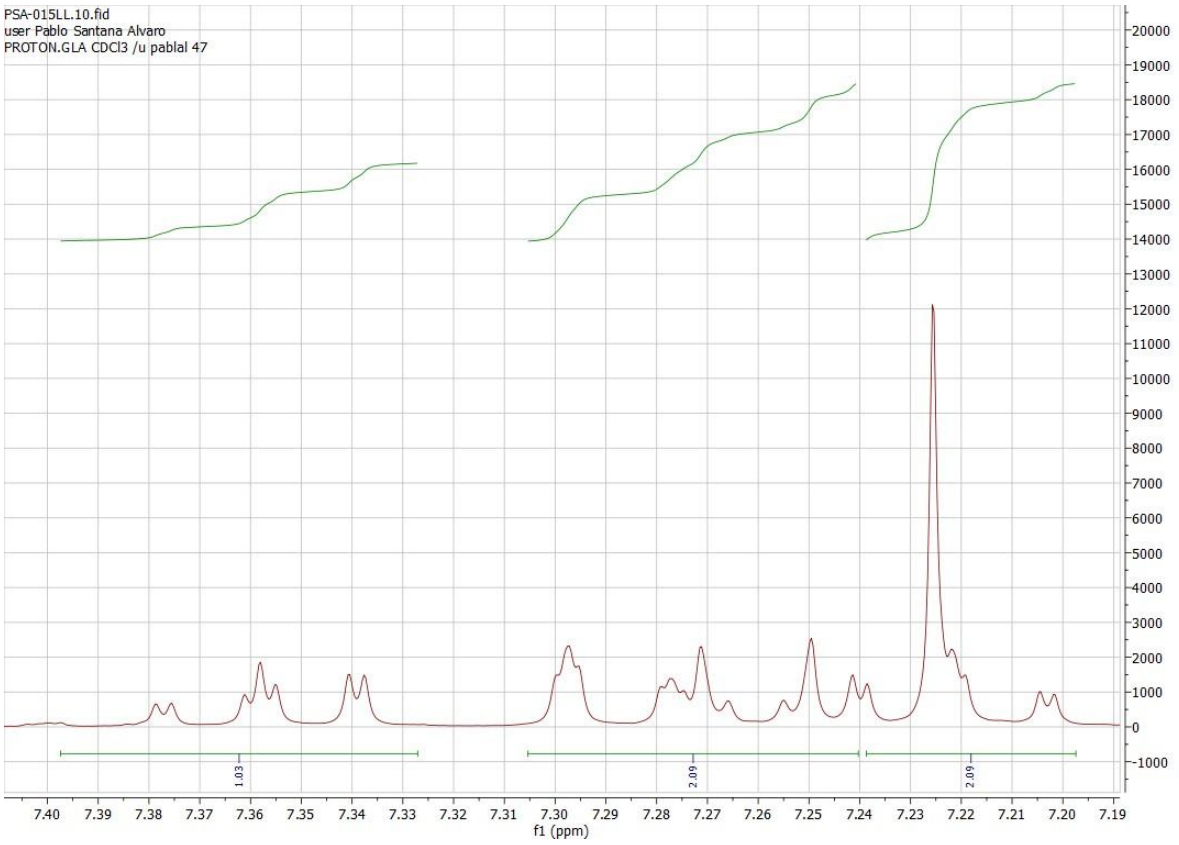

Figure 69: Partial ^{1}H NMR ($CDCl_3$) of **PSA-015**

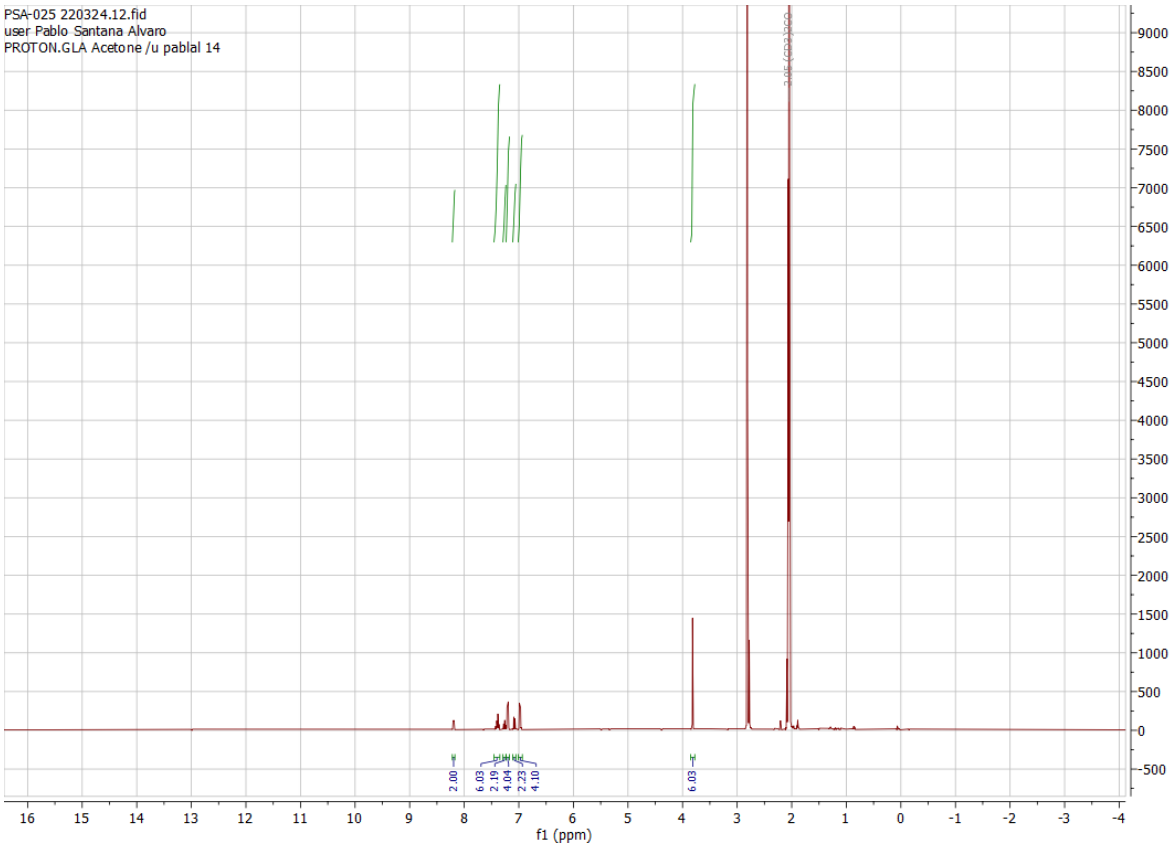

Figure 70: ^{1}H NMR (d6-acetone) of **PSA-018/025**

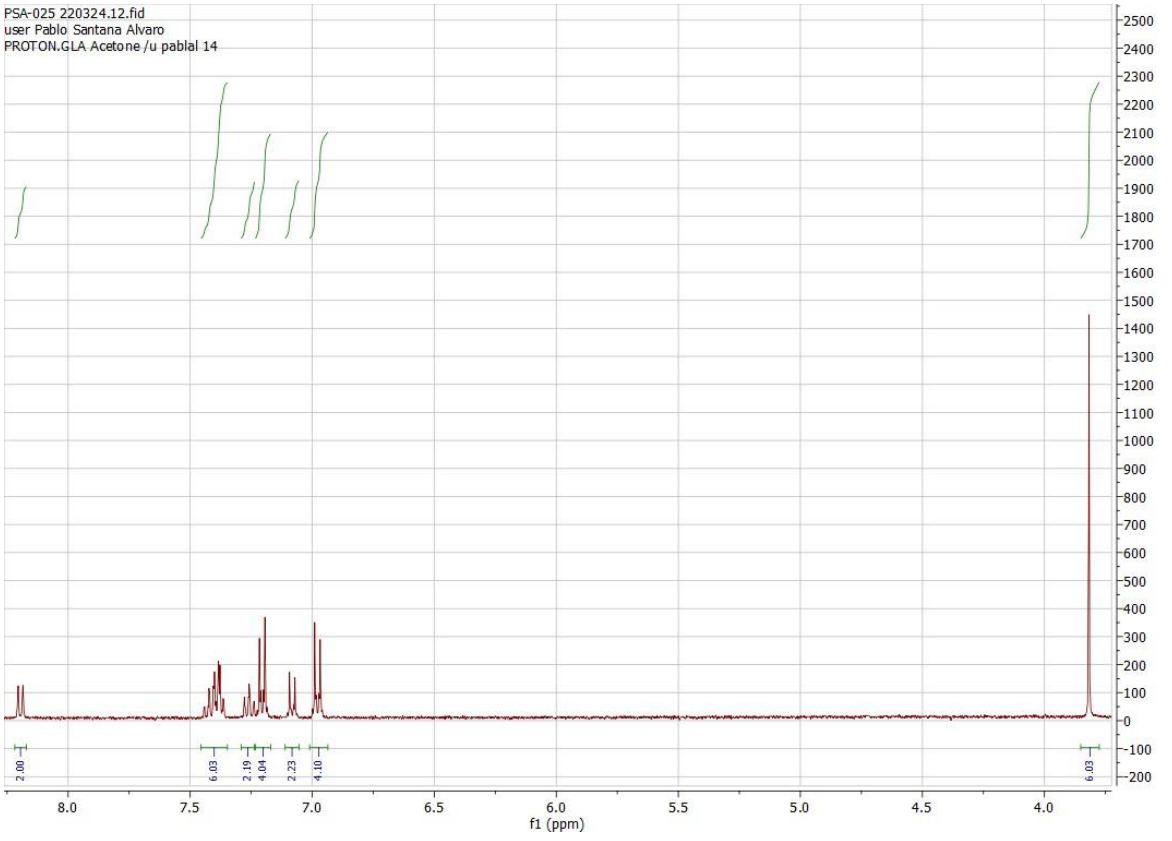

Figure 71: Partial ^{1}H NMR (d6-acetone) of **PSA-018/025**

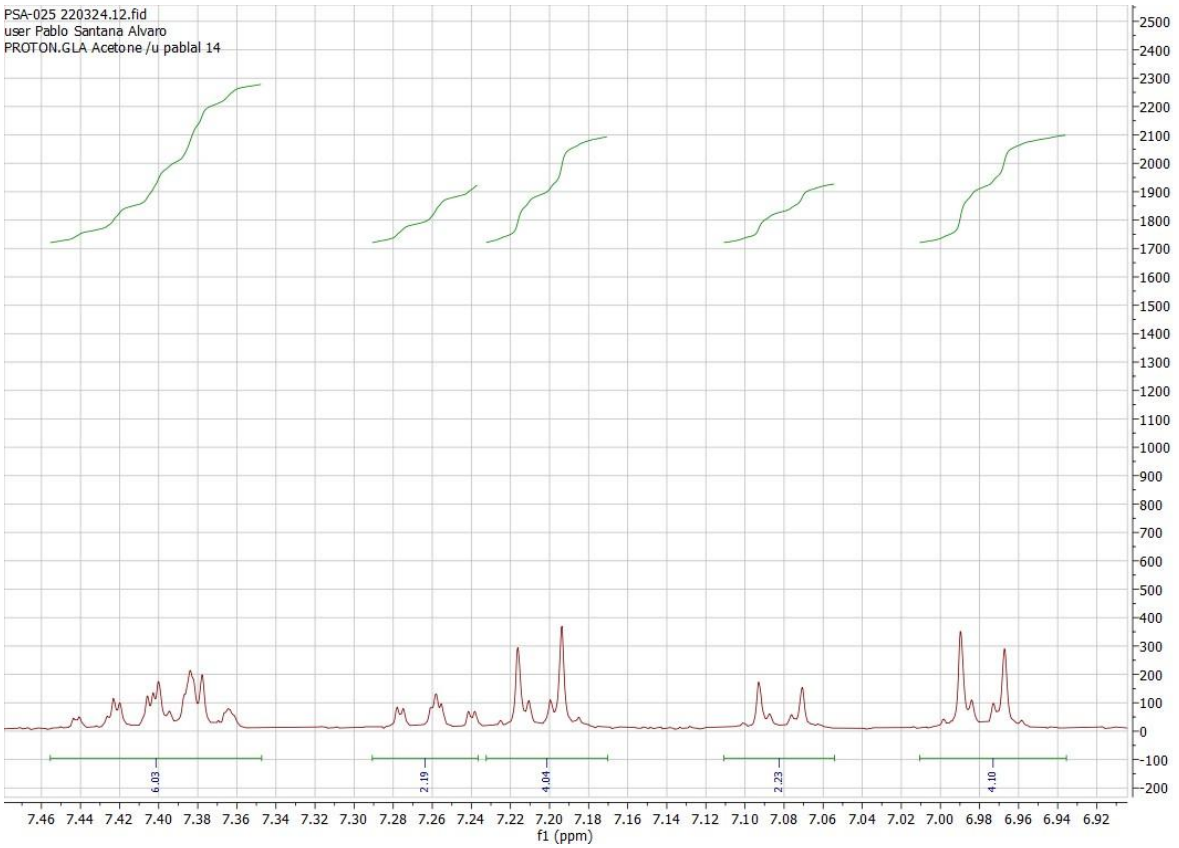

Figure 72: Partial ^{1}H NMR (d6-acetone) of **PSA-018/025**

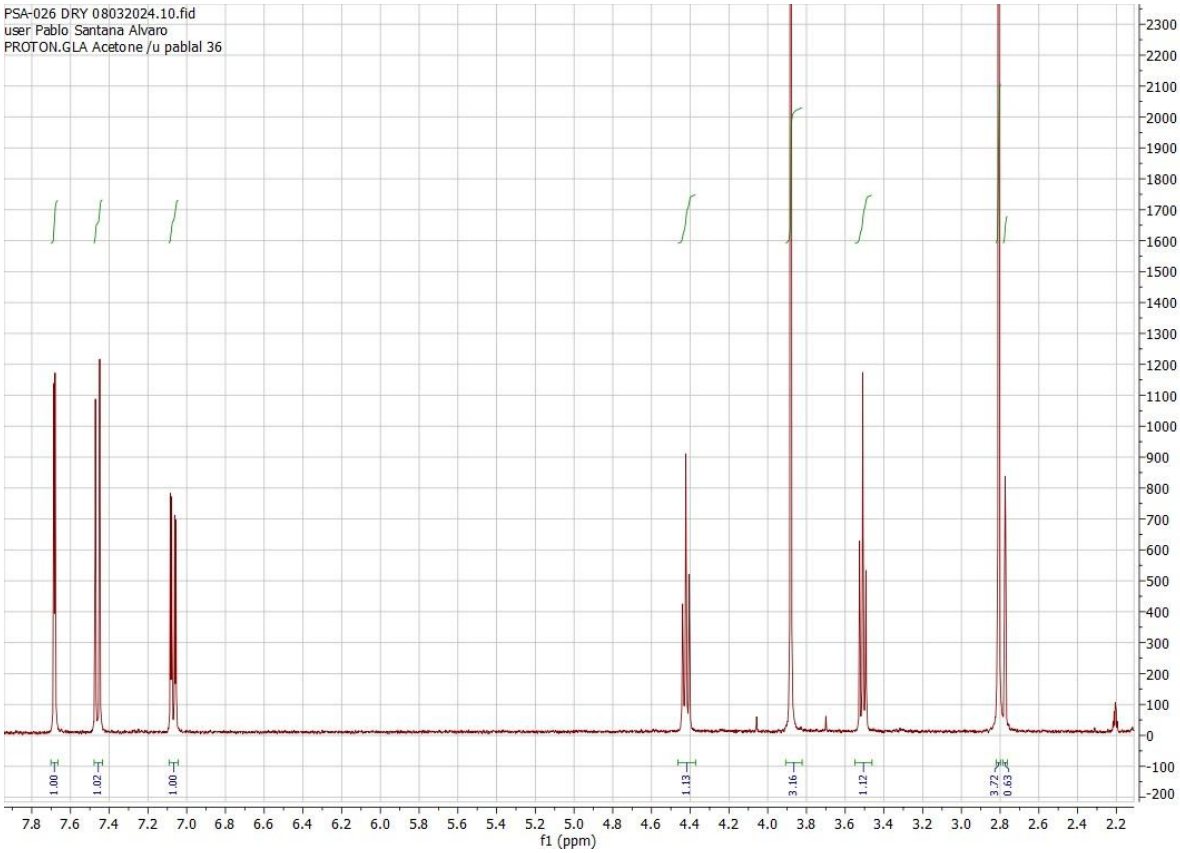

Figure 73: ^{1}H NMR (d6-acetone) of **PSA-026**

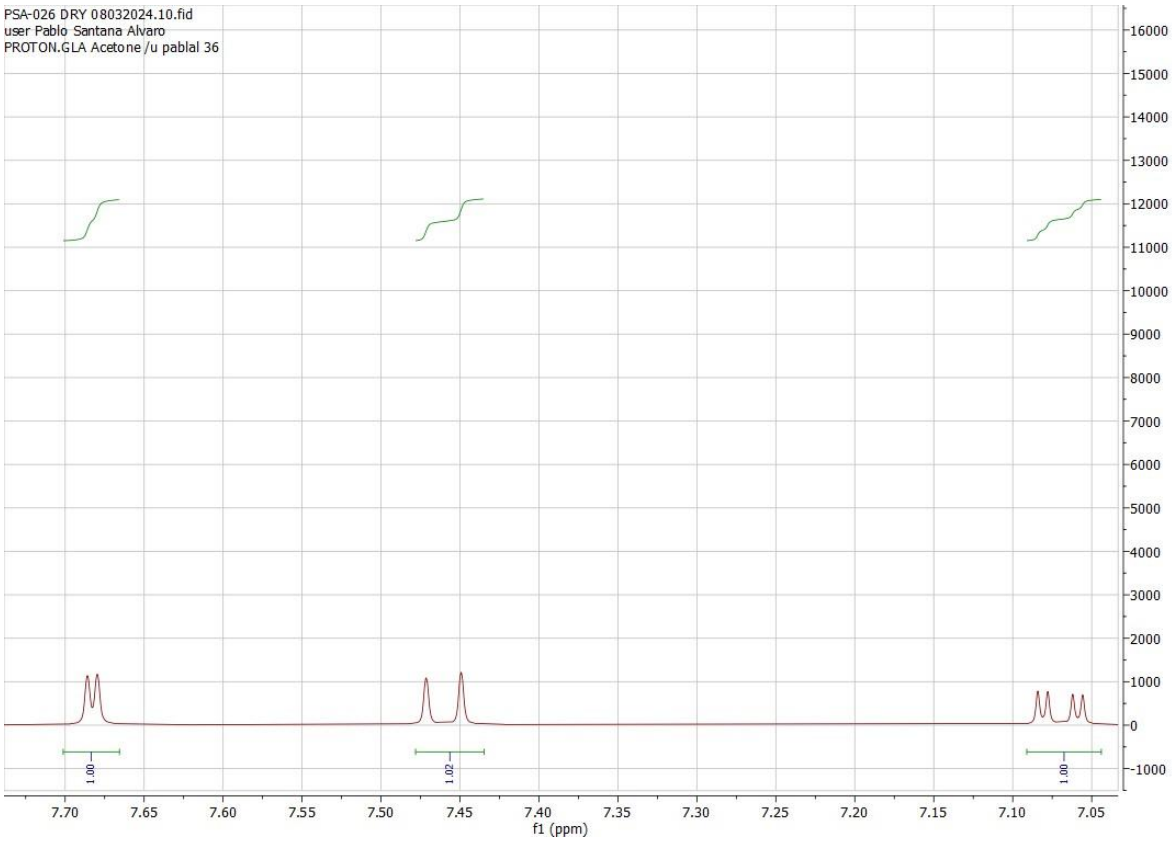

Figure 74: Partial H[1]NMR (d6-acetone) of **PSA-026**

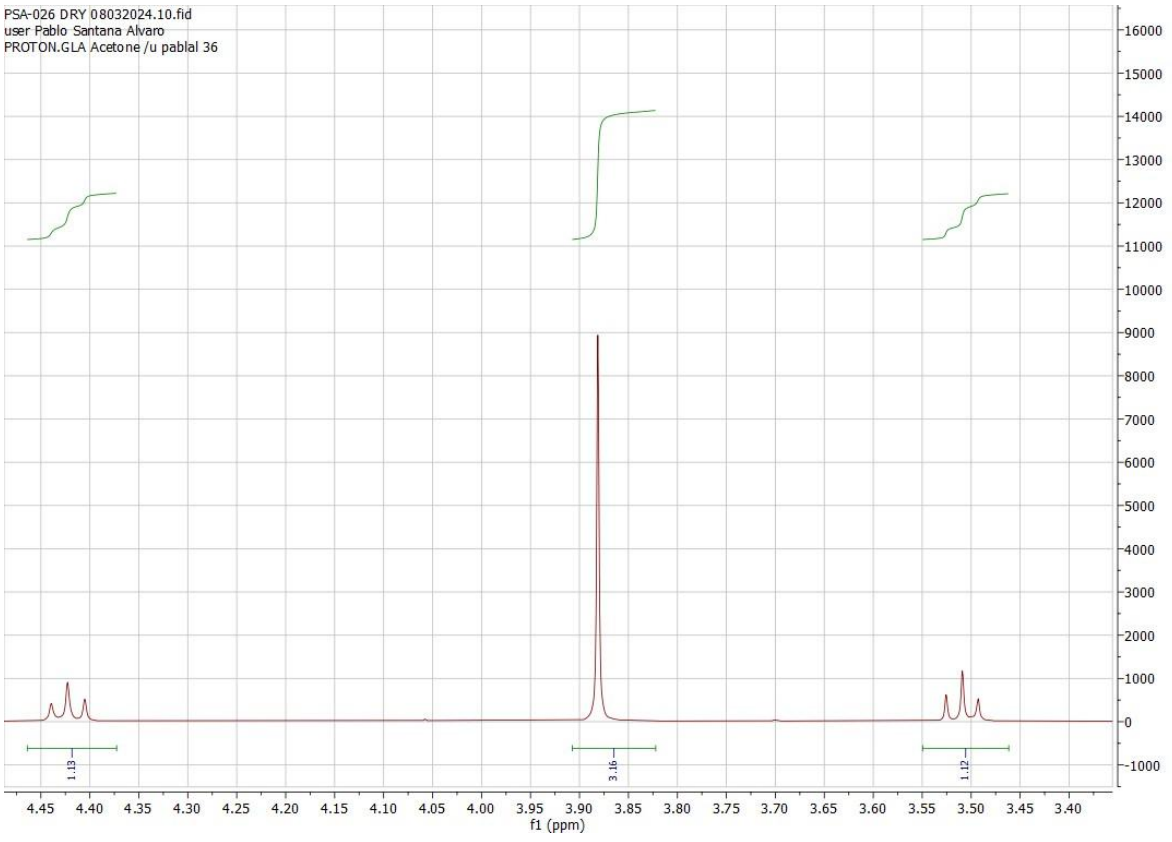

Figure 75: Partial [1]H NMR (d6-acetone) of **PSA-026**

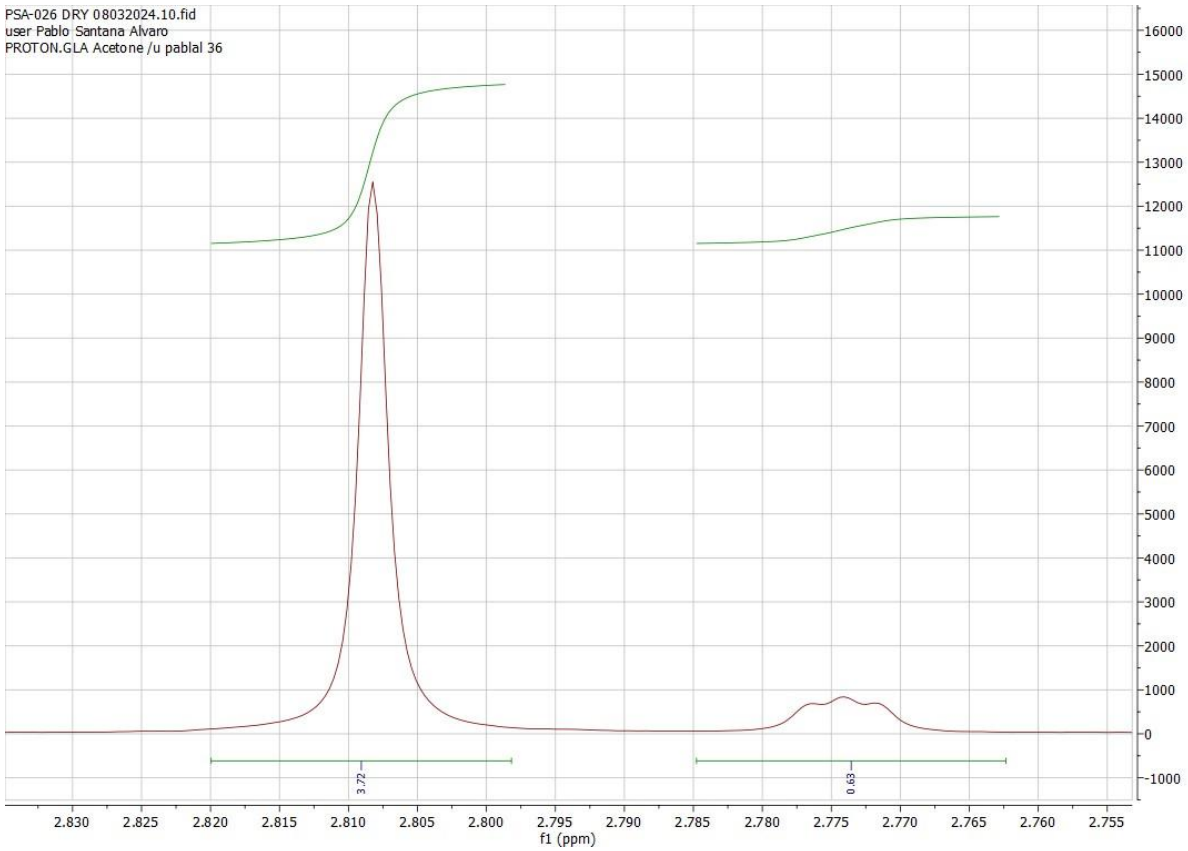

Figure 76: Partial ^{1}H NMR (d6-acetone) of **PSA-026**

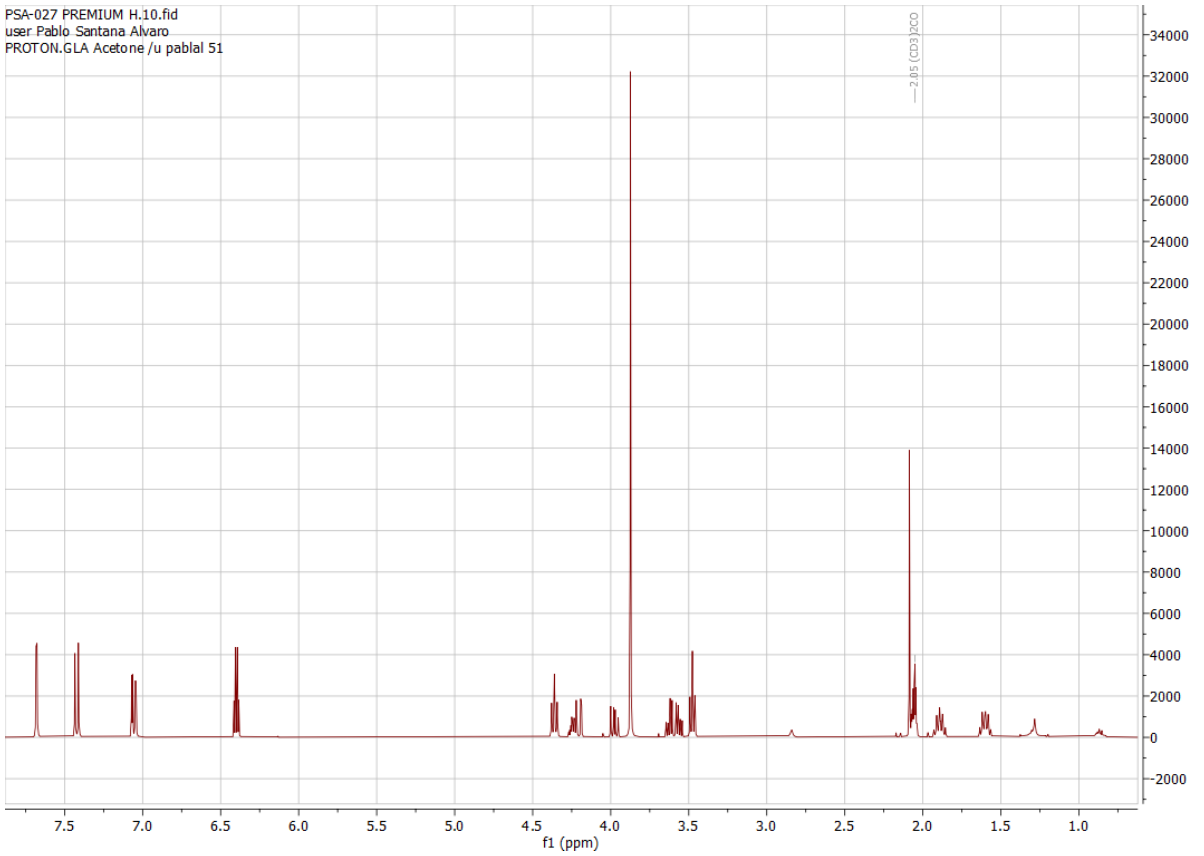

Figure 77: ^{1}H NMR (d6-acetone) of **PSA-027**

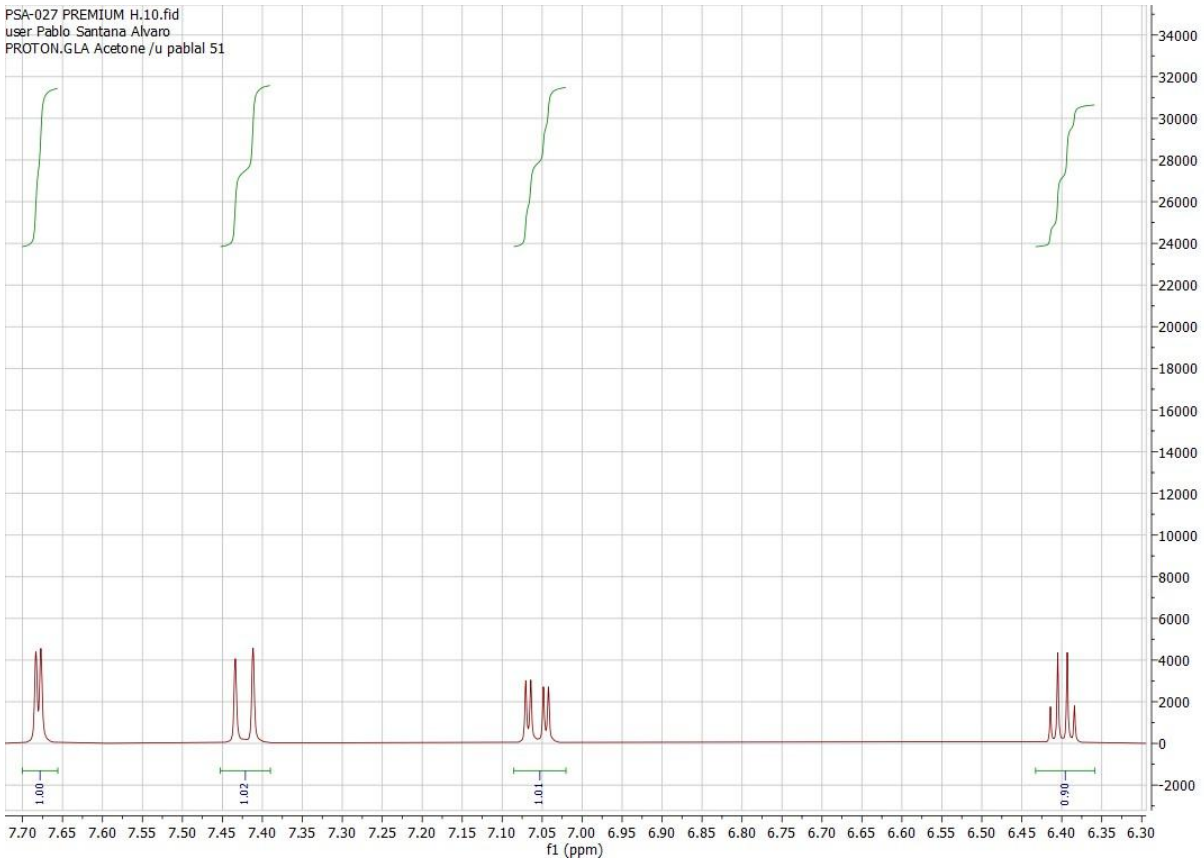

Figure 78: Partial ^{1}H NMR (d6-acetone) of **PSA-027**

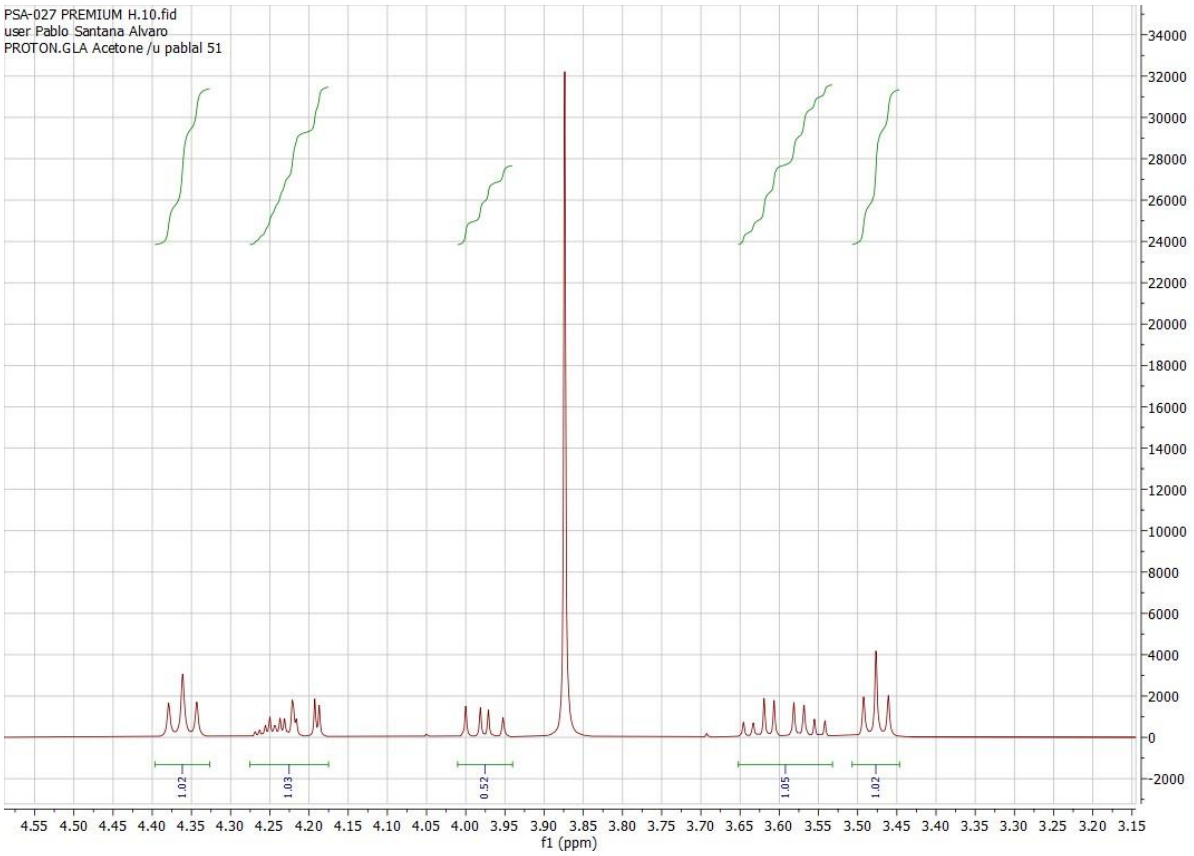

Figure 79: Partial ^{1}H NMR (d6-acetone) of **PSA-027**

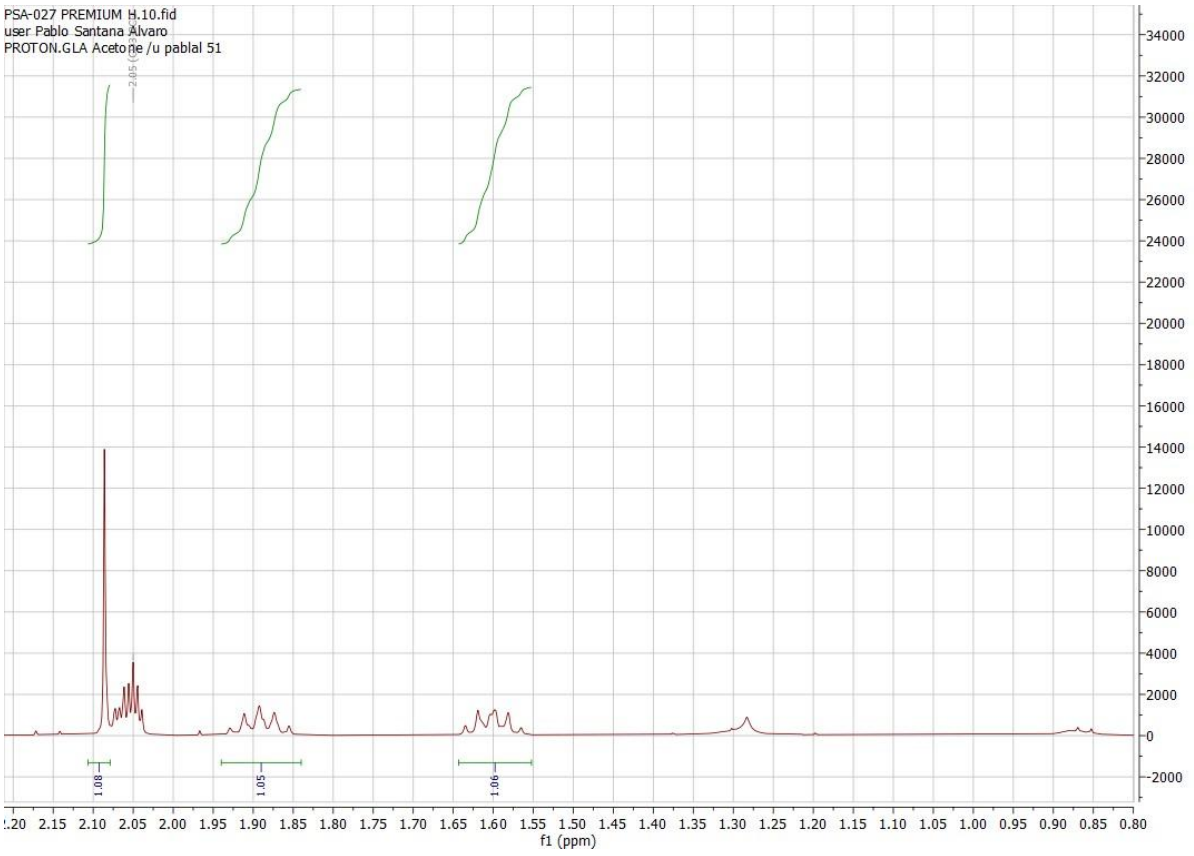

Figure 80: Partial ^{1}H NMR (d6-acetone) of **PSA-027**

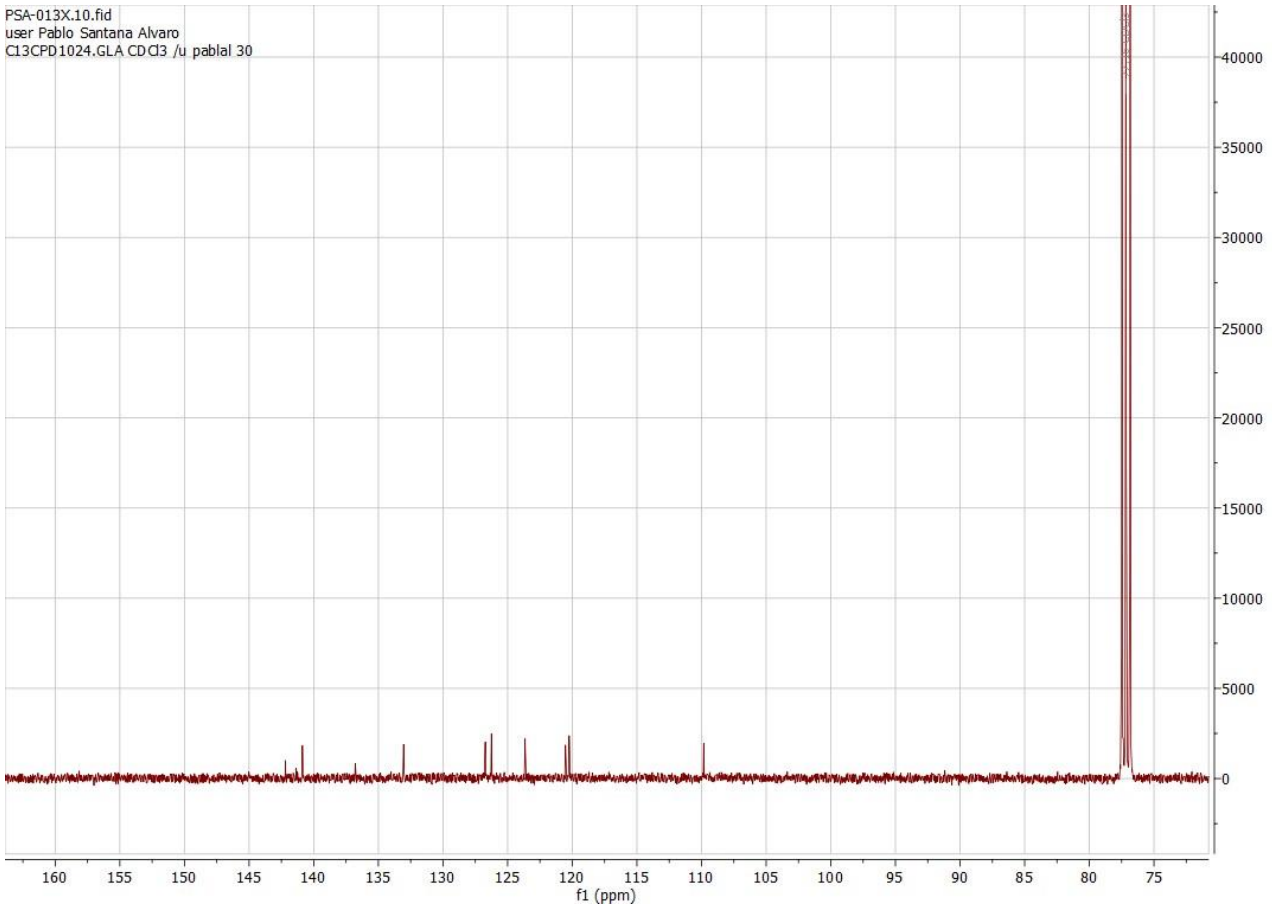

Figure 81: ^{13}C NMR ($CDCl_3$) of **PSA-013**

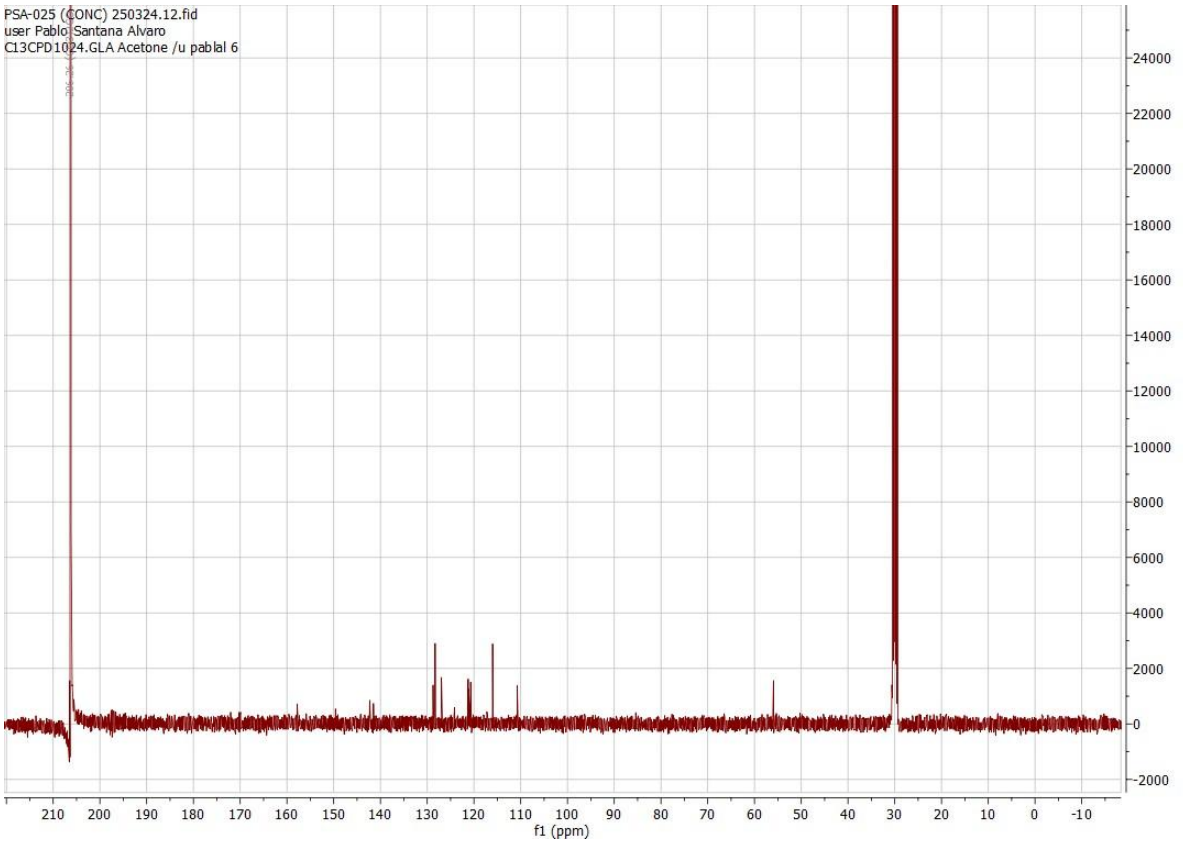

Figure 82: ^{13}C NMR (d6-acetone) of **PSA-018/025**

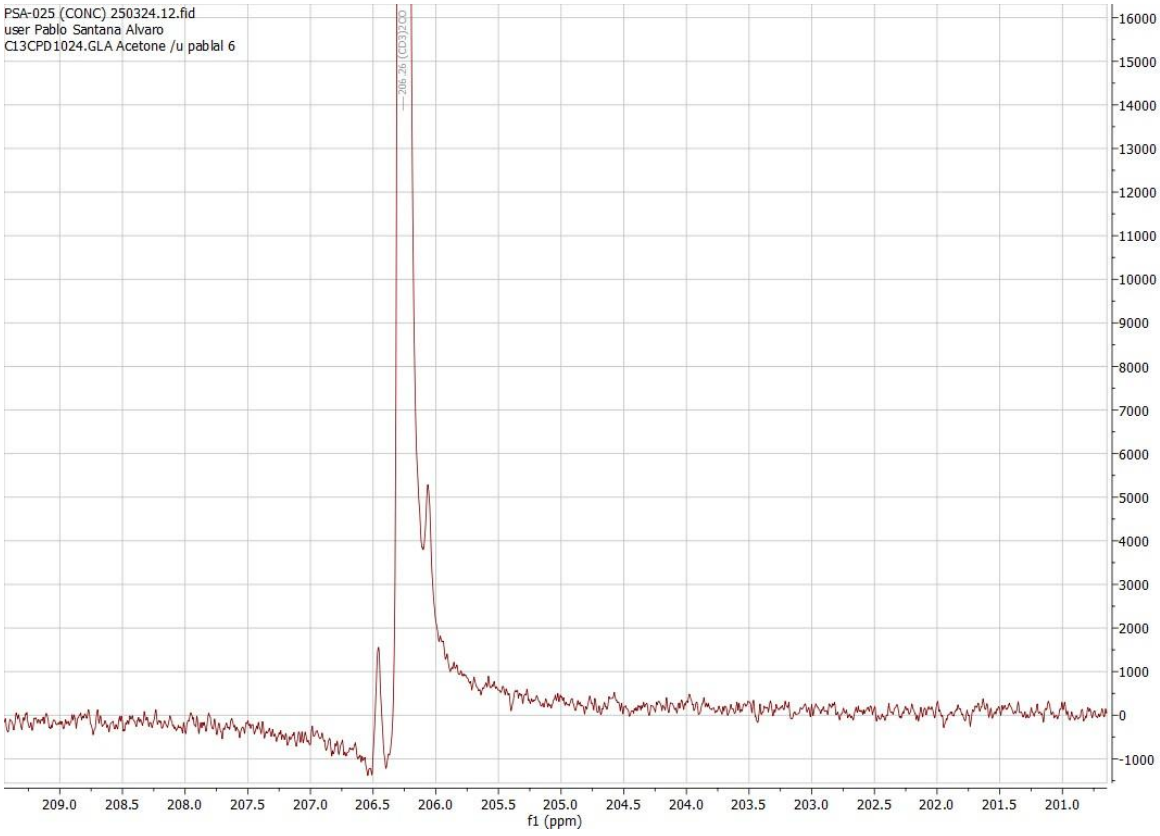

Figure 83: Partial ^{13}C NMR (d6-acetone) of **PSA-018/PSA-025**

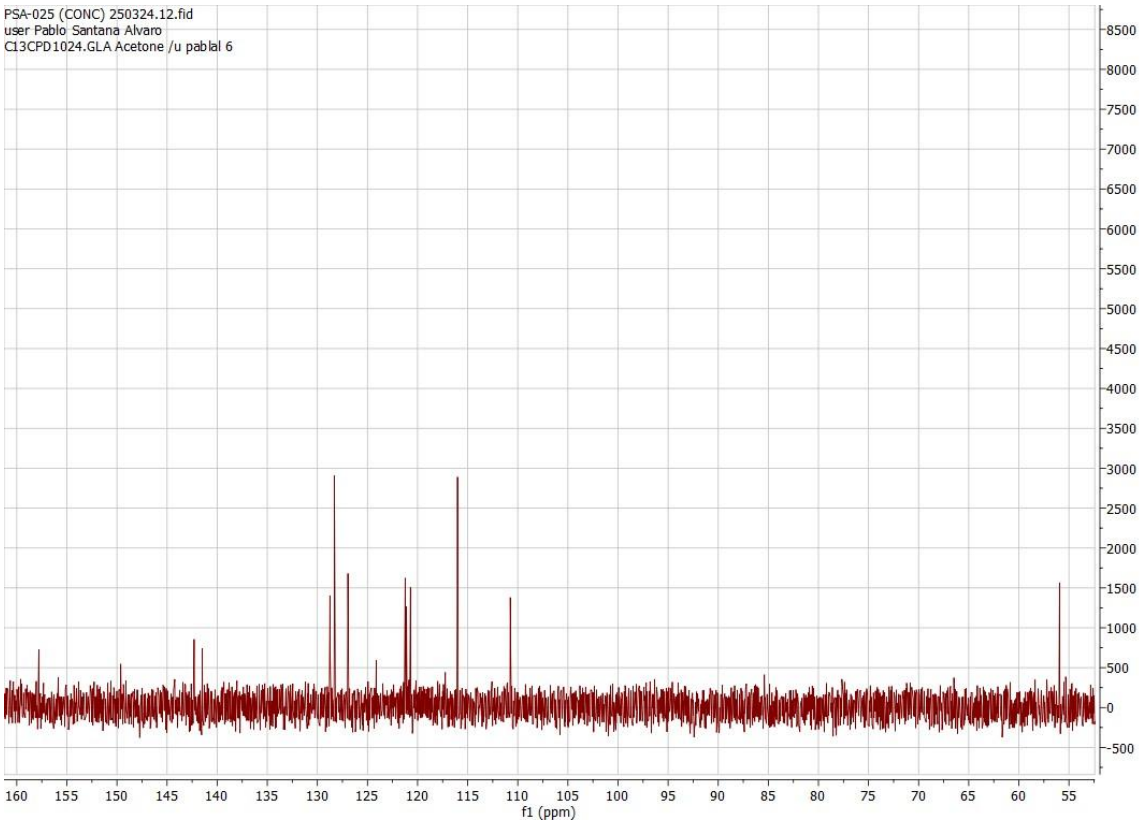

Figure 84: Partial ^{13}C NMR (d6-acetone) of **PSA-018**/**PSA-025**

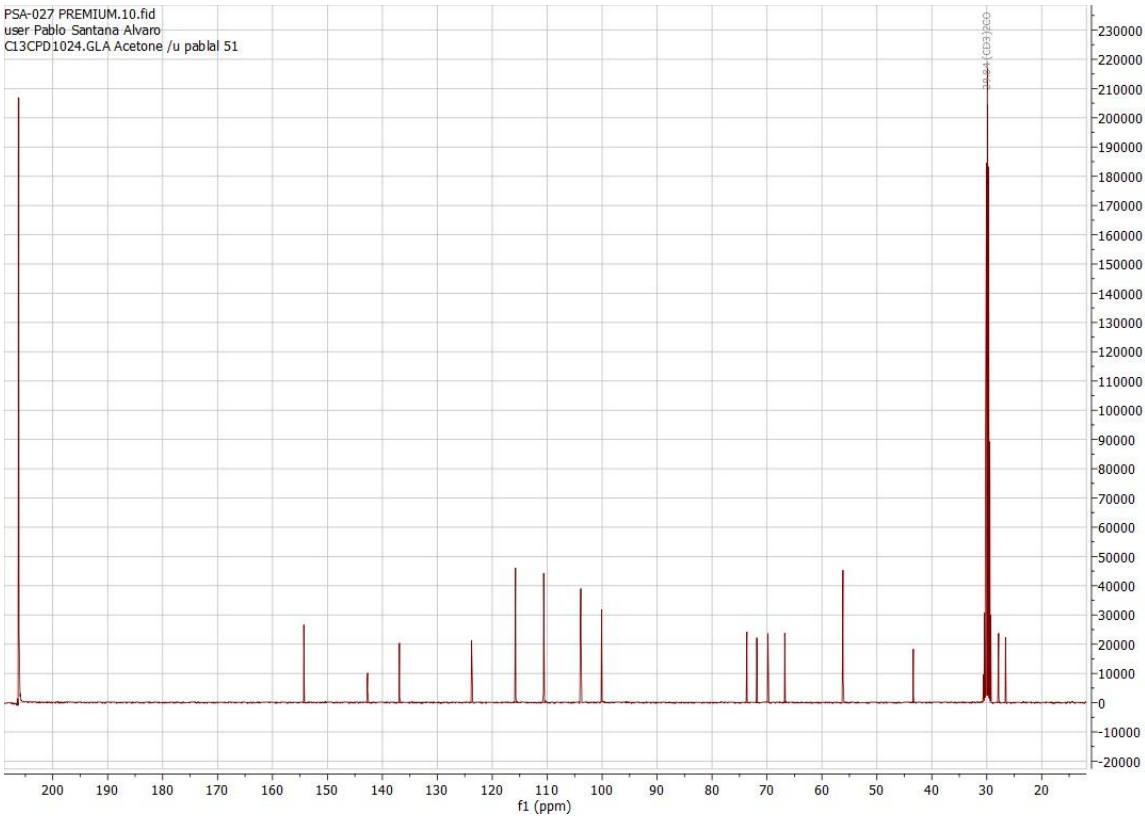

Figure 85: ^{13}C NMR (d6-acetone) of **PSA-027**

Bibliography:

1. Abd Mutalib, M., Aziz, F., Ismail, A.F., Wan Salleh, W.N., Yusof, N., Jaafar, J., Soga, T., Sahdan, M.Z. and Ahmad Ludin, N. *Towards high performance perovskite solar cells: A review of morphological control and HTM development*. *Applied Materials Today*, (2018), **13**, 69–82.
2. Abe, S., Bernede, J., Delvalle, M., Tregouet, Y., Ragot, F., Diaz, F. and Lefrant, S. *Electroluminescent polycarbazole thin films obtained by electrochemical polymerization*. *Synthetic Metals*, (2002), **126**, 1-6.
3. Ahn, N. and Choi, M. *Towards Long-Term Stable Perovskite Solar Cells: Degradation Mechanisms and Stabilization Techniques*. *Advanced science*, (2024), **11**, 1 -18.
4. Amin, S. Panchal, H. *A Review on Thermal Spray Coating Processes*. *International Journal of Current Trends in Engineering & Research*, (2016), **2**, 556–563.
5. Appel, A.M. and Helm, M.L. *Determining the Overpotential for a Molecular Electrocatalyst*. *ACS Catalysis*, (2013), **4**, 630–633.
6. Aziz, F. and Ismail, A.F. *Spray coating methods for polymer solar cells fabrication: A review*. *Materials Science in Semiconductor Processing*, (2015), **39**, 416–425.
7. Bhattacharjee, I., Acharya, N., Bhatia, H. and Ray, D. *Dual Emission through Thermally Activated Delayed Fluorescence and Room-Temperature Phosphorescence, and Their Thermal Enhancement via Solid-State Structural Change in a Carbazole-Quinoline Conjugate*. *Journal of Physical Chemistry Letters*, (2018), **9**, 2733–2738.
8. Bond, A.M. *Electrochemistry: General Introduction*. *Comprehensive Coordination Chemistry 2*, (2003), **2**, 197–222.
9. Capasso, A., Salamandra, L., Giuliana Faggio, Theodoros Dikonimos, Buonocore, F., Morandi, V., Ortolani, L. and Lisi, N. *Chemical Vapor Deposited Graphene-Based Derivative As High-Performance Hole Transport Material for Organic Photovoltaics*. *ACS Applied Materials & Interfaces*, (2016), **8**, 23844–23853.
10. Cariello, M., Pant, N., Harkiss, A.H., Tracey, F.M., Cameron, J., Skabara, P.J., Holliman, P.J., Docampo, P. and Cooke, G. *Synthesis of SOT-OH and its application as a building block for the synthesis of new dimeric and trimeric Spiro-OMeTAD materials*. *Molecular Systems Design & Engineering*, (2022), **7**, 899–905.
11. Chen, C., Ran, C., Yao, Q.-Z., Wang, J., Guo, C., Gu, L., Han, H., Wang, X., Chao, L., Xia, Y. and Chen, Y. *Screen-Printing Technology for Scale Manufacturing of Perovskite Solar Cells*. *Advanced Science*, (2023), **10**, 1–31.
12. Chen, H., Wang, J., Shan, D., Chen, J., Zhang, S. and Lu, X. *Dual-Emitting Fluorescent Metal–Organic Framework Nanocomposites as a Broad-Range pH Sensor for Fluorescence Imaging*. *Analytical Chemistry*, (2018), **90**, 7056–7063.
13. Cho, Y.J., Jeong, M.J., Park, J.H., Hu, W., Lim, J. and Chang, H.S. *Charge Transporting Materials Grown by Atomic Layer Deposition in Perovskite Solar Cells*. *Energies*, (2021), **14**, 1–11.
14. Conte, S., Rodríguez-Calero, G.G., Burkhardt, S.E., Lowe, M.A. and Abruña, H.D. *Designing conducting polymer films for electrochemical energy storage technologies*. *RSC Adv.*, (2013), **3**, 1957–1964.
15. Coyle, D. *Knife and Roll Coating*. *Liquid Film Coating*, ed. S. F. Kistler and P. M. Schweizer, *Chapman and Hall*, *London*, (1997), 539–540.
16. Dame, N. (2024). University of Notre Dame.
17. Ding, X., Liu, J. and Harris, T.A.L. *A review of the operating limits in slot die coating processes*. *AIChE Journal*, (2016), **62**, 2508–2524.
18. Downard, A.J. and Pletcher, D. (1986). *The influence of water on the electrodeposition of polypyrrole in acetonitrile*. *Journal of Electroanalytical Chemistry and Interfacial Electrochemistry*, (1986), **206**, 139–145.

19. Elgrishi, N., Rountree, K.J., McCarthy, B.D., Rountree, E.S., Eisenhart, T.T. and Dempsey, J.L. *A Practical Beginner's Guide to Cyclic Voltammetry*. *Journal of Chemical Education*, (2017), **95**, 197–206.
20. Erazo, E.A., Ortiz, P. and Cortés, M.T. *Tailoring the PEDOT: PSS hole transport layer by electrodeposition method to improve perovskite solar cells*. *Electrochimica Acta*, (2023), **439**, 141573.
21. Esakkimuthu Shanmugasundaram, Chandramohan Govindasamy, Muhammad Ibrar Khan, Ganesan, V., Narayanan, V., Kannan Vellaisamy, Rajaram Rajamohan and Stalin Thambusamy. *Electrospun and electropolymerized carbon nanofiber–polyaniline–Cu material as a hole transport material for organic solar cells*. *Carbon letters*, (2023), **33**, 2223–2235.
22. Ezekoye, B., Offor, P., Ezekoye, V. and Ezema, F. *Chemical Bath Deposition Technique of Thin Films: A Review*. *International Journal of Scientific Research*, (2013), **2**, 452–456.
23. Feiner, A.-S. and McEvoy, A.J. *The Nernst Equation*. *Journal of Chemical Education*, (1994), **71**, 493–494.
24. Feng, J., Jiao, Y., Wang, H., Zhu, X., Sun, Y., Du, M., Cao, Y., Yang, D. and Shengzhong Frank Liu. *High-throughput large-area vacuum deposition for high-performance formamidine-based perovskite solar cells*. *Energy & environmental science (Print)*, (2021), **14**, 3035–3043.
25. Fluorescence Excitation and Emission Fundamentals. (n.d.). University of California: Manuals.
26. Groenendaal, L., Jonas, F., Freitag, D., Pielartzik, H. and Reynolds, J.R. *Poly(3,4-ethylenedioxythiophene) and Its Derivatives: Past, Present, and Future*. *Advanced Materials*, (2000), **12**, 481–494.
27. Groenendaal, L., Zotti, G. and Jonas, F. *Optical, conductive and magnetic properties of electrochemically prepared alkylated poly(3,4-ethylenedioxythiophene)s*. *Synthetic Metals*, (2001), **118**, 105–109.
28. Grysiński, T. and Moroń, Z. *Experimental investigations of Van der Pauw method applied for measuring electrical conductivity of liquids*. *Fundamental and Applied Metrology*, (2009), **3**, 1639–1644.
29. Hassan Elamin Elkhidr, Zeliha Ertekin, Yasemin Arslan Udum and Kadir Pekmez. *Electrosynthesis and characterizations of electrochromic and soluble polymer films based on N- substituted carbazole derivates*. *Synthetic Metals*, (2020), **260**, 116253–116253.
30. Heinze, J. *Electrochemistry of Conducting Polymers*. *Synthetic Metals*, (1991), **41**, 2805–2823.
31. Heinze, J., Rasche, A., Pagels, M. and Geschke, B. *On the Origin of the So-Called Nucleation Loop during Electropolymerization of Conducting Polymers*. *The Journal of Physical Chemistry B*, (2007), **111**, 989–997.
32. Hsiao, S.-H. and Wang, H.-M. *Electrochemically fabricated electrochromic films from 4-(N-carbazolyl)triphenylamine and its dimethoxy derivative*. *RSC Advances*, (2016), **6**, 43470–43479.
33. Huckaba, A.J., Lee, Y., Xia, R., Paek, S., Bassetto, V.C., Oveisi, E., Lesch, A., Kinge, S., Dyson, P.J., Girault, H. and Nazeeruddin, M.K. *Inkjet-Printed Mesoporous TiO_2 and Perovskite Layers for High Efficiency Perovskite Solar Cells*. *Energy Technology*, (2018), **7**, 317–324.
34. Jia, X., Yu, H., Chen, J., Gao, W., Fang, J., Qin, Y., Hu, X. and Shao, G. *Stimuli-Responsive Properties of Aggregation-Induced-Emission Compounds Containing a 9,10-Distyrylanthracene Moiety*. *Chemistry – A European Journal*, (2018), **24**, 19053–19059.

35. Jones, B.J., Korzeniewski, C., Franco, J.H., Minteer, S.D. and Fritsch, I. *Spatially Directed Functionalization by Co-electropolymerization of Two 3,4-ethylenedioxythiophene Derivatives on Microelectrodes within an Array*. *Journal of The Electrochemical Society*, (2020), **167**, 166511–166511.
36. Jung, S.-H., Kim, J.-J. and Kim, H.-J. *High performance inkjet printed phosphorescent organic light emitting diodes based on small molecules commonly used in vacuum processes*. *Thin Solid Films*, (2012), **520**, 6954–6958.
37. Karunakaran, S.K., Arumugam, G.M., Yang, W., Ge, S., Khan, S.N., Lin, X. and Yang, G. *Recent progress in inkjet-printed solar cells*. *Journal of Materials Chemistry A*, (2019), **7**, 13873–13902.
38. Keruckiene, R., Volyniuk, D., Leitonas, K. and Grazulevicius, J.V. *Dual emission fluorescence/room-temperature phosphorescence of phenothiazine and benzotrifluoride derivatives and its application for optical sensing of oxygen*. *Sensors and Actuators B: Chemical*, (2020), **321**, 1–10.
39. Keyvan Rad, J., Mahdavian, A.R., Khoei,S. and Janati Esfahani, A. *FRET-based acrylic nanoparticles with dual-color photoswitchable properties in DU145 human prostate cancer cell line labeling*. *Polymer*, (2016), **98**, 263–269.
40. Kissinger, P.T. and Heineman, W.R. *Cyclic Voltammetry*. *Journal of Chemical Education*, (1983), **60**, 702–706.
41. Lan, Y., Wang, Y.-D., Lan, Z.-R., Wang, Y., Cui, B.-B., Shao, J.-Y. and Zhong, Y.-W. *Thermally stable inverted perovskite solar cells using an electropolymerized Zn-porphyrin film as a dopant-free hole-transporting layer*. *Journal of Materials Chemistry A*, (2023), **11**, 7085–7093.
42. Li, S., Wang, X., Li, H., Fang, J., Wang, D., Xie, G., Lin, D., He, S. and Qiu, L. *Low-Temperature Chemical Bath Deposition of Conformal and Compact NiO_X for Scalable and Efficient Perovskite Solar Modules*. *Small*, (2023), **19**, 1–9.
43. Liou, G.-S., Hsiao, S.-H. and Chen, H.-W. *Novel high-T_g poly(amine-imide)s bearing pendent N-phenylcarbazole units: synthesis and photophysical, electrochemical and electrochromic properties*. *Journal of Materials Chemistry*, (2006), **16**, 1831.
44. Liu Mingxuan, Zhou, B., Zhou, L., Xie, Z., Li, S. and Chen, L. *Nitroxyl radical based conjugated microporous polymers as heterogeneous catalysts for selective aerobic alcohol oxidation*. *J. Mater. Chem. A*, (2018), **6**, 9860–9865.
45. Liu, Y., Liu, T., Pang, L., Guo, J., Wang, J., Qi, D., Li, W. and Shen, K. *Novel triphenylamine polyamides bearing carbazole and aniline substituents for multi-colored electrochromic applications*. *Dyes and Pigments*, (2020), **173**, 1–13.
46. Mangione, M.I., Spanevello, R.A. and Anzardi, M.B. *Efficient and straightforward click synthesis of structurally related dendritic triazoles*. *RSC Adv.*, (2017), **7**, 47681–47688.
47. Marques, A.S., Szostak, R., Marchezi, P.E. and Nogueira, A.F. *Perovskite solar cells based on polyaniline derivatives as hole transport materials*. *J. Phys energy*, (2018), **1**, 1–10.
48. Matsumura, T. and Sato, Y. *A Theoretical Study on Van Der Pauw Measurement Values of Inhomogeneous Compound Semiconductor Thin Films*. *Journal of Modern Physics*, (2010), **1**, 340–347.
49. Mengesha, E.T., Demissie, T.B., Mesfin Redi-Abshiro and Mohammed, A.M. *Dual fluorescence of (E)-N-(4-(dimethylamino) benzylidene)-2H-1,2,4-triazol-3-amine (DMABA-Amtr): A ground state perspective*. *Spectrochimica Acta Part A Molecular and Biomolecular Spectroscopy*, (2018), **189**, 601–607.
50. Moran, P.J. and Gileadi, E. Alleviating the common confusion caused by polarity in electrochemistry. *Journal of Chemical Education*, (1989), **66**, 912.

51. Nadege, A., George Omololu Odunmbaku, Ouyang, Y., Xiong, X., Guo, B., Chen, S., Lu, S. and Sun, K. *Eco-friendly processing of perovskite solar cells in ambient air*. *Renewable and Sustainable Energy Reviews*, (2024), **192**, 119–145.
52. Norrman, K., Ghanbari-Siahkali, A. and Larsen, N.B. *6 Studies of spin-coated polymer films*. *Annual Reports Section 'C' (Physical Chemistry)*, (2005), **101**, 174–201.
53. Nørskov, J.K., Rossmeisl, J., Logadottir, A., Lindqvist, L., Kitchin, J.R., Bligaard, T. and Jónsson, H. *Origin of the Overpotential for Oxygen Reduction at a Fuel-Cell Cathode*. *The Journal of Physical Chemistry B*, (2004), **108**, 17886–17892.
54. Nutting, J.E., Gerken, J.B., Stamoulis, A.G., Bruns, D.L. and Stahl, S.S. *'How Should I Think about Voltage? What Is Overpotential?': Establishing an Organic Chemistry Intuition for Electrochemistry*. *The Journal of Organic Chemistry*, (2021), **86**, 15875–15885.
55. Oliveira, F.S., Cipriano, R.B., da Silva, F.T., Romão, E.C. and dos Santos, C. a. M. *Simple analytical method for determining electrical resistivity and sheet resistance using the van der Pauw procedure*. *Scientific Reports*, (2020), **10**, 1–8.
56. Oviroh, P.O., Akbarzadeh, R., Pan, D., Coetzee, R.A.M. and Jen, T.-C. *New development of atomic layer deposition: processes, methods and applications*. *Science and Technology of Advanced Materials*, (2019), **20**, 465–496.
57. Palma-Cando, A., Woitassek, D., Brunklaus, G. and Scherf, U. *Luminescent tetraphenylethene-cored, carbazole- and thiophene-based microporous polymer films for the chemosensing of nitroaromatic analytes*. *Materials Chemistry Frontiers*, (2017), **1**, 1118–1124.
58. Park, S., Jeong, S., Kang, C. and Hong, S. *Synthesis of Conjugated Copolymer Containing Spirobifluorene Skeleton by Acyclic Diene Metathesis Polymerization for Polymer Light-Emitting Diode Applications*. *Bulletin of the Korean Chemical Society*, (2021), **42**, 929–933.
59. Patidar, R., Burkitt, D., Hooper, K., Richards, D. and Watson, T. *Slot-die coating of perovskite solar cells: An overview*. *Materials Today Communications*, (2020), **22**, 1–13.
60. Patschinski, P., Zhang, C. and Zipse, H. *The Lewis Base-Catalyzed Silylation of Alcohols—A Mechanistic Analysis*. *The Journal of Organic Chemistry*, (2014), **79**, 8348–8357.
61. Peng, X., Yuan, J., Shen, S., Gao, M., Chesman, A.S.R., Yin, H., Cheng, J., Zhang, Q. and Angmo, D. *Perovskite and Organic Solar Cells Fabricated by Inkjet Printing: Progress and Prospects*. *Advanced Functional Materials*, (2017), **27**, 1–27.
62. Poverenov, E., Li, M., Bitler, A. and Bendikov, M. *Major Effect of Electropolymerization Solvent on Morphology and Electrochromic Properties of PEDOT Films*. *Chemistry of Materials*, (2010), **22**, 4019–4025.
63. Rana, Md.S., Rahman, M.A. and Alam, A.M.S. *A CV Study of Copper Complexation with Guanine Using Glassy Carbon Electrode in Aqueous Medium*. *ISRN Electrochemistry*, (2014), **2014**, 1–7.
64. Reger, D., Haines, P., Amsharov, K.Y., Schmidt, J.A., Ullrich, T., Bönisch, S., Hampel, F., Görling, A., Nelson, J., Jelfs, K.E., Guldi, D.M. and Jux, N. *A Family of Superhelicenes: Easily Tunable, Chiral Nanographenes by Merging Helicity with Planar π Systems*. *Angewandte Chemie International Edition*, (2021), **60**, 18073–18081.
65. Romero, M., M.A. del Valle, R. del Río, F.R. Díaz and Armijo, F. *Polymers Nucleation and Growth Mechanism: Solubility, a Determining Factor*. *International Journal of Electrochemical Science*, (2012), **7**, 10132–10141.
66. Schiavon, G., Sitran, S. and Zotti, G. *A simple two-band electrode for in situ conductivity measurements of polyconjugated conducting polymers*. *Synthetic Metals*, (1989), **32**, 209–217.

67. Schmidt-Hansberg, B., Michael, Peters, K., Buss, F., Pfeifer, J., Walheim, S., Colsmann, A., Lemmer, U., Scharfer, P. and Schabel, W. *In situ monitoring the drying kinetics of knife coated polymer-fullerene films for organic solar cells*. *Journal of Applied Physics*, (2009), **106**, 1–8.
68. Seki, Y., Takahashi, M. and Takashiri, M. *Effects of different electrolytes and film thicknesses on structural and thermoelectric properties of electropolymerized poly(3,4-ethylenedioxythiophene) films*. *RSC Advances*, (2019), **9**, 15957–15965.
69. Seong Ryul Pae, Byun, S., Kim, J., Kim, M.-K., Issam Gereige and Shin, B. *Improving Uniformity and Reproducibility of Hybrid Perovskite Solar Cells via a Low-Temperature Vacuum Deposition Process for NiO_x Hole Transport Layers*. *ACS Applied Materials & Interfaces*, (2018), **10**, 534–540.
70. Shao, J.-Y., Yu, B., Wang, Y.-D., Lan, Z.-R., Li, D., Meng, Q. and Zhong, Y.-W. *In-Situ Electropolymerized Polyamines as Dopant-Free Hole-Transporting Materials for Efficient and Stable Inverted Perovskite Solar Cells*. *ACS Applied Energy Materials*, (2020), **3**, 5058–5066.
71. Shao, J.-Y. and Zhong, Y.-W. *Pyrene-Cored Hole-Transporting Materials for Efficient and Stable Perovskite Solar Cells*. *Bulletin of the Chemical Society of Japan*, (2021), **94**, 632–640.
72. Shao, J.-Y. and Zhong, Y.-W. *Toward Stable and Efficient Solar Cells with Electropolymerized Films*. *ACS Sustainable Chemistry & Engineering*, (2022), **10**, 13555–13567.
73. Swartwout, R., Hoerantner, M.T. and Bulović, V. *Scalable Deposition Methods for Large-area Production of Perovskite Thin Films*. *Energy & Environmental Materials*, (2019), **2**, 119–145.
74. Tan, S.Y., Chia, V.Y.Y., Hölttä-Otto, K. and Anariba, F. *Teaching the Nernst Equation and Faradaic Current through the Use of a Designette: An Opportunity to Strengthen Key Electrochemical Concepts and Clarify Misconceptions*. *Journal of Chemical Education*, (2020), **97**, 2238–2243.
75. Trippé, G., Le Derf, F., Lyskawa, J., Mazari, M., Roncali, J., Gorgues, A., Levillain, E. and Sallé, M. *Crown-Tetrathiafulvalenes Attached to a Pyrrole or an EDOT Unit: Synthesis, Electropolymerization and Recognition Properties*. *Chemistry – A European Journal*, (2004), **10**, 6497–6509.
76. Tyona, M.D. *A theoretical study on spin coating technique*. *Advances in materials Research*, (2013), **2**, 195–208.
77. Usluer, O., Demic, S., Egbe, D., Birckner, E., Tozlu, C., Pivrikas, A., Ramil, A. and Sariciftci, N. *Fluorene-Carbazole Dendrimers: Synthesis, Thermal, Photophysical and Electroluminescent Device Properties*. *Adv. Funct. Mater*, (2010), **20**, 4152–4161.
78. Van der Pauw, L.J. *A Method of Measuring the Resistivity and Hall Coefficient on Lamellae of Arbitrary Shape*. *Philips Technical Review*, (1958), **20**, 220 - 224.
79. Vidal-Iglesias, F.J., Solla-Gullón, J., Rodes, A., Herrero, E. and Aldaz, A. *Understanding the Nernst Equation and Other Electrochemical Concepts: An Easy Experimental Approach for Students*. *Journal of Chemical Education*, (2012), **89**, 936–939.
80. Wadley, H.N.G., Zhou, X., Johnson, R.A. and Neurock, M. *Mechanisms, models and methods of vapor deposition*. *Progress in Materials Science*, (2001), **46**, 329–377.
81. Wang, H., Thiele, A.M. and Pilon, L. *Simulations of Cyclic Voltammetry for Electric Double Layers in Asymmetric Electrolytes: A Generalized Modified Poisson–Nernst–Planck Model*. *Journal of Physical Chemistry C*, (2013), **117**, 18286–18297.
82. Wang, Y., Zhang, S., Wu, J., Liu, K., Li, D., Meng, Q. and Zhu, G. *Electropolymerization Porous Aromatic Framework Film As a Hole-Transport Layer*

for Inverted Perovskite Solar Cells with Superior Stability. *ACS Applied Materials & Interfaces*, (2017), **9**, 43688–43695.
83. Yang, J., Li, Z. and Jia, Q. *Design of dual-emission fluorescence sensor based on Cu nanoclusters with solvent-dependent effects: Visual detection of water via a smartphone*. *Sensors and Actuators B-chemical*, (2019), **297**, 1–8.
84. Yi, Z., Li, X., Xiong, Y., Shen, G., Zhang, W., Huang, Y., Jiang, Q., Xin Ren Ng, Luo, Y., Zheng, J., Wei Lin Leong, Fu, F., Bu, T. and Yang, J. *Self-assembled monolayers (SAMs) in inverted perovskite solar cells and their tandem photovoltaics application*. *Interdisciplinary materials*, (2024), **3**, 203–244.
85. Zhou, M. and Heinze, J. *Electropolymerization of Pyrrole and Electrochemical Study of Polypyrrole. 2. Influence of Acidity on the Formation of Polypyrrole and the Multipathway Mechanism*. *The Journal of Physical Chemistry B*, (1999), **103**, 8443–8450.
86. Zhu, Y., Zhang, J., Chen, Z., Zhang, A. and Ma, C. *Synthesis of nitrocarbazole compounds and their electrocatalytic oxidation of alcohol*. *Chinese Journal of Catalysis*, (2016), **37**, 533–538.
87. Bard, A.J. and Faulkner, L.R. *Electrochemical Methods: Fundamentals and Applications*. *John Wiley and Sons*, *United Kingdom*, (2001), 32.
88. Chou, L.-H., Julian and Liu, C.-L. *Progress in Spray Coated Perovskite Films for Solar Cell Applications*. *Solar RRL*, (2022), **6**, 1–13.
89. Heravi, M.M., Kheilkordi, Z., Zadsirjan, V., Heydari, M. and Malmir, M. *Buchwald-Hartwig reaction: An overview*. *Journal of Organometallic Chemistry*, (2018), **861**, 17–104.
90. Jason, J., Muhamad Afiq Akbar, Mohd, Y., Pike, A., Choo Ta Goh, Mustapha, S. and Ling Ling Tan (2024). *Enhancing early warning: A DNA biosensor with polyaniline/graphene nanocomposite for label-free voltammetric detection of saxitoxin-producing harmful algae*. *Chemosphere*, (2024), **364**, 1–12.
91. Jiang, W., Wang, D., Shang, W., Li, Y., Zeng, J., Zhu, P., Zhang, B., Mei, L., Chen, X.-K., Xu, Z.-X., Lin, F.R., Xu, B. and Jen, A.K.-Y. *Spin-coated and vacuum-processed hole-extracting self-assembled multilayers with H-aggregation for high-performance inverted perovskite solar cells*. *Angewandte Chemie International Edition*, (2024), **2024**, 1–20.
92. Zhang, H., Darabi, K., Nia, N.Y., Krishna, A., Ahlawat, P., Guo, B., Almalki, M.H.S., Su, T.-S., Ren, D., Bolnykh, V., Castriotta, L.A., Zendehdel, M., Pan, L., Alonso, S.S., Li, R., Zakeeruddin, S.M., Hagfeldt, A., Rothlisberger, U., Di Carlo, A. and Amassian, A. *A universal co-solvent dilution strategy enables facile and cost-effective fabrication of perovskite photovoltaics*. *Nature Communications*, (2022), **13**, 1–12.
93. Mothika, V.S., Räupke, A., Brinkmann, K.O., Riedl, T., Brunklaus, G. and Scherf, U. *Nanometer-Thick Conjugated Microporous Polymer Films for Selective and Sensitive Vapor-Phase TNT Detection*. *ACS Applied Nano Materials*, (2018), **1**, 6483–6492.

94. Yang, S., Yang, C., Zhang, X., Zheng, Z., Bi, S., Zhang, Y. and Zhou, H. *A conjugated microporous polymer film fabricated by in situ electro-chemical deposition as a hole transporting layer in organic photovoltaics*. *Journal of Materials Chemistry C*, (2018), **6**, 9044–9048.
95. Lee, J.-S.M. and Cooper, A.I. *Advances in Conjugated Microporous Polymers*. *Chemical Reviews*, (2020), **120**, 2171–2214.
96. Guo, R., Zhang, X., Zheng, X., Li, L., Li, M., Zhao, Y., Zhang, S., Luo, L., You, S., Li, W., Gong, Z., Huang, R., Cui, Y., Rong, Y., Zeng, H. and Li, X. *Tailoring Multifunctional Self-Assembled Hole Transporting Molecules for Highly Efficient and Stable Inverted Perovskite Solar Cells*. *Advanced Functional Materials*, (2023), **33**, 1-9.
97. Ece Aktas, Phung, N., Köbler, H., González, D.A., Méndez, M., Ivona Kafedjiska, Silver-Hamill Turren-Cruz, Wenisch, R., Lauermann, I., Abate, A. and Palomares, E. *Understanding the perovskite/self-assembled selective contact interface for ultra-stable and highly efficient p–i–n perovskite solar cells*. *Energy and Environmental Science*, (2021), **14**, 3976–3985.
98. Cassella, E.J., Spooner, E.L.K., Thornber, T., O'Kane, M.E., Catley, T.E., Bishop, J.E., Smith, J.A., Game, O.S. and Lidzey, D.G. *Gas-Assisted Spray Coating of Perovskite Solar Cells Incorporating Sprayed Self-Assembled Monolayers*. *Advanced Science*, (2022), **9**, 1–10.
99. Santana Alvaro, P. *The synthesis and characterization of a new hole transporting material*, BSci (Hons) thesis, University of Glasgow, Glasgow, (2023).
100. P. Boix, K. Nonomura, N. Mathews and S. G. Mhaisalkar. *Current progress and future perspectives for organic/inorganic perovskite solar cells*. *Materials Today*, (2014), **17**, 16–23.
101. A. Kojima, K. Teshima, Y. Shirai and T. Miyasaka. *Organometal Halide Perovskites as Visible-Light Sensitizers for Photovoltaic Cells*. *Journal of the American Chemical Society*, (2009), **131**, 6050–6051.
102. Palz, W. *Power for the World: The Emergence of Electricity from the Sun*, Jenny Stanford Publishing, New York, (2010).
103. T. Liu, K. Chen, Q. Hu, Zhao, L., Luo, D., Wu, J., Zhang, Y., Zhang, W., Liu, F., P. Russel, T., R. Zhu and Q. Gong. *Charge-Carrier Balance for Highly Efficient Inverted Planar Heterojunction Perovskite Solar Cells*. *Advanced Energy Materials*, (2016), **28**, 10718–10724.
104. W. Yan, Y. Li, Y. Liu, S. Ye, Z. Liu, S. Wang, Z. Bian and C. Huang. *Room-temperature and Solution-processed Copper Iodide as the Hole Transport Layer for Inverted Planar Perovskite Solar Cells*. *Nano Energy*, (2015), **16**, 428–437.
105. F. Hou, Z. Su, F. Jin, X. Yan, L. Wang, H. Zhao, J. Zhu, B. Chu and W. Li. *Efficient and Stable Planar Heterojunction Perovskite Solar Cells with an MoO_3/PEDOT:PSS Hole Transporting Layer*. *Nanoscale*, (2015), **7**, 9427–9432.

106. C. Liu, H. Luo, G. Shi, L. Nian, Z. Chi and Y. Ma, *Electrochemical route to fabricate porous organic polymers film and its application for polymer solar cells*. *Dyes and Pigments*, (2017), **142**, 132–138.

107. S. P. Ponnappa, J. Macleod, M. Umer, N. Soda, A. S. Pannu, M. J. A. Shiddiky, G. A. Ayoko, A. P. O'Mullane and P. Sonar. *Electropolymerized Porous Polymer Films on Flexible Indium Tin Oxide Using Trifunctional Furan Substituted Benzene Conjugated Monomer for Biosensing*. *ACS Applied Polymer Materials*, (2020), **2**, 351–359.

108. Zhou, Z., Li, X., Guo, D., B. Shinde, D., Lu, D., Chen, L., Liu, X., Cao, L., M. Aboalsaud, A., Hu Y. and Lai, Z. *Electropolymerization of robust conjugated microporous polymer membranes for rapid solvent transport and narrow molecular sieving*. *Nat Commun*., (2020), **11**, 1–9

109. H. Ma, Y. Chen, X. Li and B. Li, *Advanced Applications and Challenges of Electropolymerized Conjugated Microporous Polymer Films*. *Advanced Functional Materials*, (2021), **31**, 1–19.

110. N. Jangid, N. Pal, S. Chauhan and K. Meghwal. *Conducting polymers and their applications*. *Research Journal of Pharmaceutical, Biological and Chemical Sciences,* (2014), **5**, 383–412.

111. J.-X. Jiang, F. Su, H. Niu, C. D. Wood, N. L. Campbell, Y. Z. Khimyak and A. I. Cooper. *Conjugated Microporous Poly(phenylene butadiynylene)s*. *Chem. Commun.*, (2008), Issue 4, 486–488.

112. Troisi, A. *Charge transport in high mobility molecular semiconductors: classical models and new theories*. *Chemical Society Reviews*, (2011), **40**, 2347–2358.

113. Hua, Y., Liu, P., Li, Y., Sun, L. and Kloo, L. *Composite Hole-Transport Materials Based on a Metal-Organic Copper Complex and Spiro-OMeTAD for Efficient Perovskite Solar Cells. Solar RRL*, (2018), **2**, 1–7.